2007

Defect detection using eddy-currents and Hall effect sensor arrays

Raza Ali
Iowa State University

Defect detection using eddy-currents and Hall effect sensor arrays

by

Raza Ali

A thesis submitted to the graduate faculty

in partial fulfillment of the requirements for the degree of

MASTER OF SCIENCE

Major: Electrical Engineering

Program of Study Committee:
John Bowler, Major Professor
David Hsu
Nicola Bowler

Iowa State University

Ames, Iowa

2007

TABLE OF CONTENTS

LIST OF TABLES iv

LIST OF FIGURES v

INTRODUCTION 1

CHAPTER 1. Benchmark Problems in Eddy-Current Nondestructive Evaluation 3

1.1 Introduction 3

1.1.1 Experimental Configuration 3

1.1.2 Coil Construction 4

1.1.3 Test Specimen 5

1.1.4 Overview of the measurement technique 6

1.1.5 Correction for Nonideal Coil Behavior 7

1.1.6 Correction Procedure 8

1.1.7 Determination of Effective Coil Parameters 10

1.1.8 Results 11

1.1.9 Significance of cable separation 11

1.1.10 Benchmark Experiment showing Edge Effects 12

1.1.11 Conclusion 16

CHAPTER 2. Hall Effect Sensors for Eddy Current Probe Arrays 32

2.1 Introduction 32

2.1.1 Our Project 34

2.1.2 Hall Effect Physics 37

2.1.3 Parameters of Hall Effect Sensors that were tested 39
2.1.4 Principle of Modulation 49
2.1.5 Modulation in Hall Effect Sensors 49
2.1.6 Detector circuitry 56
2.1.7 The Hall Array 59
2.1.8 The P-2 Hall Sensor 62
2.1.9 Labview Software 63
2.1.10 Conclusion 63
2.1.11 Acknowledgements 64

APPENDIX . ENHANCED FLAW DETECTION USING AN EDDY CURRENT PROBE WITH A LINEAR ARRAY OF HALL SENSORS [27] . 68

BIBLIOGRAPHY 79

ACKNOWLEDGEMENTS 82

LIST OF TABLES

Table 1.1	Measured Coil Parameters [1]	5
Table 1.2	Measured Plate Parameters	6
Table 1.3	Comparison of Nominal Measured Parameters and Effective Parameters Obtained by Least Squares Fits Using the Theory of Dodd and Deeds	11
Table A.1	Characteristics of the P2 Hall sensors.	72

LIST OF FIGURES

Figure 1.1 Geometry of the benchmark experiment: circular air-cored coil positioned above a flawless Aluminum alloy plate 4

Figure 1.2 Equivalent electrical circuit for an eddy-current probe coil 9

Figure 1.3 Change in coil impedance due to an unflawed region of plate, normalized to the ideal isolated coil reactance X_o. The open circles denote the uncorrected experimental data, the filled circles denote the corrected experimental data and the solid curve represent the theoretical calculations using the effective coil parameters and Dodd and Deeds Theory [2]. The results were obtained using the 0.3 inch cable 13

Figure 1.4 Change in coil impedance due to an unflawed region of plate, normalized to the ideal isolated coil reactance X_o. The open circles denote the uncorrected experimental data, the filled circles denote the corrected experimental data and the solid curve represent the theoretical calculations using the effective coil parameters and Dodd and Deeds Theory [2]. The results were obtained using the 1 inch cable 14

Figure 1.5 Impedance comparison between the 1 inch cable and the 0.3 inch cable. For the comparison, the uncorrected experiment data was used. Red circles for the 1 inch cable and Black circles for 0.3 inch cable 15

Figure 1.6 Change in coil impedance, as the coil moves from free space towards the edge of the plate, normalized to the ideal isolated (free space) coil reactance X_o and at frequency of 1 kHz 17

Figure 1.7 Change in coil impedance, as the coil moves from free space towards the edge of the plate, normalized to the ideal isolated (free space) coil reactance X_o and at frequency of 2.5 kHz 18

Figure 1.8 Change in coil impedance, as the coil moves from free space towards the edge of the plate, normalized to the ideal isolated (free space) coil reactance X_o and at frequency of 6.3 kHz 19

Figure 1.9 Change in coil impedance, as the coil moves from free space towards the edge of the plate, normalized to the ideal isolated (free space) coil reactance X_o and at frequency of 15.9 kHz 20

Figure 1.10 Change in coil impedance, as the coil moves from free space towards the edge of the plate, normalized to the ideal isolated (free space) coil reactance X_o and at frequency of 40 kHz 21

Figure 1.11 Change in coil impedance, as the coil moves over the edge of the plate towards free space, normalized to the ideal isolated (free space) coil reactance X_o and at frequency of 1 kHz 22

Figure 1.12 Change in coil impedance, as the coil moves over the edge of the plate towards free space, normalized to the ideal isolated (free space) coil reactance X_o and at frequency of 2.5 kHz 23

Figure 1.13 Change in coil impedance, as the coil moves over the edge of the plate towards free space, normalized to the ideal isolated (free space) coil reactance X_o and at frequency of 6.3 kHz 24

Figure 1.14 Change in coil impedance, as the coil moves over the edge of the plate towards free space, normalized to the ideal isolated (free space) coil reactance X_o and at frequency of 15.9 kHz 25

Figure 1.15 Change in coil impedance, as the coil moves over the edge of the plate towards free space, normalized to the ideal isolated (free space) coil reactance X_o and at frequency of 40 kHz 26

Figure 1.16 Comparison between the change in impedance when the coil moves from free space towards the edge of the plate (black circles) and the change in impedance when the coil moves from the edge of the plate towards free space (red circles), normalized to the ideal isolated (free space) coil reactance X_o and at frequency of 1 kHz 27

Figure 1.17 Comparison between the change in impedance when the coil moves from free space towards the edge of the plate (black circles) and the change in impedance when the coil moves from the edge of the plate towards free space (red circles), normalized to the ideal isolated (free space) coil reactance X_o and at frequency of 2.5 kHz 28

Figure 1.18 Comparison between the change in impedance when the coil moves from free space towards the edge of the plate (black circles) and the change in impedance when the coil moves from the edge of the plate towards free space (red circles), normalized to the ideal isolated (free space) coil reactance X_o and at frequency of 6.3 kHz 29

Figure 1.19 Comparison between the change in impedance when the coil moves from free space towards the edge of the plate (black circles) and the change in impedance when the coil moves from the edge of the plate towards free space (red circles), normalized to the ideal isolated (free space) coil reactance X_o and at frequency of 15.9 kHz 30

Figure 1.20 Comparison between the change in impedance when the coil moves from free space towards the edge of the plate (black circles) and the change in impedance when the coil moves from the edge of the plate towards free space (red circles), normalized to the ideal isolated (free space) coil reactance X_o and at frequency of 40 kHz 31

Figure 2.1 Final configuration of the Hall array probe 35

Figure 2.2 PCB showing the 32 element Hall array. This side would be resting on the specimen 36

Figure 2.3 The inside surface of the PCB showing the racetrack coil and the contacts for the 32 element Hall array 36
Figure 2.4 Hall Effect Transducer showing critical dimensions and axis 37
Figure 2.5 Schematic diagram of the system used to measure the sensitivity of a Hall device as a function of frequency 41
Figure 2.6 Sensitivity of the P-2 Hall sensor as a function of frequency 42
Figure 2.7 Sensitivity of the P-15 Hall sensor as a function of frequency 43
Figure 2.8 Sensitivity of the HW-105 Hall sensor as a function of frequency 44
Figure 2.9 Sensitivity of the MRC Hall sensor as a function of frequency 44
Figure 2.10 Diagram to give a general idea of the relationship between temperature and sensitivity. For more detail, a Fig based on experimental data and typical results for sensitivity vs temperature; see [16][17] 45
Figure 2.11 Ohmic offsets results from misalignment of the sense contacts and inhomogeneities in the material 46
Figure 2.12 Figure Explaining the concept of modulation 52
Figure 2.13 Block diagram of the circuit layout during the process of modulation . 53
Figure 2.14 Sensitivity without Modulation 54
Figure 2.15 Sensitivity with modulation 54
Figure 2.16 Comparison between the frequency spectrum of an ideal sinusoid and a real world sinusoid 55
Figure 2.17 Process of Modulation in frequency domain 57
Figure 2.18 Block Diagram of the detector circuit 59
Figure 2.19 PCB showing four detector circuits. Each circuit handles one Hall Sensor. There are 32 circuits in total on 8 PCBs 60
Figure 2.20 Schematic of the detector circuit 61
Figure 2.21 Parallel configuration of the Hall sensors 64
Figure 2.22 Series configuration of the Hall sensors 64

Figure 2.23 Actual wafer (die) of Hall sensors containing more than 5000+ Hall sensors 65
Figure 2.24 Zoomed in of the actual wafer showing 16 series (rows labeled 1), 16 parallel (rows labeled 3) and 16 individual (rows labeled 2) Hall sensors 66
Figure 2.25 Coil configurations 67
Figure 2.26 Hall sensors zoomed-in 67

Figure A.1 Epitaxial structure of the Hall effect sensor (P2) 70
Figure A.2 Geometries of the Hall sensor arrays. The dimensions shown in the Fig are a = 400 μm, b = 90 μm, c = 70 μm, d = 80 μm, e = 50 μm, f = 100 μm, W = 70 μm, L = 210 μm. Note that the tracks connecting between sensors are not shown. 70
Figure A.3 Different coils and Hall sensor array arrangements. 71
Figure A.4 Block diagram of the Hall array circuit system. 74
Figure A.5 Block diagram of the detector circuit for one channel. 75
Figure A.6 Experimental results showing the effect of modulation. For the modulated data, the Hall sensor is biased with an AC current at a frequency of 30kHz which acts as the carrier frequency of the amplitude modulated signal. In acquiring data without modulation, the Hall sensor is biased with a DC current. 76

INTRODUCTION

Eddy current testing is an electromagnetic technique and can only be used on conductive materials. Applications include crack and corrosion detection, the sorting of actual components using conductivity variations, conductivity measurements and the measurements of surface layer properties, for example coating thickness. The method is most commonly used in the aerospace industry, but also in the power, automotive, marine and manufacturing industries.

Here is how the technique works. When a coil carrying an AC current is brought near to the surface of a metal specimen, eddy currents are induced into the specimen. The AC current in the coil generates a changing magnetic field, which interacts with the test object and induces eddy currents. These eddy currents set up small magnetic fields of their own that tends to oppose the original magnetic field of the coil. This change in the original magnetic field can be detected through changes of the coil impedance. A probe moved over the surface of a defect free specimen has a constant impedance if its height above the surface is kept constant, but if there are defects present in the material, then the defects will cause the original magnetic field to vary beyond the expected value and that will indicate a presence of a defect in the material through changes of the coil impedance. The variation in the magnetic field causes the impedance of the coil to change and this is how it is measured. Thus, a defect will cause the impedance of the coil to change beyond that is expected of the given material, indicating the defect. This is eddy current testing.

The induced eddy currents in the specimen are distorted by the presence of the flaws or material variations, causing the impedance in the coil to change. This change is measured and displayed in a manner that provides an indication of the type of flaw or material condition. Eddy currents also have the ability to penetrate the surface and detect sub-surface defects that

are ordinarily invisible to the naked eye. The detection of defects can prevent a major failure in a critical component which could lead to a costly repair, or even a loss of life. Nondestructive evaluation is justified because it prevents critical failures of power plants and transport systems and ensures their safe operation.

Eddy current inspection technique is called nondestructive as the test material remains intact during the testing procedure. Eddy current inspection is widely used to detect cracks, corrosion, and other defects in metallic structures. However, while eddy current nondestructive evaluation (NDE) has proved to be a reliable method for defect detection, it is only recently that the potential for eddy current defect sizing has begun to be fully explored. At present, practical crack sizing methods using eddy current NDE have relied on the use of either calibration flaws or estimates of crack depths via measurements of the surface crack length, and have limited applicability.

Recently model based crack sizing techniques have been developed which use inversion techniques. In order to be able to determine crack parameter in this way, it is first necessary to ensure that the models are validate and thus shown to give correct signal predictions. This is usually done by performing carefully controlled benchmark experiments and comparing the results with model predictions. In the first part of this thesis a benchmark experiment is described which uses eddy current technique to detect the change in the impedance of the coil.

In the second part of this thesis, eddy current techniques and Hall effect sensors are used to detect defects in the material.

CHAPTER 1. Benchmark Problems in Eddy-Current Nondestructive Evaluation

1.1 Introduction

Below is a benchmark problem presented for verification of theoretical calculations of the impedance change in a coil due to a layered conducting half space. The benchmark problem is based on careful measurements of the change in coil impedance as a function of frequency for a circular air-cored coil which is scanned over a 2024-T3 Aluminium alloy plate. Deviations from ideal coil behavior are identified and a procedure for correcting these deviations is also presented.

Carefully controlled benchmark experiments are carried out to validate models. The models can then be used for crack-sizing, inversion and for model based probability of detection (POD). For further detail see work done in this area [1-12].

1.1.1 Experimental Configuration

The experimental configuration is shown in Fig 1.1, where a cylindrical air-cored coil is placed over a plate and the measurement is taken with a constant lift-off L_1. As shown in Fig 1.1 the plate lies on the x-y plane while the axis of the coil is parallel with the z-axis. An impedance analyzer, Agilent 4294A, was used to take the impedance measurements. The impedance analyzer was controlled by a Pentium-II PC through ethernet. The coil was connected to the impedance analyzer through a standard 0.3 inch low capacitance TV antenna ribbon cable.

The same setup was used for the edge effect measurements. In this case the coil was moved over the edge of the plate and the change in the impedance of the coil with respect

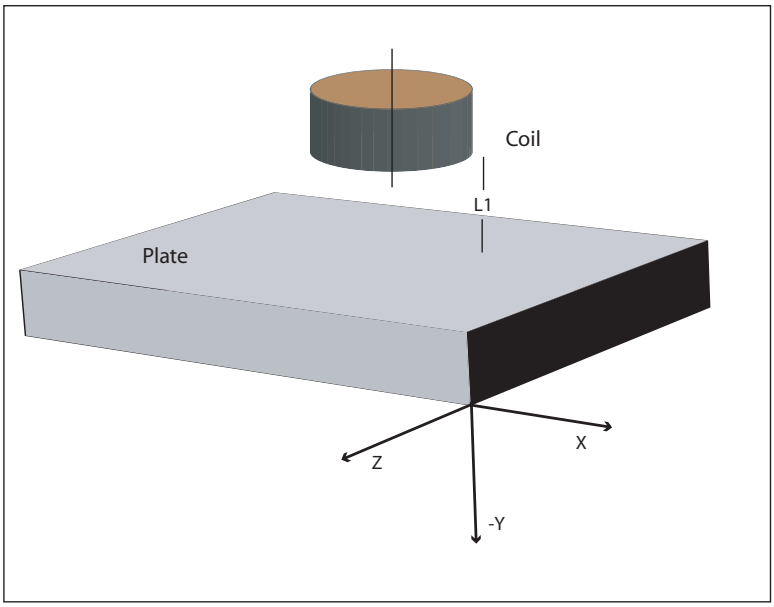

Figure 1.1 Geometry of the benchmark experiment: circular air-cored coil positioned above a flawless Aluminum alloy plate

to the position was measured to test a model for plate edge behavior. Edge effect results are explained in section 1.1.10

1.1.2 Coil Construction

The coil used in the experiment was obtained from D. J. Harrison, L. D. Jones and S. K. Burke and it had been perviously used by them for benchmark experiments in eddy current testing [1]. The description of the coil construction is as follows. "It was constructed by layer-winding self-bonding copper wire onto a captive perspex former. The windings were consolidated by heating using an air-gun and the assembly was potted, remounted in a lathe and the base machined off to give the required geometric lift-off. This procedure allowed a very small value of lift-off to be achieved" [1]. The proportions of the coil were chosen to maximize the ratio of coil inductance to coil resistance, and the effect of stray capacitance due to the leads was minimized by using a 0.3 inch standard low capacitance TV antenna ribbon cable. The measured coil parameters and the electrical parameters are given in Table 1.1. The

electrical parameters were measured with Agilent 4294A impedance analyzer. The measured values were found using a digital vernier caliper. The outer radius was assigned a nominal value as although the measurement is accurate, it does not necessarily represent the true outer radius of the ideal coil carrying uniform current density. Rather, it represents the highest points of the coil and is likely to over estimate the true value. The outer radius is corrected later-on by minimizing the RMS error between theory and experiment and the true value is obtained (this procedure is explained in section 1.17). Similarly, the coil lift-off represents the lift-off at the time of coil construction but the true lift-off while the coil is sitting on the Aluminum plate may be larger due to irregularities in the surface of the Aluminum plate and the thickness of the lubricant layer applied to ensure smooth transition of the coil-probe on the plate. Thus, it is also given a nominal value at this point.

Table 1.1 Measured Coil Parameters [1]

Nominal outer Radius	7.50 mm
Inner Radius	2.51 mm
Length	4.99 mm
Nominal Lift-off	0.10 mm
Number of turns	4000 ± 1
DC inductance	100.45 mH
DC resistance	689.5 Ω

1.1.3 Test Specimen

The specimen used for the test was an 2024-T3 Aluminum alloy plate. The nominal electrical conductivity of the plate was obtained by using a conductivity meter and was found to be 17.1 MS/m at room temperature, which is typical of the 2024-T3 plates [13]. The dimensions of the plate are given in the Table 1.2. The dimensions are large enough that the measurement can be made without experiencing any edge effects.

Table 1.2 Measured Plate Parameters

length	254 mm
Width	254 mm
Thickness	4 mm
Conductivity(nominal)	17.16 MS/m

1.1.4 Overview of the measurement technique

This section explains briefly the actual measurement technique that was used to collect the data. The impedance data was collected as a function of frequency instead of coil position, as the coil was stationary. The impedance analyzer used was Agilent 4294A. It was connected to a Pentium-2 PC through ethernet. The coil was placed on the surface of the plate using an X-Y scanning frame interface connected to the PC. The frame has the capacity to move the coil in either direction at the increments of 0.1 mm. The coil was mounted on a secure holder and care was taken to make sure that it touched the surface of the plate at a constant pressure, thus ensuring an almost negligible and constant lift-off.

The measurements were taken using a software utility written for this purpose. The whole procedure was computer controlled, thus minimizing random errors introduced through human involvement. The scan was taken at 32 frequencies. The lower frequency limit was selected as 250 Hz and the upper limit as 50 kHz. The 32 frequencies were spread between these two limits at equal logarithmic intervals. This frequency range selected corresponds to a range of skin depth from 6.5 mm (250 Hz) to 0.5 mm (50 kHz). In order to further reduce the random errors, 16 measurements were taken at each frequency and then averaged.
In order to ensure accuracy of the scans the following precautions were also taken:

(i) Movement of the antenna cable with respect to the earth or metallic structures could change the capacitance of the coil to earth, thereby reducing the accuracy of the measurement. Thus, special care was taken to ensure that the cable remained stationary. This was done by taping the cable with a nearby wooden table. This ensured that the cable was not in contact with any metallic surface, was straight as possible and did not move with respect to the earth. The

effect of stray capacitance on the measurement and a way to remove this effect is mentioned in section 1.1.5 and 1.1.6.

(ii) To make sure that the coil did not scratch the surface of the Aluminum plate during the edge-effect measurements; thereby damaging the plate as well as itself in the process, a good quality flat Aluminum plate was chosen. The Aluminum plate was also carefully polished to remove any scratch marks introduced through normal handling and then it was lubricated by a thin layer of WD-40 synthetic lubricant to minimize the friction between the coil probe and the surface of the plate.

(iii) Precautions were also taken to minimize the effect of changes in temperature. A change in temperature was expected to change the value of coil lift-off and conductivity from experiment to experiment. Thus, the correction procedure, described later in section 1.1.6, was repeated each time a new dataset was taken. In addition, to minimize the effects of temperature variation the duration of individual scans was kept to a minimum.

1.1.5 Correction for Nonideal Coil Behavior

"Theoretical models for eddy-current NDE assume that the probe coil is an ideal conductor carrying a uniformly distributed current. In practice, any real coil exhibits self-capacitance and resistance as well as additional capacitance associated with the leads. Furthermore, in a real coil, the current distribution is nonuniform, first because of winding irregularities, and second because the electrical currents are confined to discrete positions defined by the windings. In addition, skin and proximity effects give rise to nonuniform current distributions within the wires themselves. These deviations from ideal behavior must be taken into account if good agreement between theory and experiment is to be obtained over a significant frequency range. In the benchmark experiments presented here, the impedance data and experimental parameters are corrected to remove any deviations from ideal coil behavior. In this way. the resulting data can be used directly in any theoretical calculations of defect size and shape" [1]. There are two distinct elements in the correction procedure. First, as described below in

section 1.1.6, the experimental impedance data must be corrected to eliminate the effects of stray capacitance and DC coil resistance. Second, deviations from the ideal coil geometry must be corrected by using effective values of the coil outer radius and lift-off in preference to the geometric measured parameters presented in Table 1.1. As described later in section 1.1.7, these effective coil parameters are determined by fitting the corrected impedance data using well-established theoretical model of Dodd and Deeds for an air-cored coil above a conducting half-space [2]. The later procedure was also used to determine the plate conductivity and overcomes some of the difficulties in obtaining accurate values of coil lift-off and plate conductivity by direct measurement. The correction procedure mentioned below in section 1.1.6 was developed by D. J. Harrison, L. D. Jones and S. K. Burke and was used by them in a previous benchmark experiment [1].

1.1.6 Correction Procedure

A practical eddy-current probe not only exhibits inductance but self-capacitance and resistance as well. The equivalent circuit of the coil is shown in the Fig 1.2. In the figure R_s and C_s represent the series resistance and capacitance respectively, Z_c is the reflected impedance due to eddy current induction in any neighboring conductors, R_o and L_o are the DC resistance and inductance of the coil and C_L represents the lead capacitance. These are the major component of of the equivalent circuit but any behavior that is not represented by the above is lumped into an unspecified RC network. All of the above mentions elements can be grouped together for convenience into a single parallel network Z_p.

The presence of this parallel network results in the deviation of the coil impedance from the ideal value by an amount that increases with frequency. The deviation is especially marked when it reaches the resonant frequency of the coil in air. Clearly, corrections for the non-ideal coil behavior are required if the impedance data is to be useful beyond the very lowest frequencies.

In order to remove the effects of this parallel network, the experiment data was corrected in the following way. The coil impedance Z_a is measured in air in the selected frequency range

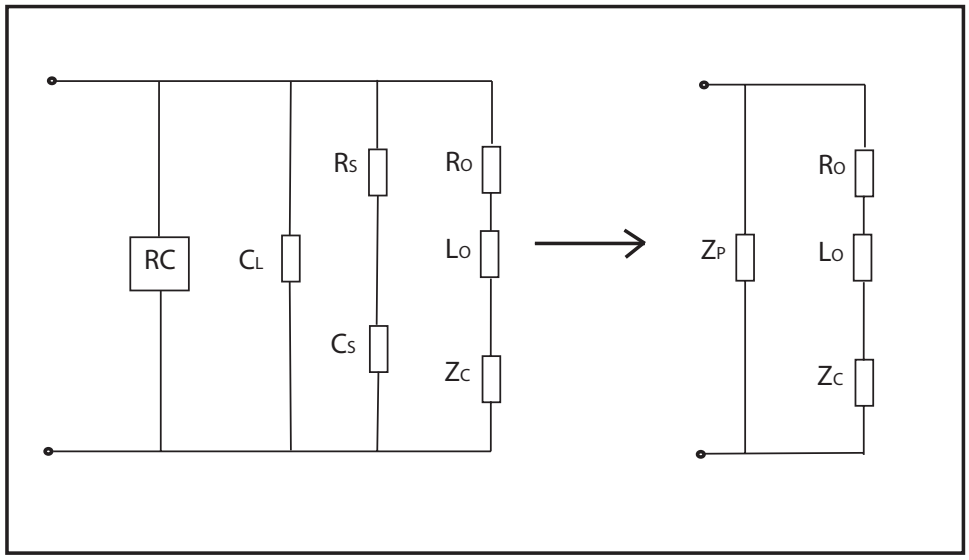

Figure 1.2 Equivalent electrical circuit for an eddy-current probe coil

and the DC values of the resistance R_o and inductance L_o, are determined by extrapolation to the low frequency limit and are used to calculate the ideal admittance Y_o

$$Y_o = 1/Z_o = 1/(R_o + jwL_o) \tag{1.1}$$

This is subtracted from the admittance of coil in air $Y_a = 1/Z_a$ to give the admittance of the equivalent parallel network

$$Y_p = Y_a - Y_o \tag{1.2}$$

In order to correct the measured impedance Z_{plate} obtained by placing the coil on an unflawed region of the test specimen, the admittance of the parallel network is subtracted from the admittance $Y_{\text{plate}} = 1/Z_{\text{plate}}$ to give the corrected impedance

$$Z_{\text{corrected}} = 1/(Y_{\text{plate}} - Y_p) \tag{1.3}$$

Hence the corrected impedance change due to an unflawed test specimen is obtained by subtracting the DC impedance from $Z_{\text{corrected}}$

$$\Delta Z_{\text{corrected}} = Z_{\text{corrected}} - Z_o \tag{1.4}$$

Thus, by following this procedure the effects of the parallel network are eliminated, leaving the impedance characteristics that would have been exhibited by an ideal coil.

1.1.7 Determination of Effective Coil Parameters

Effective values for the coil outer radius and coil lift-off were determined by fitting the corrected impedance data using the theory of Dodd and Deeds for an air-cored coil above a layered conducting half-space [2]. The same procedure was used to determine the exact conductivity of the test specimen.

Outer Radius

The outer radius correction was done by firstly predicting the coil DC inductance from the measured coil values as input data. The value obtained was 101.7 mH, which is slightly higher than the experimental value of 100.45 mH mentioned in table 1.1. This discrepancy was attributed to the value of the coil outer radius, as even though the measurement is accurate, it does not necessarily reflect the true outer radius of the ideal coil carrying a uniform current density. Rather, it represents the highest points of the coil and is likely to over estimate the true value. The outer coil radius was thus treated as a free parameter and was varied until the theoretical value of DC inductance coincided with the experimental value. The effective value of coil outer radius obtained this way was 7.395 mm. This value is only slightly less than the measured value (7.5 mm)and can thus be considered to be a legitimate correction.

Coil lift-off and Conductivity

The effective value of the coil lift-off was determined by minimizing the RMS error between the corrected experimental impedance and the theoretical calculations over the same frequency range obtained from Dodd and Deeds theoretical model [2].

$$\varepsilon^2 = \frac{1}{N}\sum \frac{[\Delta R_{exp}(i) - \Delta R_{calc}(i)]^2}{[\Delta R_{exp}(i)]^2} + \frac{[\Delta L_{exp}(i) - \Delta L_{calc}(i)]^2}{[\Delta L_{exp}(i)]^2} \tag{1.5}$$

In the equation 1.5 the symbols ΔR_{exp} and ΔR_{calc} denote the real part of the corrected experimental impedance change and the real part of the theoretical impedance change respectively. ΔL_{exp} and ΔL_{calc} denote the experimental inductance minus DC inductance and theoretical inductance minus DC inductance respectively.

The lift-off was then kept constant and the conductivity was varied to get the minimum error between theory and experiment, thus obtaining the optimum conductivity of the specimen. The effective parameters obtained by following the above procedure are given in the Table 1.3 below and compared with the measured values from Table 1.1. As expected the effective lift-off is slightly higher than the measured value and the effective value of the conductivity should be taken as the true conductivity value of the test specimen.

Table 1.3 Comparison of Nominal Measured Parameters and Effective Parameters Obtained by Least Squares Fits Using the Theory of Dodd and Deeds

Parameter	**Measured Value**	**Effective Value**
Coil outer Radius	7.50 mm	7.395 mm
Coil Lift-off	0.10 mm	0.29 mm
Conductivity	17.1 MS/m	17.4 MS/m

1.1.8 Results

The results from the experiment are shown in Fig 1.3

1.1.9 Significance of cable separation

Fig 1.5 shows the comparison between the standard 0.3 inch antenna ribbon cable and a 1 inch separation ribbon cable . The antenna cable is made up of two low capacitance, multi-thread wires running parallel to each other. The 0.3 inch separation is the separation between the two parallel wires. The same is the case with the 1 inch separation cable and it was hand-made by separating two conducting wires and sandwiching them between a layer of duct tape. Comparison between the two uncorrected curves in the figures show that the greater the separation between the wires of the cable, the better the result, meaning that the

deviation between the uncorrected experiment data from the theoretical data is less for the 1 inch separation cable. Greater separation reduces the mutual capacitance between the wires and reduces the non-ideal deviation at higher frequencies. It is interesting to note that after applying the correction procedure both cables perform almost identically. Thus, the correction procedure is validated in this way. For benchmark comparison, the results from 0.3 inch cable were preferred as the cable was a standard and commercially available and it gave better fit between the theory and the experimental results. The results are shown in Fig 1.3

Fig 1.4 shows the same results as in Fig 1.3 but with the 1 inch cable. You can see the reason these results were rejected in favor of Fig 1.3 (0.3 inch cable). In Fig 1.4 on the resistance curve at low frequency, there is a deviation between the uncorrected experiment data (open circles) and the corrected experiment data (filled circles). This deviation is not present for the 0.3 inch cable at the same frequencies. At low frequencies the uncorrected and corrected data should be almost identical, with a very little error and this is true for the 0.3 inch cable. Also, for the 1 inch cable (Fig 1.4) there is a deviation between the theory and the corrected experiment reactance data at high frequencies. Ideally this deviation should have been absent or minimal, which is not the case with the 1 inch cable. The 0.3 inch cable performs better in comparison, so the results from the 0.3 inch cable were selected for the benchmark experiment. Please keep in mind that the 0.3 inch cable was a standard commercial product whereas the 1 inch cable was hand-made.

1.1.10 Benchmark Experiment showing Edge Effects

Fig 1.6 onwards show edge effects for the same Aluminum alloy plate used in section 1.1.3. In Fig 1.6 to Fig 1.10 the coil is moved from free space towards the edge of the plate. The data is normalized to the ideal isolated coil reactance X_o. The coil impedance in free space is then subtracted from the entire data, which would caused it to go to zero over free space. Fig 1.11 to Fig 1.15, show the reverse edge effect, which means that here the coil moves over the edge of the plate and goes into free space. This data is also normalized to X_o and free space impedance is subtracted. The above Figures were plotted with respect to the coil position.

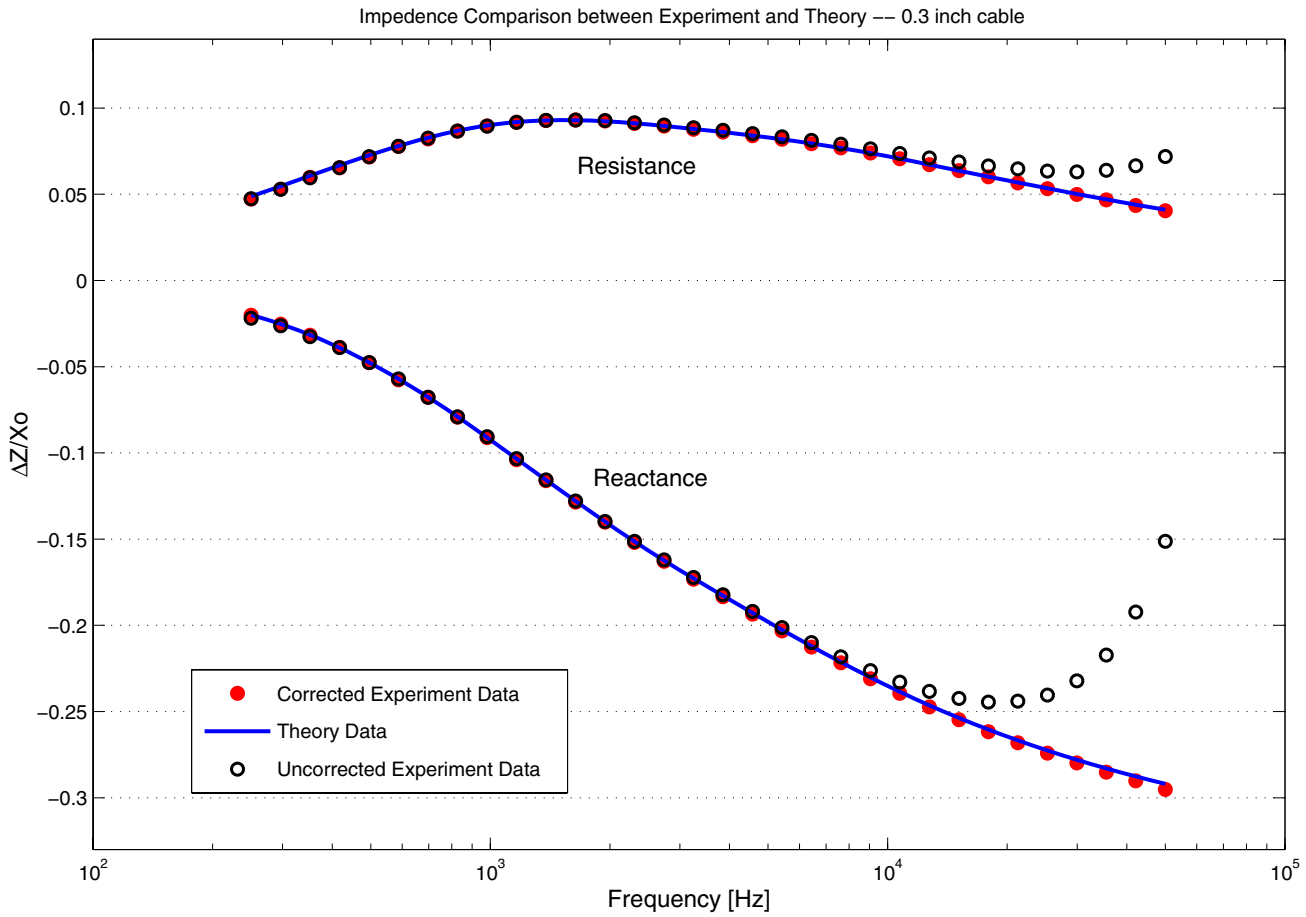

Figure 1.3 Change in coil impedance due to an unflawed region of plate, normalized to the ideal isolated coil reactance X_o. The open circles denote the uncorrected experimental data, the filled circles denote the corrected experimental data and the solid curve represent the theoretical calculations using the effective coil parameters and Dodd and Deeds Theory [2]. The results were obtained using the 0.3 inch cable

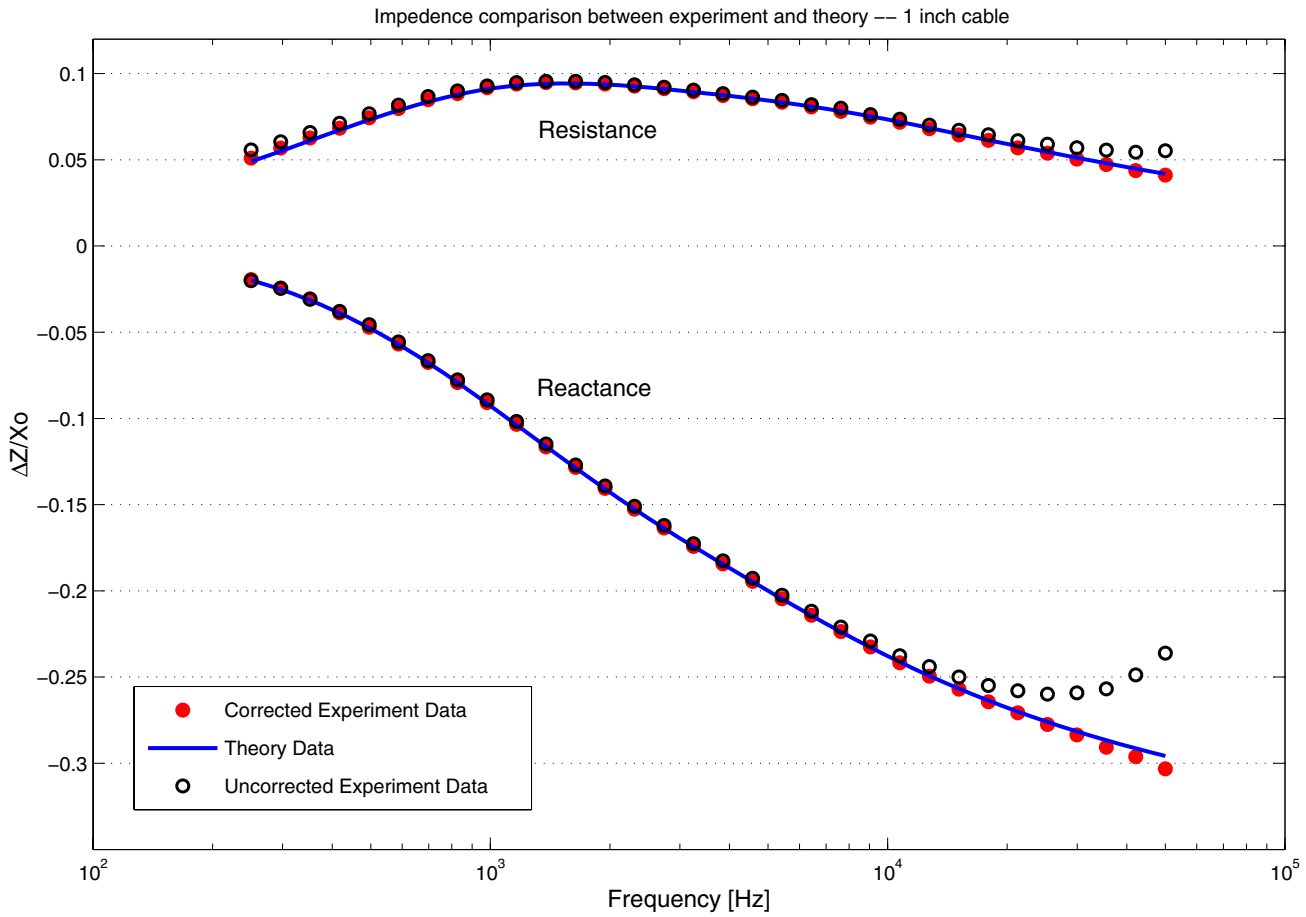

Figure 1.4 Change in coil impedance due to an unflawed region of plate, normalized to the ideal isolated coil reactance X_o. The open circles denote the uncorrected experimental data, the filled circles denote the corrected experimental data and the solid curve represent the theoretical calculations using the effective coil parameters and Dodd and Deeds Theory [2]. The results were obtained using the 1 inch cable

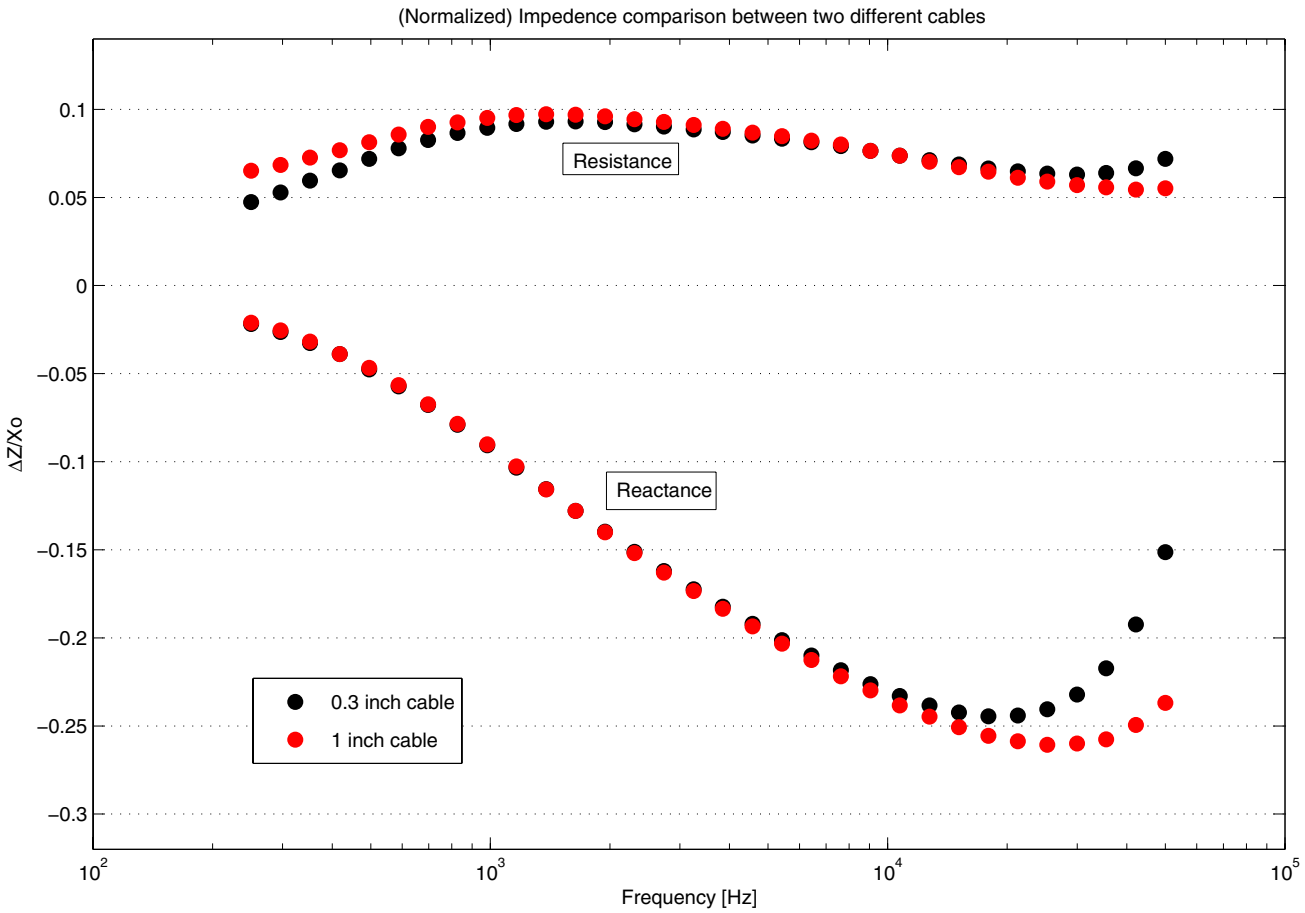

Figure 1.5 Impedance comparison between the 1 inch cable and the 0.3 inch cable. For the comparison, the uncorrected experiment data was used. Red circles for the 1 inch cable and Black circles for 0.3 inch cable

For this experiment five frequencies were used, 1 kHz, 2.5 kHz, 6.3 kHz, 15.9 kHz and 40 kHz. To reduce random errors, 16 measurements were taken at each frequency and then averaged to give one data point at that frequency. To ensure the accuracy of the data, precautions described in section 1.1.4 were also applied. The correction procedure described in section 1.1.6 was also used.

Fig 1.16 to Fig 1.20 show the comparison between the impedance measured while the coil was moved from the plate edge towards free space to the impedance measured when the coil was moved from free space towards the plate edge, at a particular frequency. For this comparison, one set of data was flipped. The comparison graphs show a small deviation when the coil moves over the edge. This deviation is not present in the two sets of data, when the coil is either in free space or on the plate surface. This would suggest an inconsistency in the plate's edge itself. This might also suggest that the coil passed over a different edge when it moved off the plate, from the one when it moved towards the plate.

These edge results are based on experimental data. A theoretical data was not available for the particular plate, so a comparison between theory and experiment could not be performed.

1.1.11 Conclusion

In this chapter two benchmark experiments were presented. The first one dealt with the verification of theoretical calculations of the impedance change in a coil due to a layered conducting half space. A correction procedure was also presented to correct the deviation in the coil from the ideal coil behavior. The results obtained and presented in Fig 1.3 show a high degree of agreement between theory and experiment. The data obtained through these benchmark experiments can now be used as a reference to validate other models.

The benchmark experiment dealt with the edge effect. Two sets of data were gathered. One where the coil moves off the edge of the plate into free space and second where the coil moves from free space towards the edge of the plate. Data obtained in both cases can be used as a benchmark. Further work needs to be done to obtain a set of theoretical data for the given plate. This benchmark data can then be used to validate the theoretical calculations.

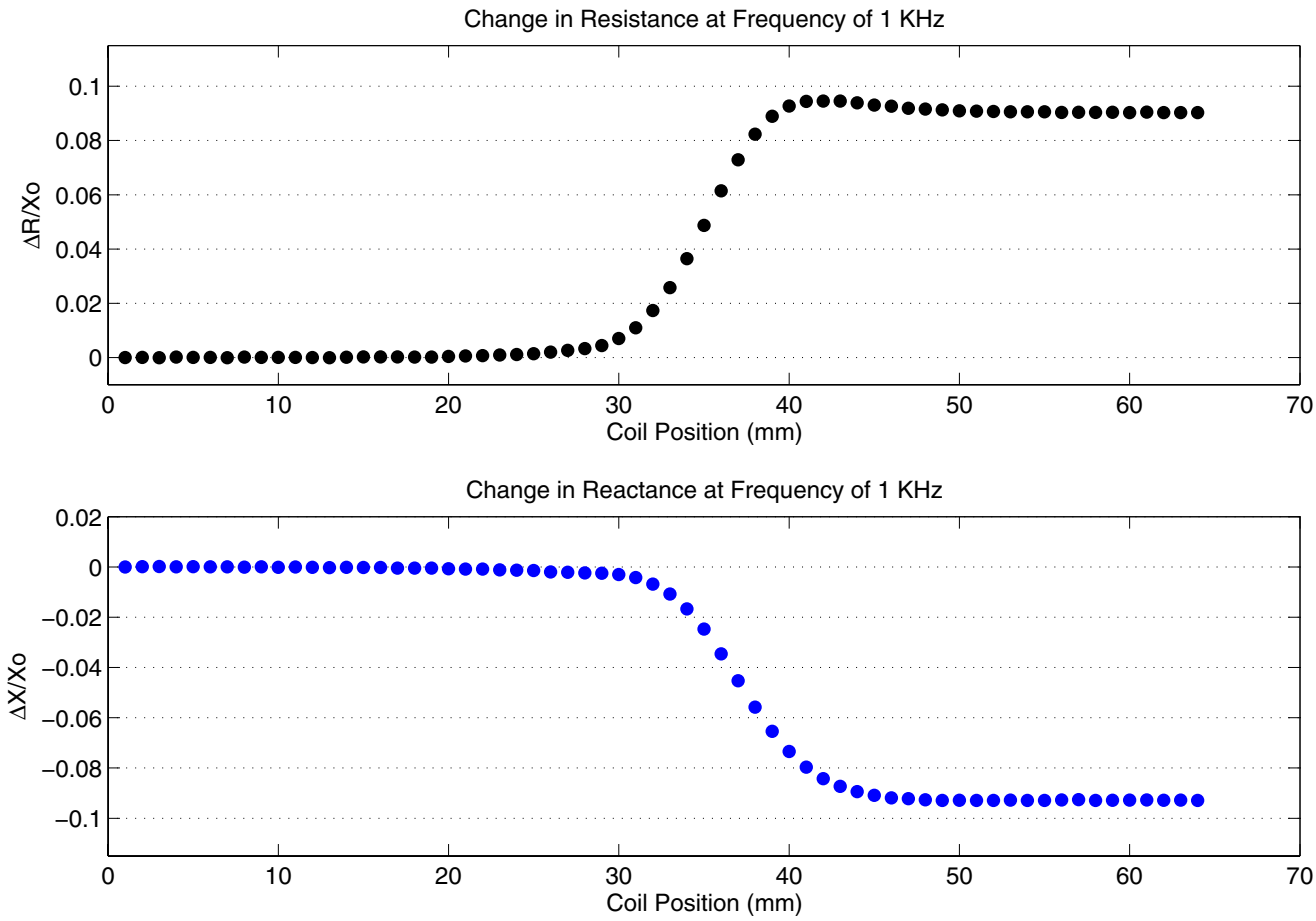

Figure 1.6 Change in coil impedance, as the coil moves from free space towards the edge of the plate, normalized to the ideal isolated (free space) coil reactance X_o and at frequency of 1 kHz

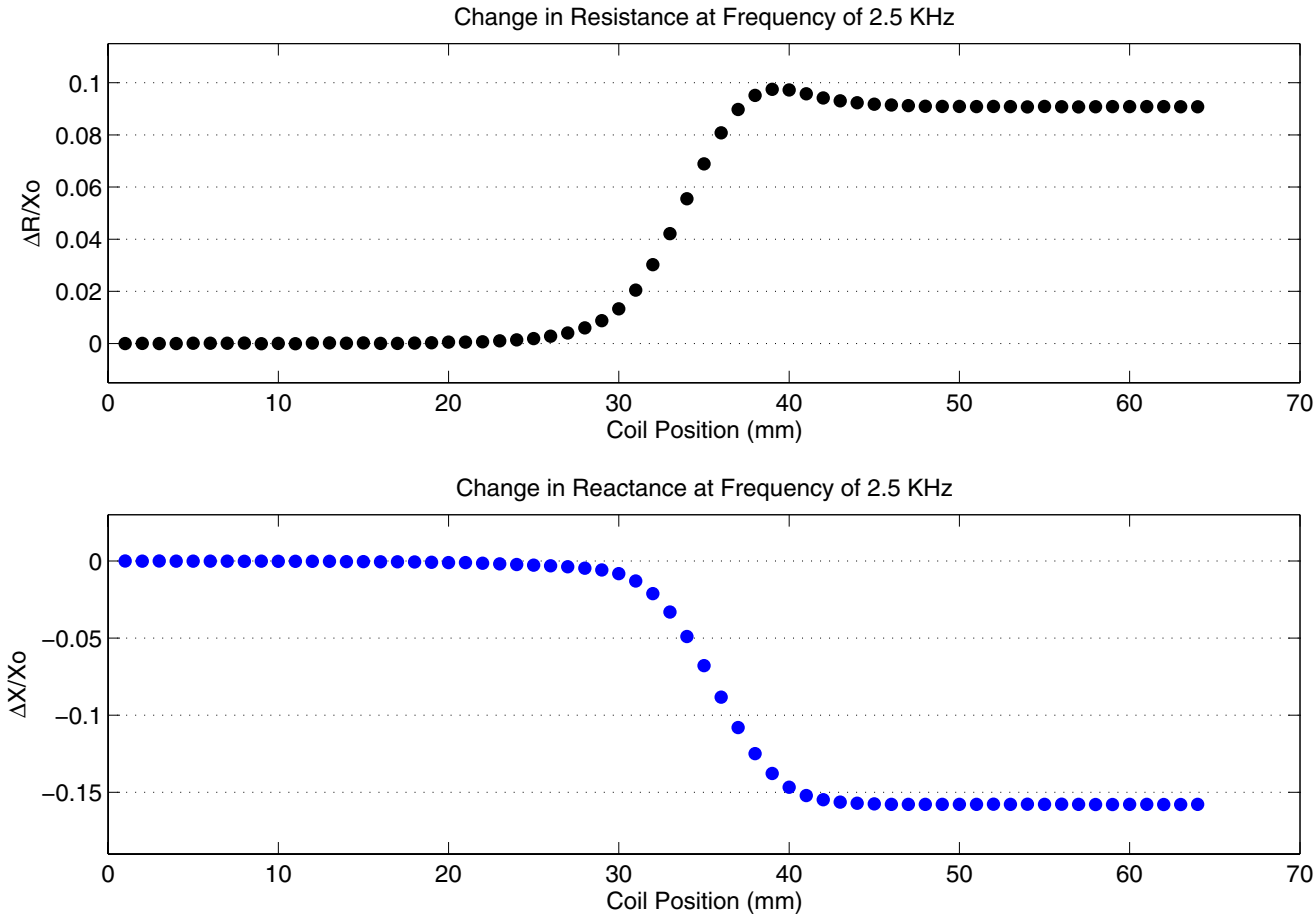

Figure 1.7 Change in coil impedance, as the coil moves from free space towards the edge of the plate, normalized to the ideal isolated (free space) coil reactance X_o and at frequency of 2.5 kHz

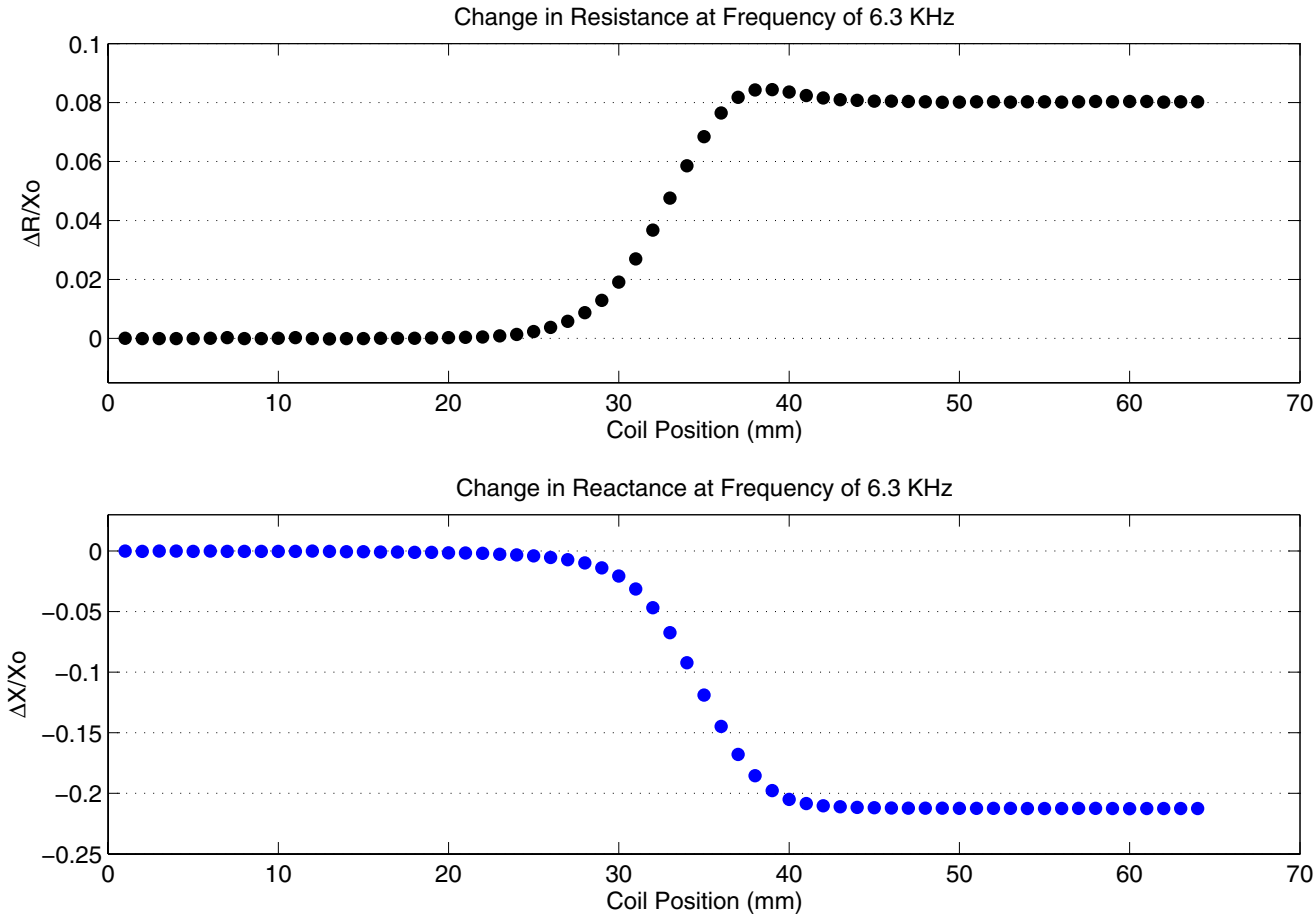

Figure 1.8 Change in coil impedance, as the coil moves from free space towards the edge of the plate, normalized to the ideal isolated (free space) coil reactance X_o and at frequency of 6.3 kHz

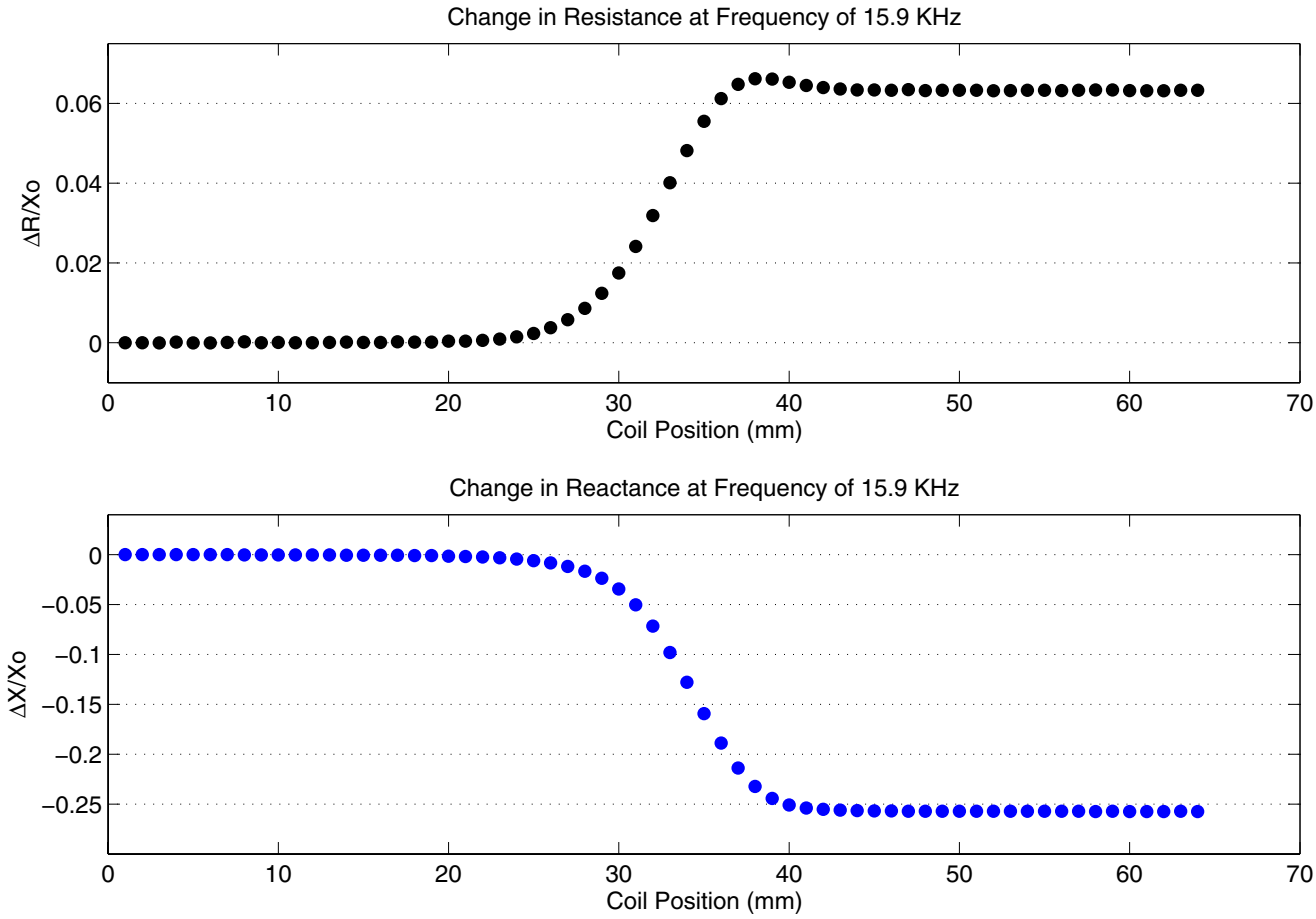

Figure 1.9 Change in coil impedance, as the coil moves from free space towards the edge of the plate, normalized to the ideal isolated (free space) coil reactance X_o and at frequency of 15.9 kHz

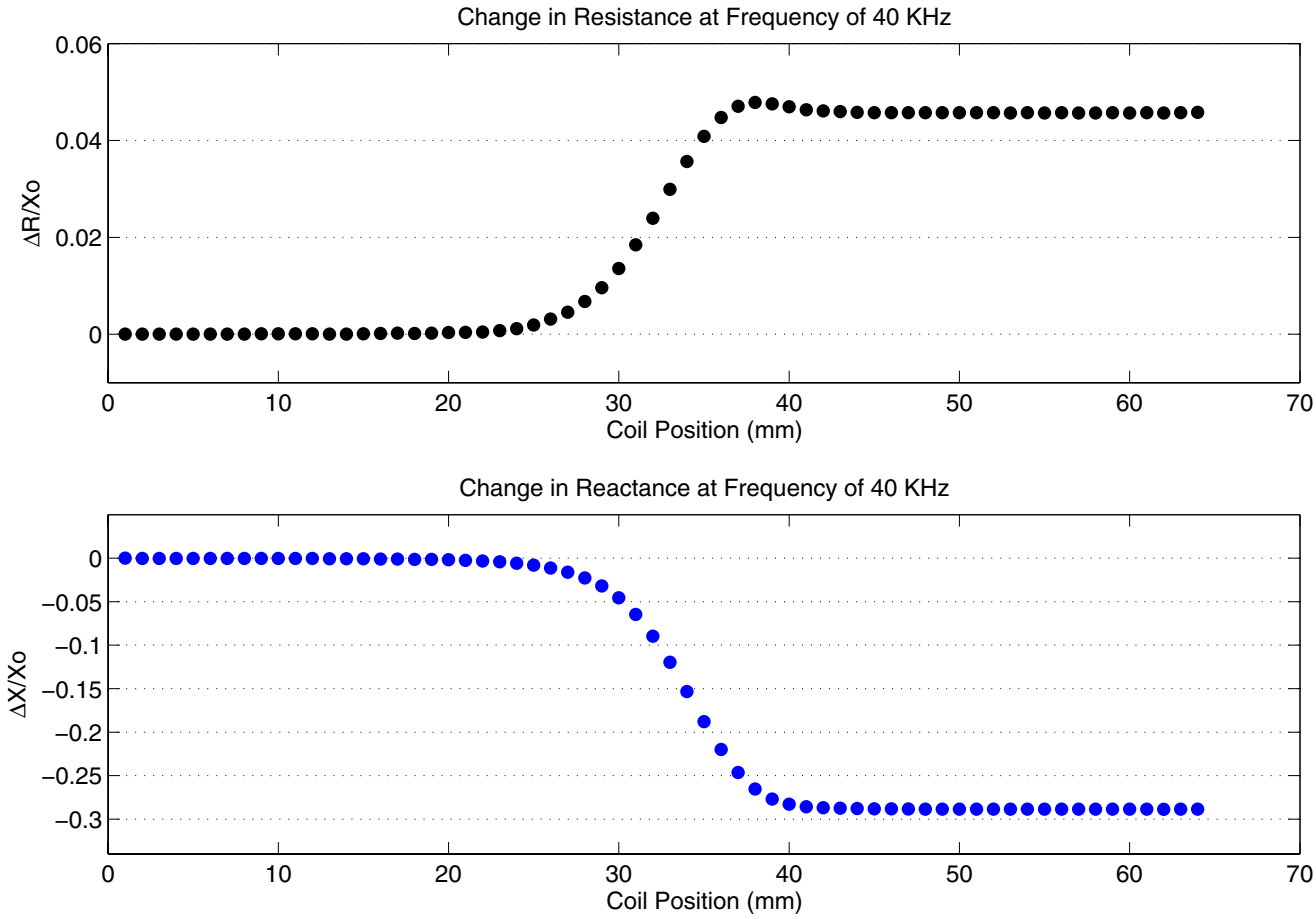

Figure 1.10 Change in coil impedance, as the coil moves from free space towards the edge of the plate, normalized to the ideal isolated (free space) coil reactance X_o and at frequency of 40 kHz

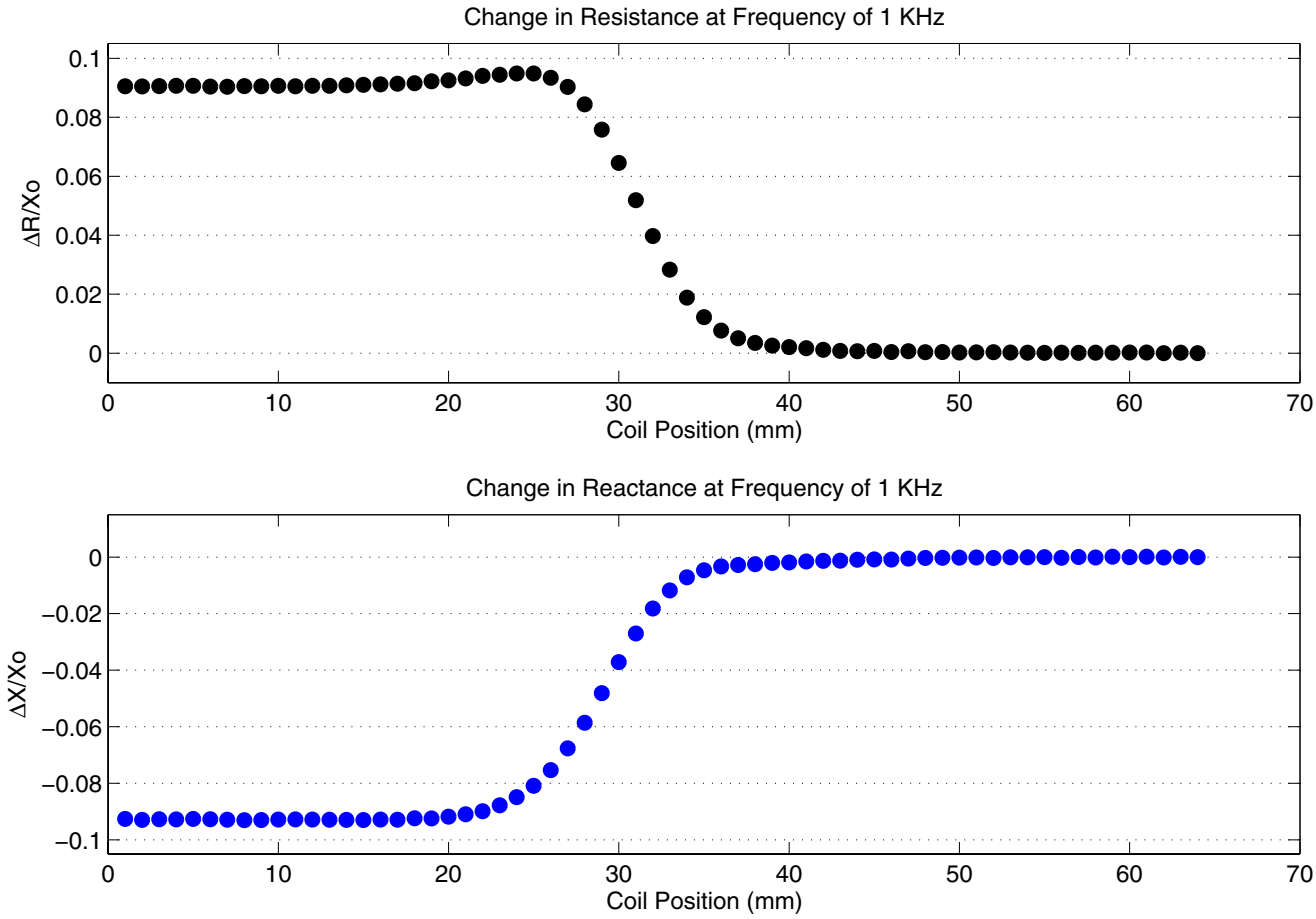

Figure 1.11 Change in coil impedance, as the coil moves over the edge of the plate towards free space, normalized to the ideal isolated (free space) coil reactance X_o and at frequency of 1 kHz

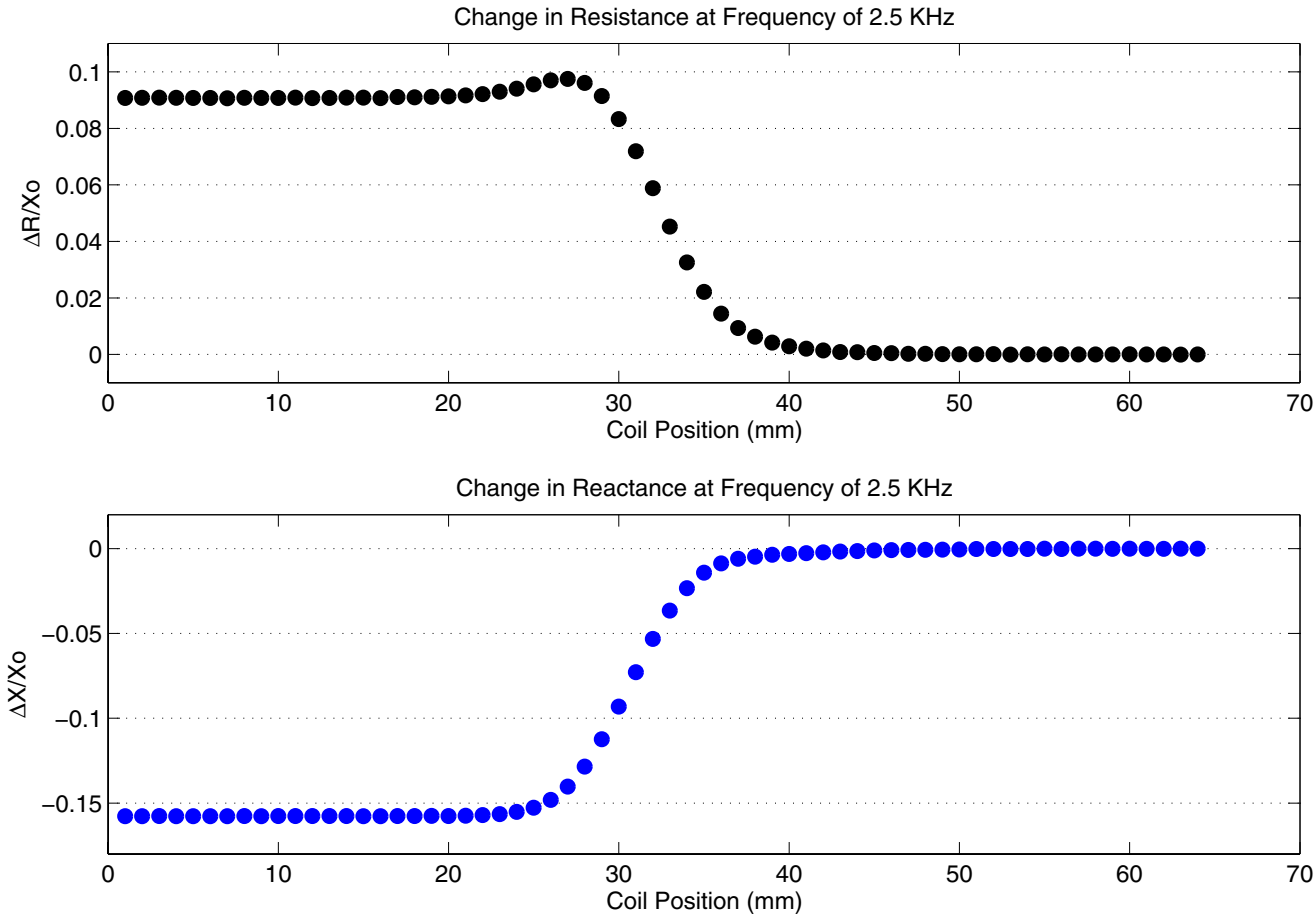

Figure 1.12 Change in coil impedance, as the coil moves over the edge of the plate towards free space, normalized to the ideal isolated (free space) coil reactance X_o and at frequency of 2.5 kHz

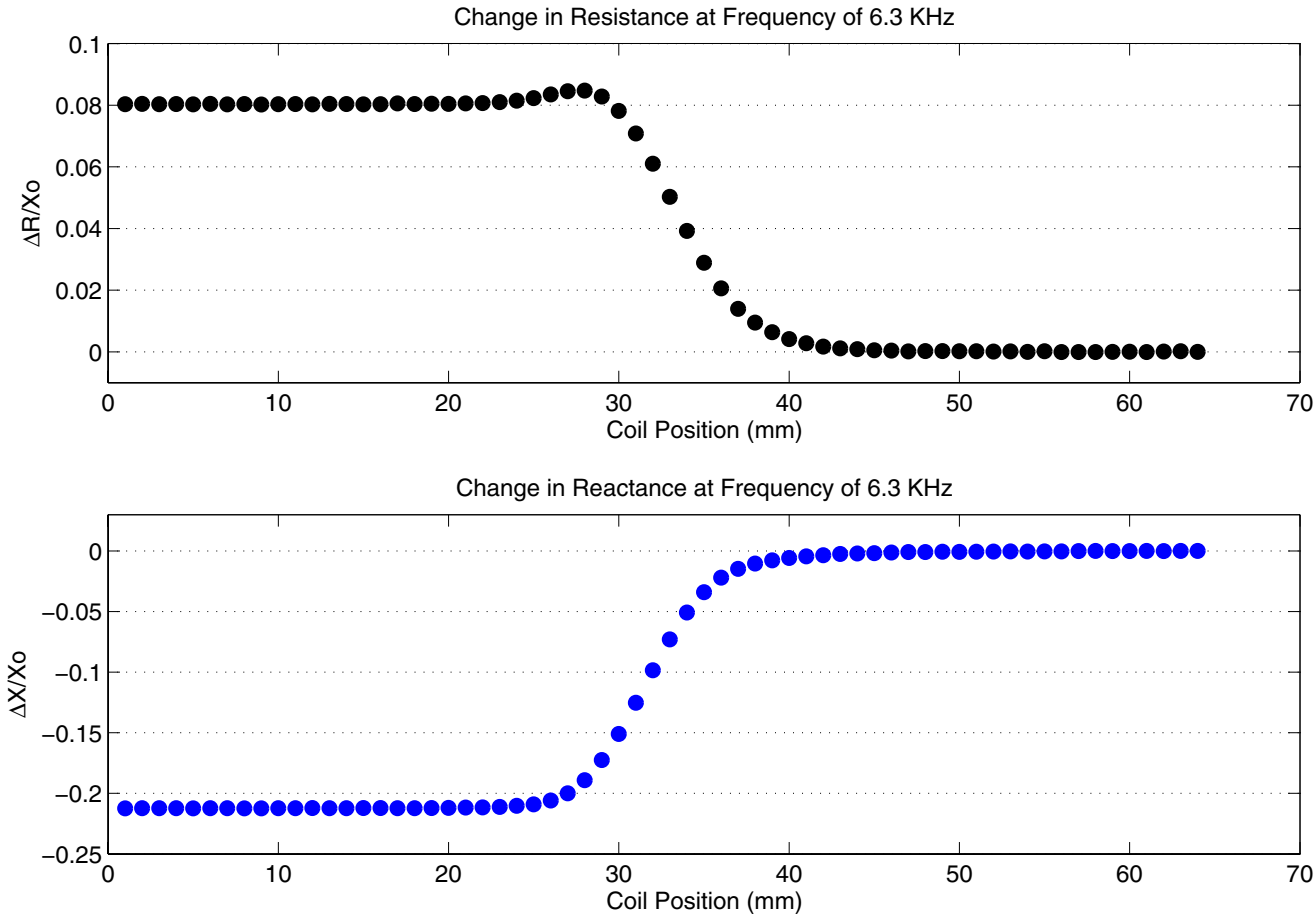

Figure 1.13 Change in coil impedance, as the coil moves over the edge of the plate towards free space, normalized to the ideal isolated (free space) coil reactance X_o and at frequency of 6.3 kHz

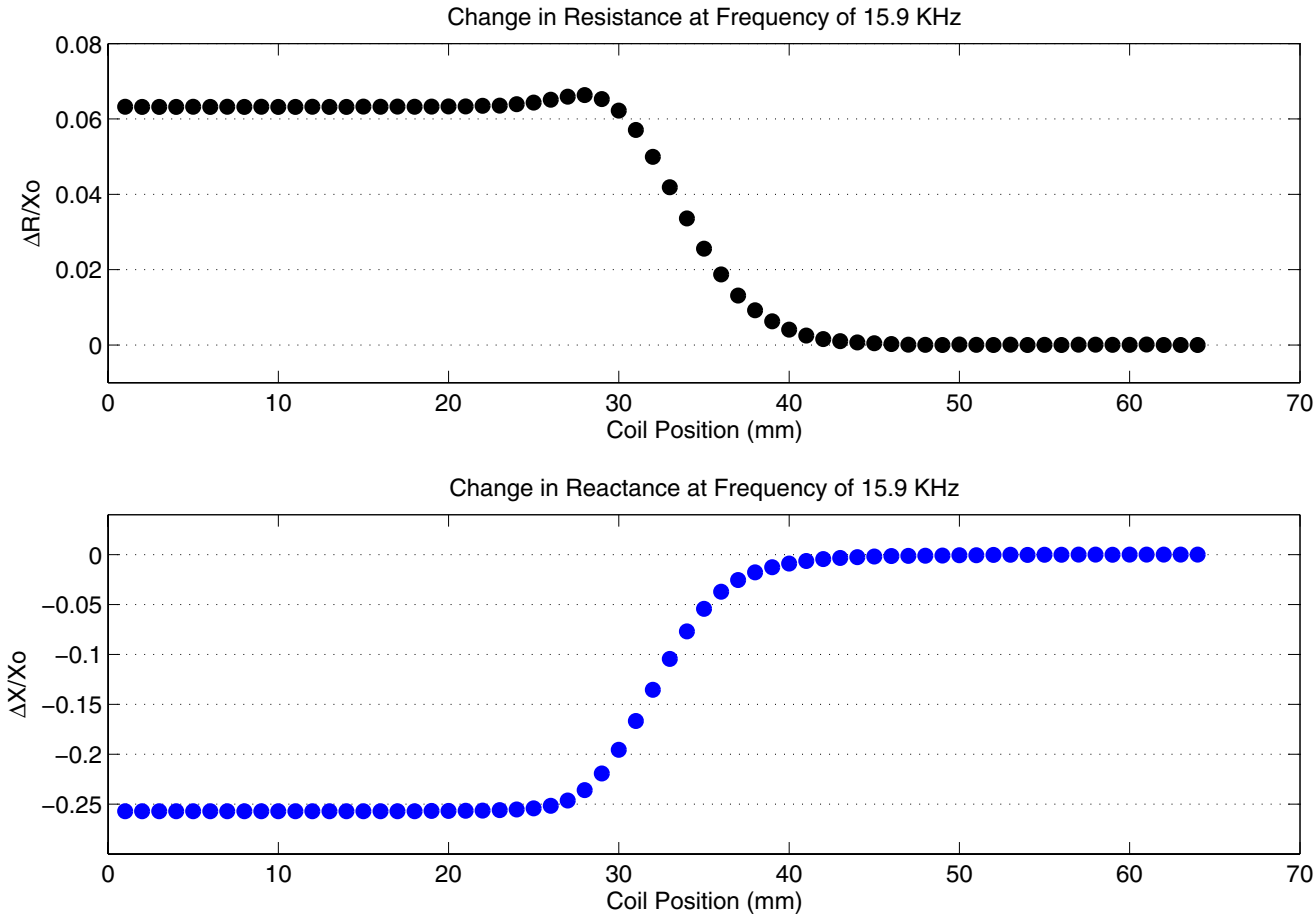

Figure 1.14 Change in coil impedance, as the coil moves over the edge of the plate towards free space, normalized to the ideal isolated (free space) coil reactance X_o and at frequency of 15.9 kHz

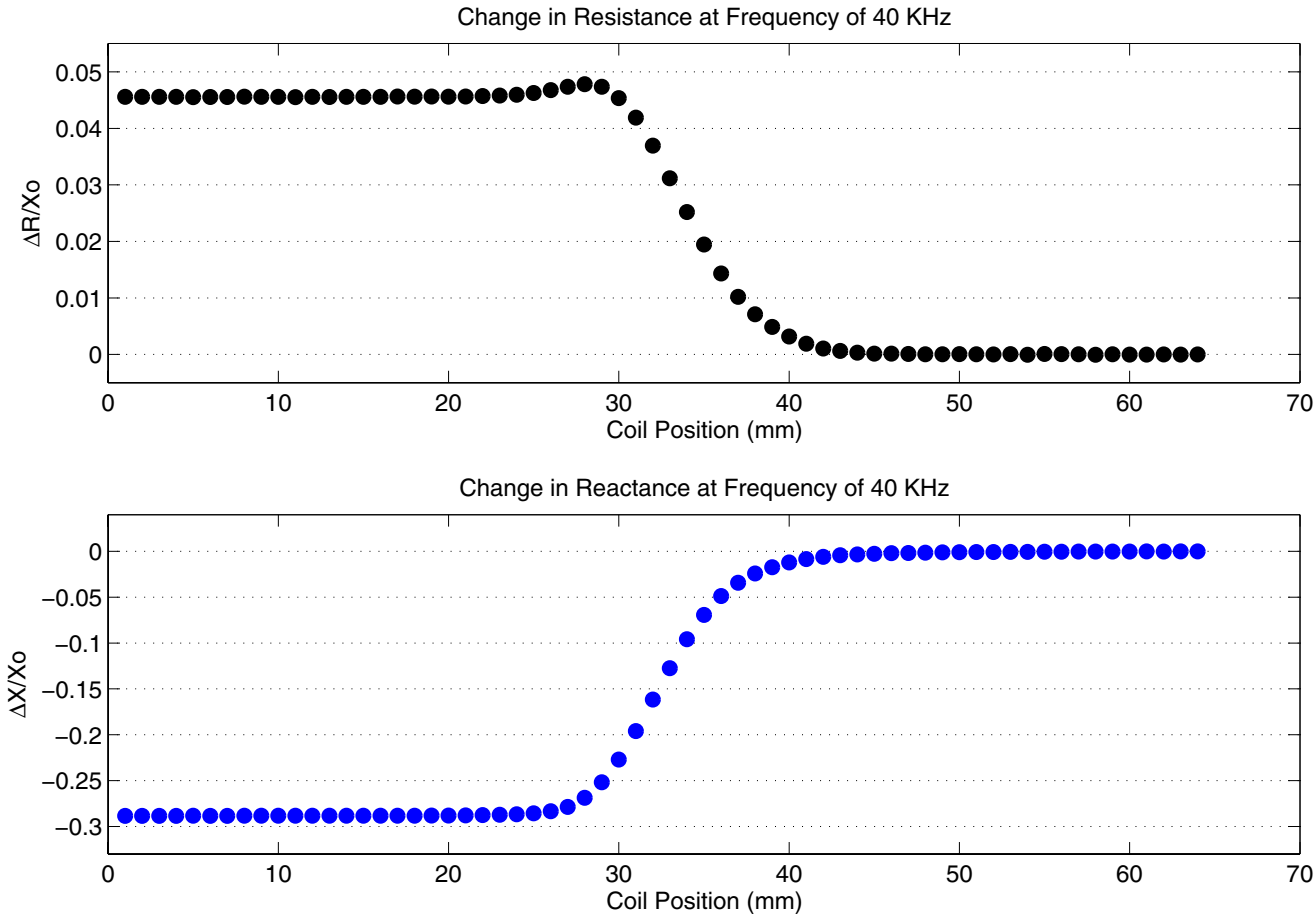

Figure 1.15 Change in coil impedance, as the coil moves over the edge of the plate towards free space, normalized to the ideal isolated (free space) coil reactance X_o and at frequency of 40 kHz

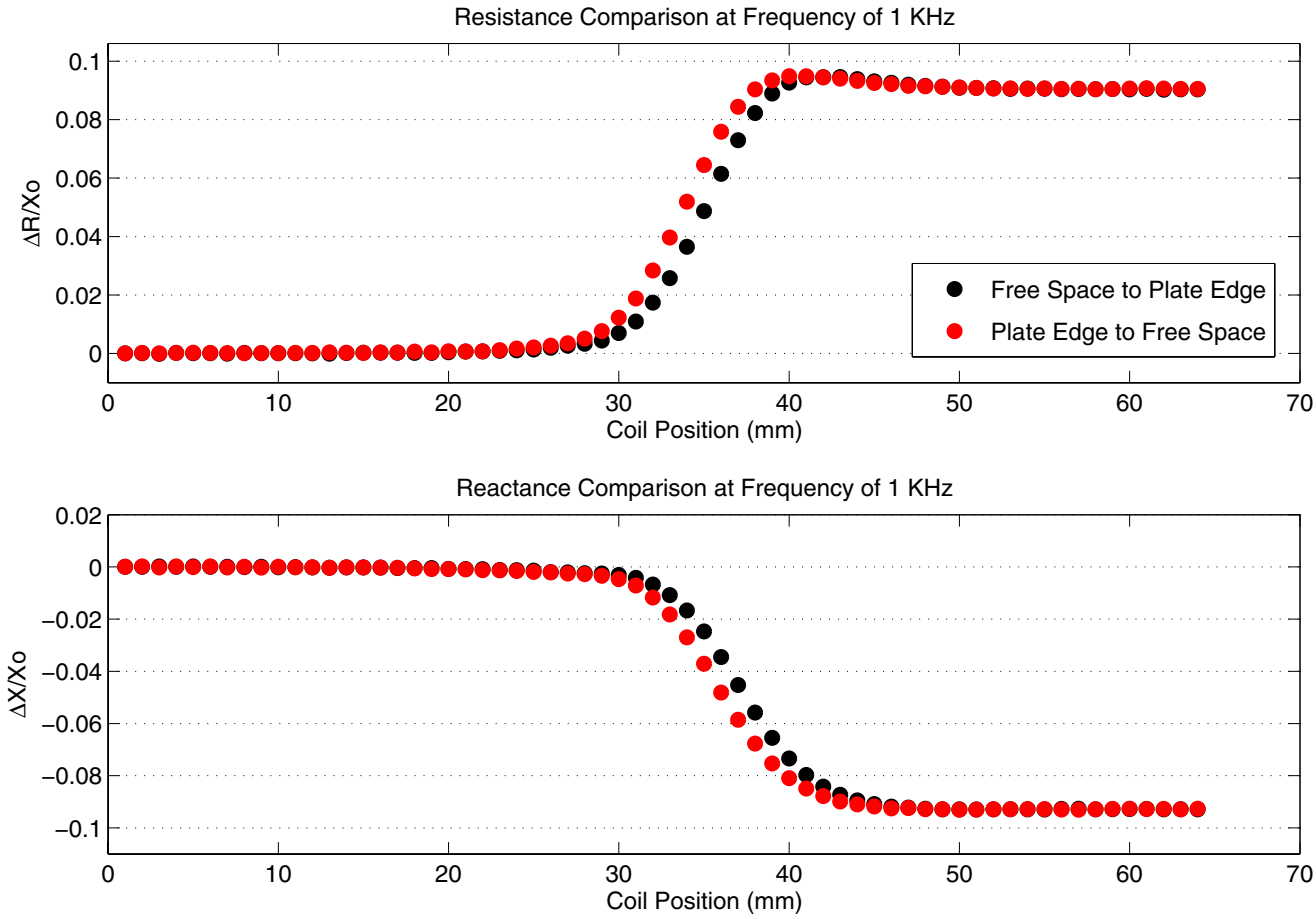

Figure 1.16 Comparison between the change in impedance when the coil moves from free space towards the edge of the plate (black circles) and the change in impedance when the coil moves from the edge of the plate towards free space (red circles), normalized to the ideal isolated (free space) coil reactance X_o and at frequency of 1 kHz

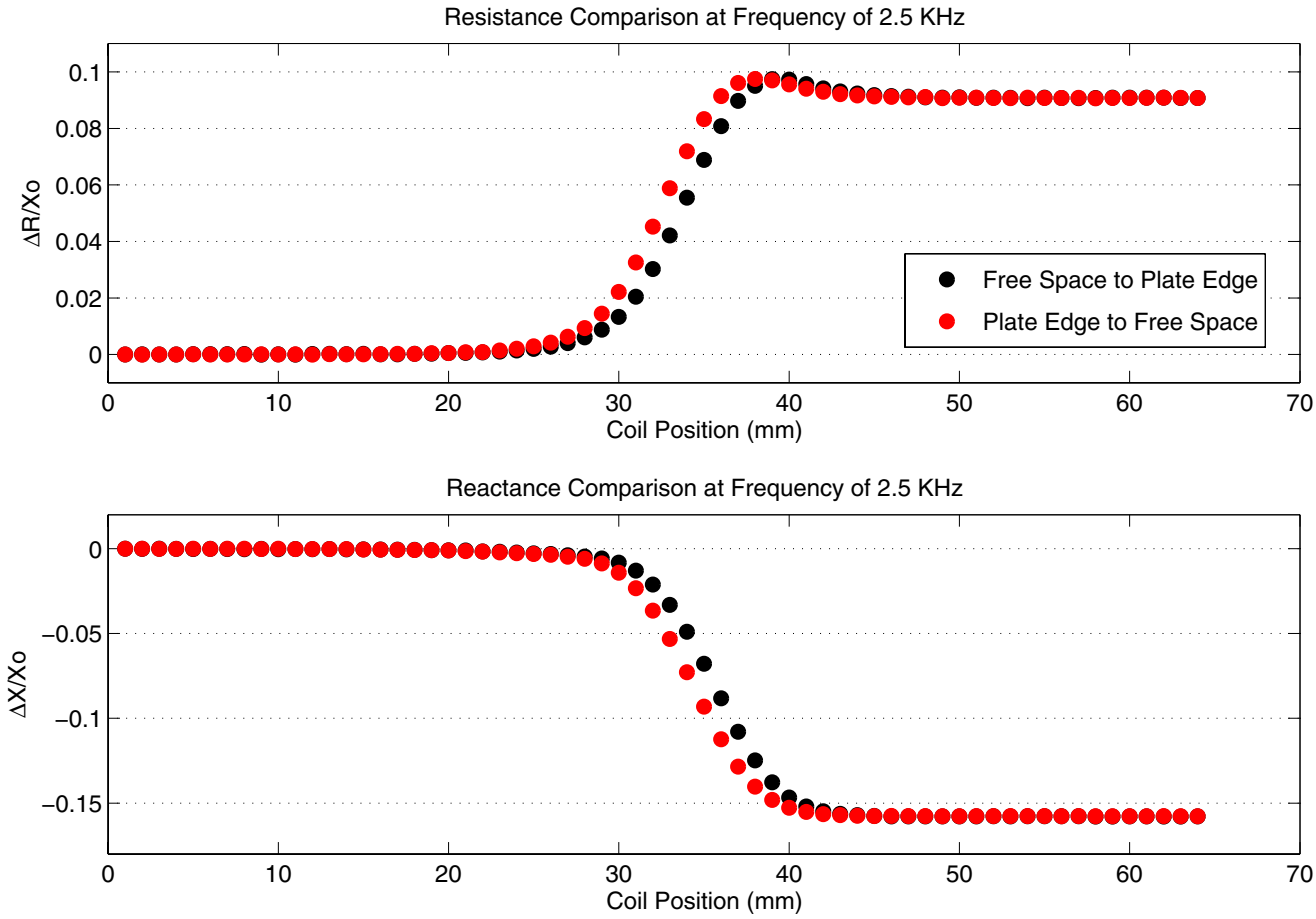

Figure 1.17 Comparison between the change in impedance when the coil moves from free space towards the edge of the plate (black circles) and the change in impedance when the coil moves from the edge of the plate towards free space (red circles), normalized to the ideal isolated (free space) coil reactance X_o and at frequency of 2.5 kHz

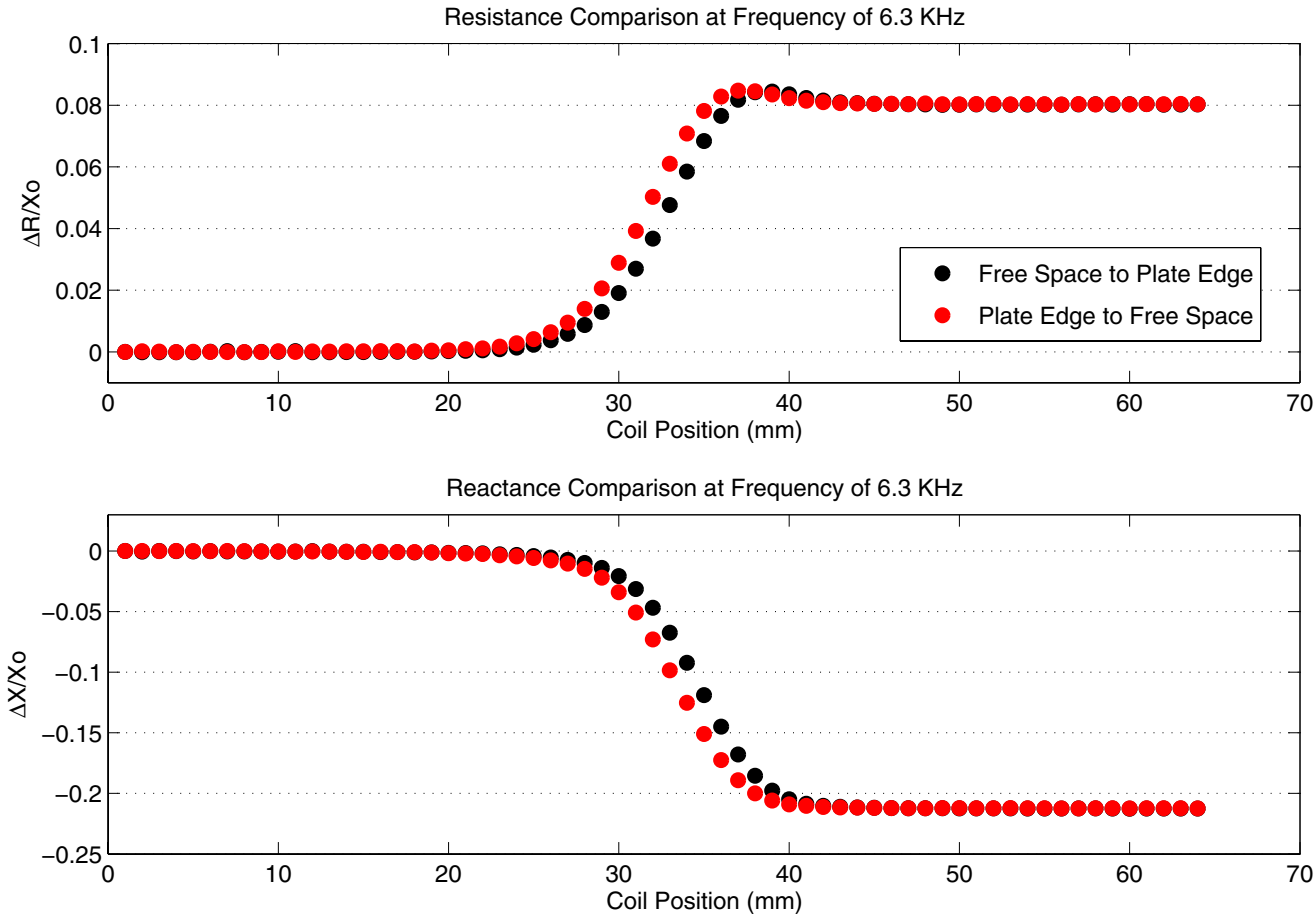

Figure 1.18 Comparison between the change in impedance when the coil moves from free space towards the edge of the plate (black circles) and the change in impedance when the coil moves from the edge of the plate towards free space (red circles), normalized to the ideal isolated (free space) coil reactance X_o and at frequency of 6.3 kHz

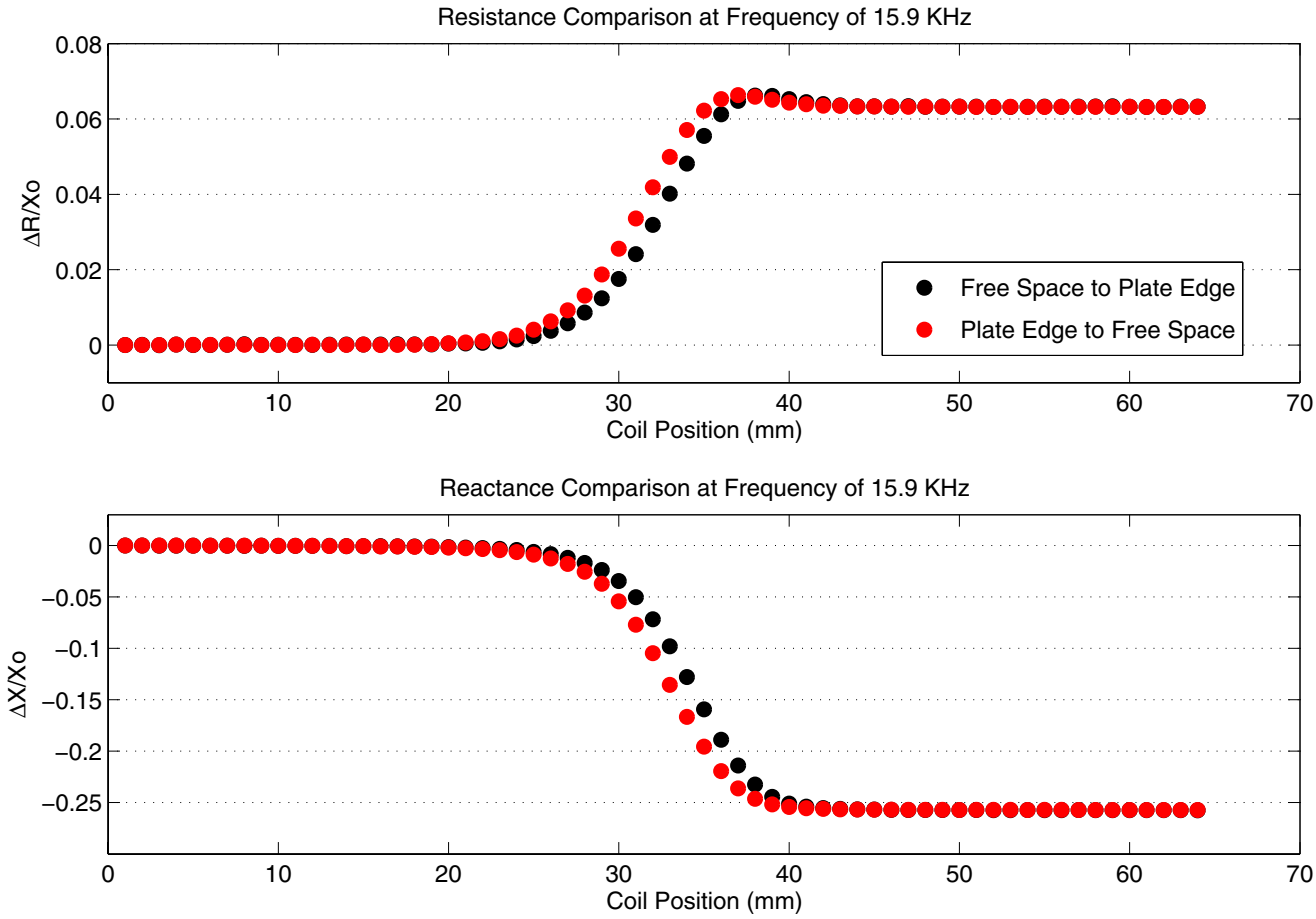

Figure 1.19 Comparison between the change in impedance when the coil moves from free space towards the edge of the plate (black circles) and the change in impedance when the coil moves from the edge of the plate towards free space (red circles), normalized to the ideal isolated (free space) coil reactance X_o and at frequency of 15.9 kHz

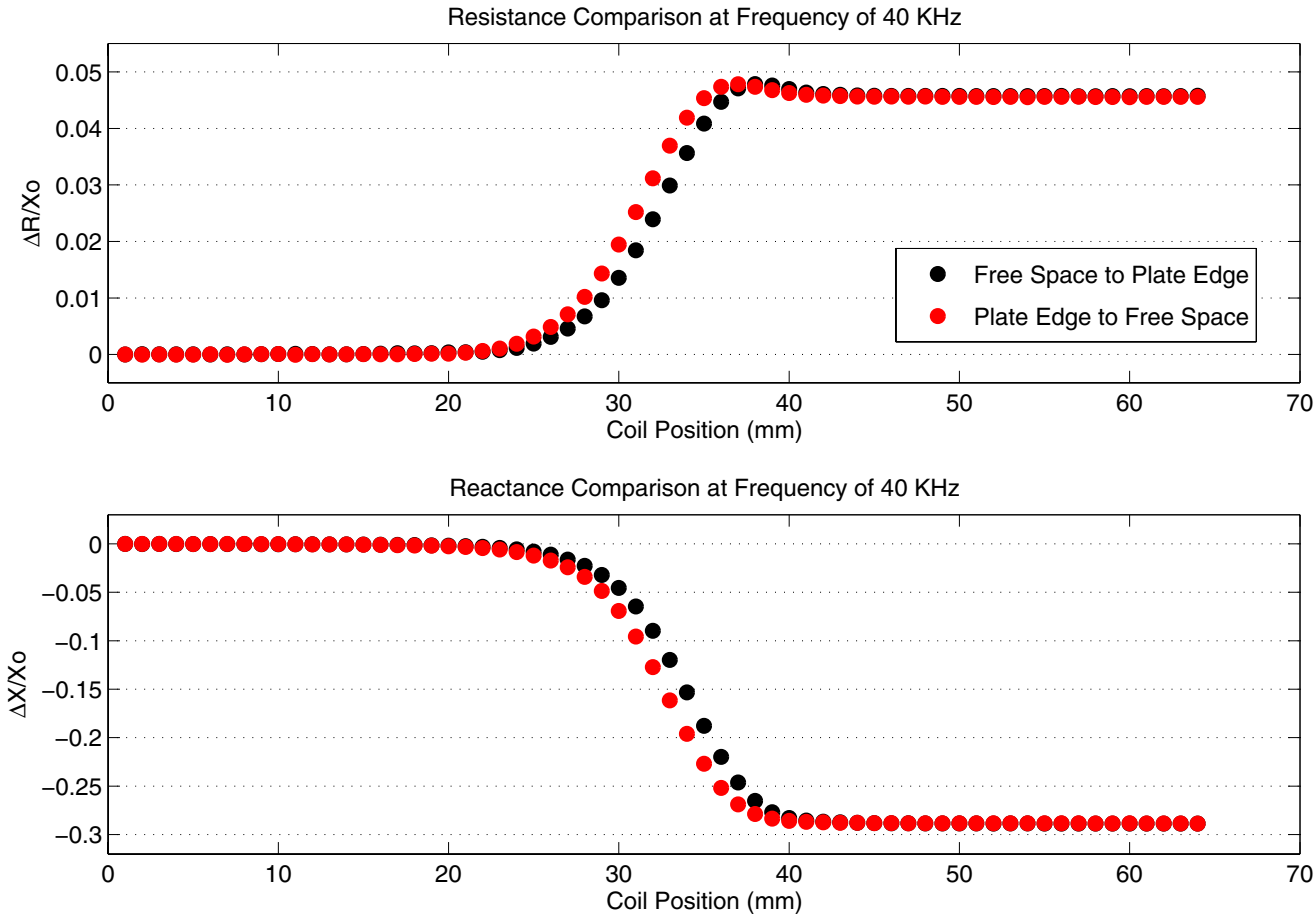

Figure 1.20 Comparison between the change in impedance when the coil moves from free space towards the edge of the plate (black circles) and the change in impedance when the coil moves from the edge of the plate towards free space (red circles), normalized to the ideal isolated (free space) coil reactance X_o and at frequency of 40 kHz

CHAPTER 2. Hall Effect Sensors for Eddy Current Probe Arrays

2.1 Introduction

In this chapter, we describe some technical issues concerning the use of Hall sensors for eddy current probe arrays. First, however is a brief introduction of the Hall effect transducers and their application in industry.

Hall effect is among the most widespread of the technologies used to detect magnetic fields. It's popularity is due to the simple reason that Hall effect transducers can be constructed easily by the standard integrated circuit process used in the microelectronic industry nowadays. Since, it is possible to integrate signal processing circuitry on the same silicon die with the Hall transducer, so usable Hall effect sensors can be fabricated readily and inexpensively. Millions of these devices are produced every year and are used in a wide variety of applications. A few of the places Hall effect transducers can be found are in automobiles: ignition timing, antilock braking systems etc, in computers: disk drive index sensors etc, in industrial controls: speed sensors, encoders etc and in consumer devices such as exercise equipment, cell phones etc.

Knowledge of Hall effect is very old. It was discovered by Edwin Hall in 1879 [14]. In the late 1950s Hall effect transducers were being used to make magnetic measurement instruments commonly used in the laboratories. In 1960s and 1970s, the availability of semiconductor materials enabled the fabrication of high quality Hall transducers. The miniaturization technology made it possible to build Hall effect sensors on integrated circuits with onboard signal processing circuitry. This vastly reduced the cost of using and making these devices and enabled their widespread practical use.

Hall effect sensors are most commonly used for proximity detection, position, speed, and current measurement. Nowadays, integrated Hall effect sensors are the preferred choice for a

number of reasons:

"**Small Size**: Integrated Hall effect sensors with on-board amplifiers can be obtained in surface-mount IC packages, taking up no more then a discrete transistor. Simple Hall effect transducers can be obtained in packages that are nearly microscopic. The small size of Hall effect sensors allows them to physically fit in many places where other magnetic transducers would be too bulky.

Ruggedness: Because most Hall effect sensors are fabricated as monolithic integrated circuits, they are highly immune to shock and vibration. In addition, standard IC packaging is highly resistant to moisture and environmental contaminants. Finally, monolithic Hall effect ICs can operate over the temperature range of -40^oC to $+150^oC$ are readily available from a number of sources. Hall effect ICs have been successfully used in hostile environments, such as inside automotive transmissions and down the bore-hole in oil-well drilling equipment.

Ease-of-use: While Hall effect transducers do not even come close to being the most sensitive or accurate means of measuring magnetic fields available, they are predictable and well-behaved. The output of a Hall effect transducer is nearly linear over a substantial range of magnetic fields and exhibits no significant hysteresis or memory effects. Hall effect sensors can measure a single vector component of a field, allowing one to sense direction of a field, as well as its magnitude.

Cost: While an instrumentation-grade Hall effect sensor can cost several hundred dollars, the vast majority of transducers currently produced in the world are sold for less than $0.20, including signal processing electronics. Hall effect sensors are among the most cost-effective magnetic field sensors available today." [15]

The above was a brief introduction about Hall effect transducers and their application in the industry. However, the advantages and applications of Hall effect transducers are not the purpose of this thesis. Readers who are interested in learning more about Hall transducers and their application in industry, are requested to go through [14–19], where these issues are discussed in more detail.

2.1.1 Our Project

The aim of our project was to develop an array comprising of 32 Hall sensors to detect sub-surface defects in the body of commercial aircrafts. This array was to be placed on a hand-held probe and connected to a Laptop for processing the data. This would have been a highly mobile system. The Laptop and the probe was designed so that it could easily be carried by a person to the specimen to be tested, instead of bringing the specimen to a lab for analysis. Portability is important for a field system since it is usually much easier to get the scanning system to the aircraft then removing the part of the aircraft and bringing it into the lab for observation.

Figure 2.1 shows the final configuration of the probe. A green circuit board carrying the Hall array and the coil was attached to the bottom of the probe as shown in Figure 2.2. The black epoxy covered area on the green circuit board is the location of the 32 Hall sensor array. A race-track coil is placed on the other side of the board so that the Hall array is as nearer to the test specimen as possible as shown in Figure 2.3

The first task was to select an appropriate Hall sensor for the project. The choices available included two Japanese sensors HW-105A and HW-104, made by Asahi Kasei Electronics Co. Japan [22], one device from Honeywell and the last device was being prepared for the project in the Microelectronics Research Center (MRC) at Iowa State university under the supervision of Dr. Gary Tuttle. In this thesis I will refer to the last of these as the MRC sensor. Later, during the project we got two other devices P2 and P15 that were made by Advanced Hall Sensor Ltd. Manchester, United Kingdom [23–24]. See section 2.1.8 for the detail on these sensors. After getting these samples, extensive tests were performed to make sure that they met the requirements. The device P-2 met our requirements and the final array was fabricated from P-2s.

The most important parameter of a Hall device is sensitivity, which means given the input current and applied magnetic field how much Hall voltage the sensor can generate. The more sensitive the device the better. Sensitivity is explained in detail in section 2.1.3(a). The Hall voltage V_H produced by a Hall sensor is given by

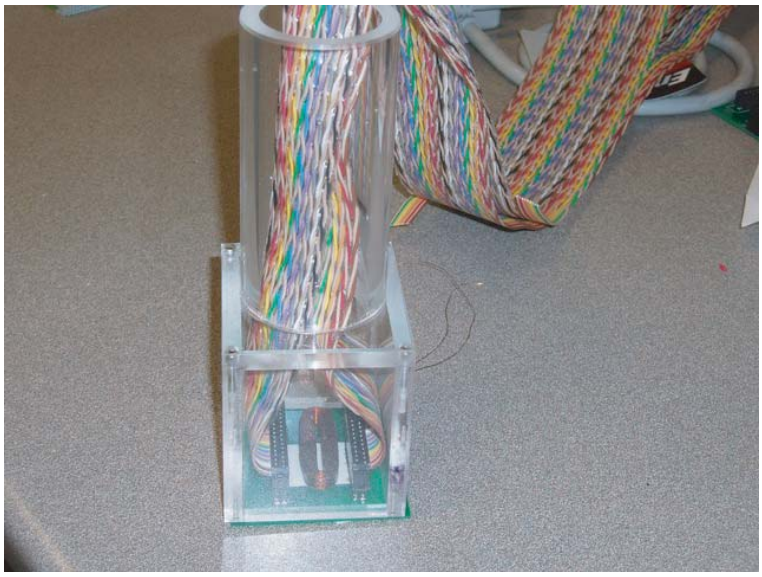

Figure 2.1 Final configuration of the Hall array probe

$$V_H = \frac{IB}{q_o N d} \tag{2.1}$$

where

I is the current is Amperes,

B is the magnetic flux density in Tesla,

q_o is the charge of an electron in Coulomb (C),

N is the carrier density. in carriers/m^3,

d is the thickness of the conductor in meters.

The measurements on the various parameters of the Hall sensors are explained in detail in section 2.1.3. The extensive testing done to the process of modulation is explained in detail in sections 2.1.4 and 2.1.5. First, we explain briefly the physics behind the Hall Effect.

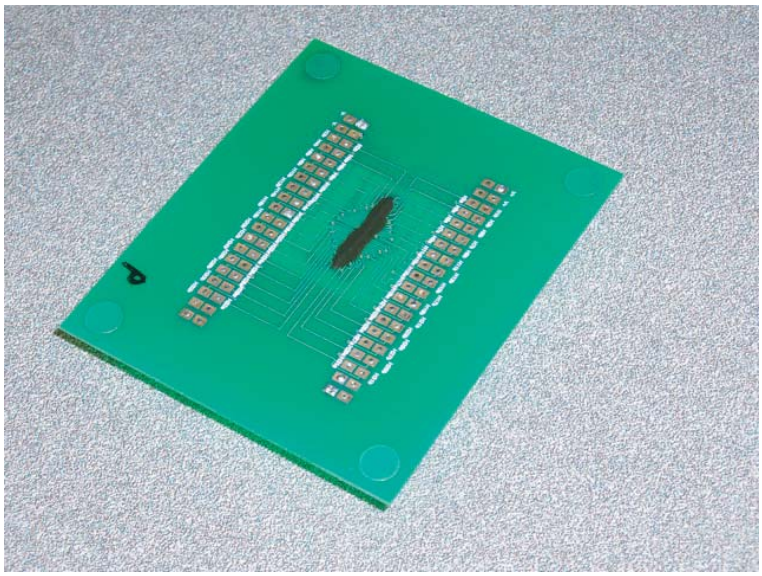

Figure 2.2 PCB showing the 32 element Hall array. This side would be resting on the specimen

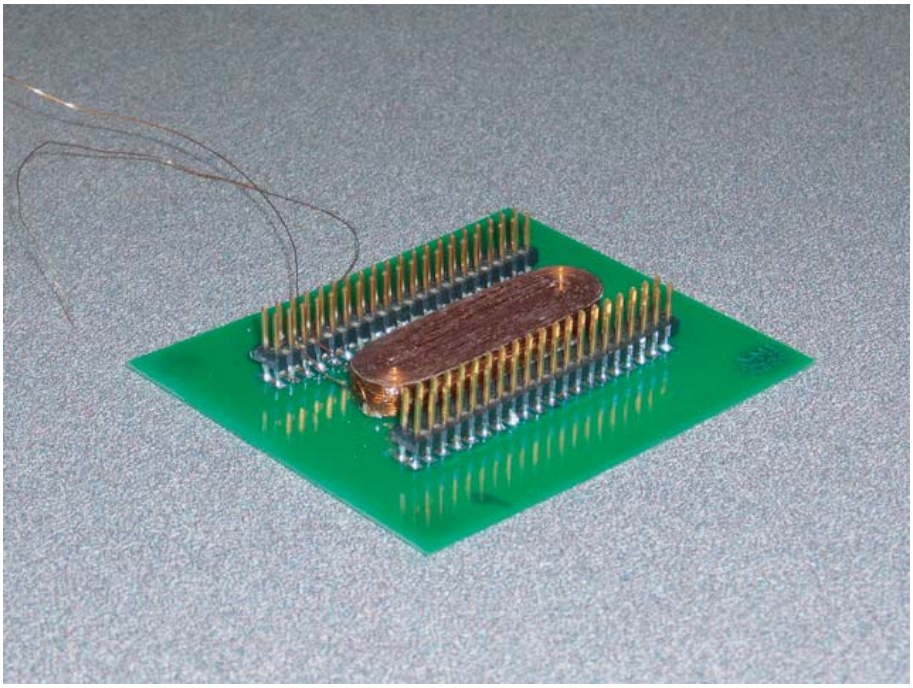

Figure 2.3 The inside surface of the PCB showing the racetrack coil and the contacts for the 32 element Hall array

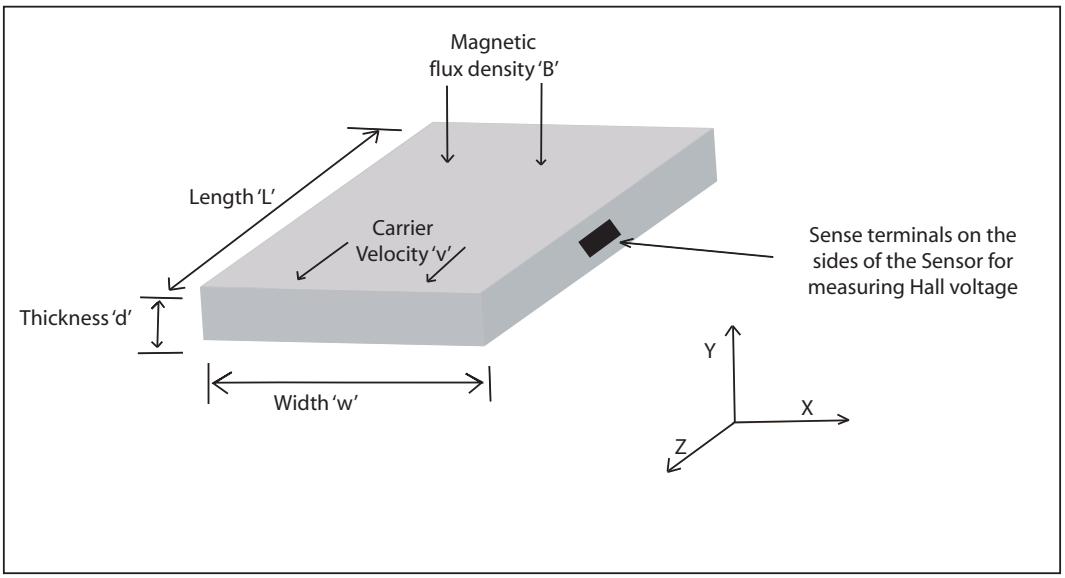

Figure 2.4 Hall Effect Transducer showing critical dimensions and axis

2.1.2 Hall Effect Physics

From electromagnetic theory we know that when a charge moves under the influence of an electric and magnetic field, a force is exerted on it. This force is given by

$$\overrightarrow{F} = q_o \overrightarrow{E} + q_o(\overrightarrow{v} \times \overrightarrow{B}) \tag{2.2}$$

where $\overrightarrow{F}$ is the resultant force, $\overrightarrow{E}$ is the Electric field, $\overrightarrow{B}$ is the magnetic flux density, q_o is the magnitude of the charge that is moving with a velocity $\overrightarrow{v}$. This relationship is known as the Lorentz force equation. In equation 2.2, except for q_o all other variables are vector quantities having independent x, y and z components.

This equation represents the response of two separate effects: the response of a charge to an electrical field and the response of a moving charge to a magnetic field. In case of an electrical field, a charge will experience a force in the direction of the field, proportional to both the magnitude of the charge and the strength of the field. This effect is what causes an electric current to flow in a conductor or a semi-conductor.

In case of a magnetic field, a charge particle does not experience any force unless it is moving. When it is moving, the force experienced by a charge particle is a function of the magnitude of its charge, the direction in which it is moving, and the orientation of the magnetic field it is moving through.

When a conductor, it may be a metal or a semi-conductor, is placed in a magnetic field and electric current is passed through it then the following will happen. The current will cause the charge carriers to move in the z direction with a velocity v, see Figure 2.4. The magnetic field will cause these charge carriers to move towards +x and -x direction. The concentration of charges towards the edges will cause a voltage to develop which will cause these charges to move back in the middle. The voltage is called the Hall voltage V_H and can be measured across the sides of the conductor. As equilibrium develops between the magnetic force pushing the charge carriers away and the electric force caused by the Hall voltage trying to push the charge carriers back in the middle, equation 2.2 becomes

$$0 = q_o\overrightarrow{E_H} + q_o(\overrightarrow{v} \times \overrightarrow{B}) \tag{2.3}$$

where $\overrightarrow{E_H}$ is the Hall electric field across the conductor. Solving for $\overrightarrow{E_H}$ yields

$$\overrightarrow{E_H} = -v \times \overrightarrow{B} \tag{2.4}$$

This implies that the Hall field is solely a function of the velocity of the charge carriers and the strength of the magnetic field. In order to get the Hall voltage V_H the Hall electric field is integrated over the width say "w" of the conductor giving us

$$V_H = -\mathrm{w}vB \tag{2.5}$$

The Hall Voltage is therefore a function of

1. The charge carrier velocity in the body of the conductor
2. The applied magnetic field
3. The spatial separation of the sense contacts, at right angles to the carrier motion

In conductors the velocity "v" is known as the drift velocity and is given by

$$v = \frac{I}{q_o N A} \tag{2.6}$$

where

I is the current is Amperes,

q_o is the charge of an electron in Coulomb (C),

N is the carrier density. in carriers/m,

A is the cross-section area in m^2.

Therefore the Hall effect voltage is given by

$$V_H = \frac{IB}{q_o N d} \tag{2.7}$$

where d is the thickness of the conductor in meters

2.1.3 Parameters of Hall Effect Sensors that were tested

In this section we explain some of the parameters of the Hall sensors that were tested to see if they full-filled our requirements. In order to get good performance from the Hall sensors, these parameters should be taken into account. These parameters are device dependant and sometimes between two devices of the same type.

a) Sensitivity:

First and the most important parameter of a Hall Sensor is its sensitivity. It can also be called the gain of the Hall sensor. Usually, more sensitivity is a good thing, as more sensitive the device, the more the signal to work with. A sensor that provides more output signal will require simpler and less expensive support electronics than the one with smaller output signal. As previously mentioned the sensitivity of the Hall device depends on the bias current so in order to compare two device sensitivities we need to take the bias current out of the equation.

This is done by dividing the output voltage by the bias current. Therefore, the sensitivity is usually defined in the units of volts per unit field, per unit bias current or simply Volts per Amp.Tesla (V/AT). From Equation 2.7, the sensitivity of a Hall sensor is

$$\text{Sensitivity} = \frac{V_H}{IB} = \frac{1}{q_o N d} \tag{2.8}$$

To measure sensitivity, the Hall device was biased by a DC current and was put in a varying magnetic field generated by passing AC current through a solenoidal coil. A sensing resistor was used in series with the Hall device to determine the exact current going through the Hall device. A resister was also used in series with the coil to determine the exact current going through the coil. The block diagram of the setup is displayed in Figure 2.5. The outputs of the Hall device were then connected to a Lock-in amplifier. The difference between the two Hall device outputs were measured and then the result was displayed in terms of x and y components. Since the coil behaves as an inductive load, the reference signal going to the lock-in amplifier was taken after the coil, instead of the source, to take into account any phase change that might have resulted after the signal passed through the coil.

P-2 Hall Sensor:

Figure 2.6 shows the sensitivity of the P-2 device as function of frequency. Ideally the x-component should be a flat line while the y-component should be increasing linearly with frequency. As displayed in figure 2.6, this is exactly the case with the P-2 sensor. If you look at the magnitude it is increasing linearly with frequency. This is not because the Hall Voltage is increasing with the frequency but it is due to the pick-up in the leads that causes the magnitude to increase linearly with frequency. The pick-up in the leads is given by equation (2.13) and is explained in detail in section 2.1.3(e). Splitting the magnitude into x and y component gives a more realistic picture. The Hall voltage that is a real part displayed by the x-component remains constant with the increase in frequency. The pick-up in the leads which is an imaginary part displayed by the y-component increases linearly with frequency. The

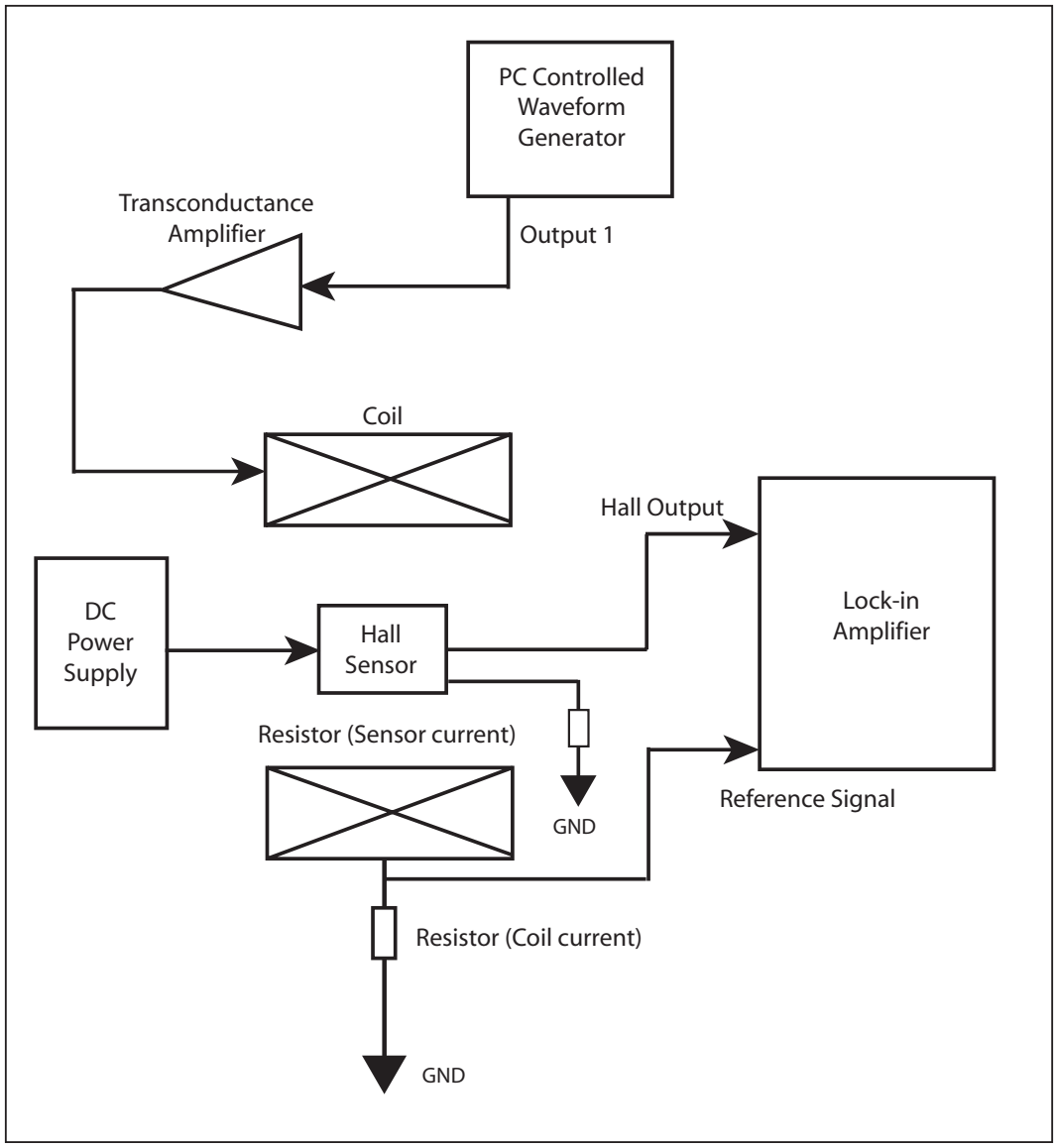

Figure 2.5 Schematic diagram of the system used to measure the sensitivity of a Hall device as a function of frequency

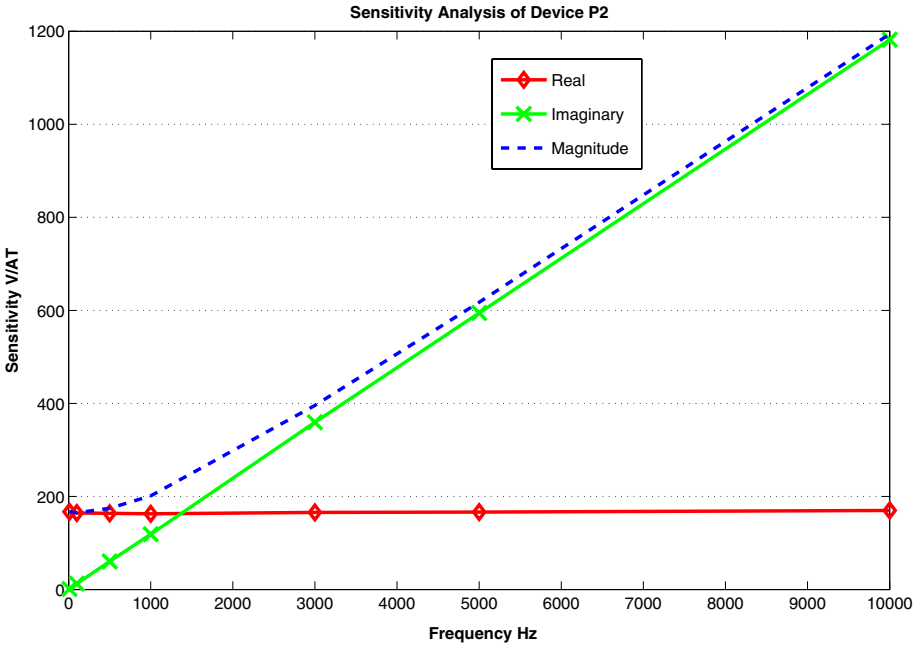

Figure 2.6 Sensitivity of the P-2 Hall sensor as a function of frequency

pick-up in the leads becomes a big problem at high frequencies and it is desirable to remove it from the signal. In section 2.1.5, a way to remove it using modulation is explained.

P-15 Hall Sensor:

Figure 2.7 shows the sensitivity of the P-15 Hall sensor as a function of frequency. Notice the imaginary part increases linearly with frequency indicating the presence of pick-up in the leads.

HW-105 Hall Sensor:

Figure 2.8 shows the sensitivity of the Japanese HW-105 Hall sensor as a function of frequency. Notice the imaginary part increases linearly with frequency indicating the presence of pick-up in the leads.

MRC Hall Sensor:

The MRC sensor did not give us the required results. Figure 2.9 shows the sensitivity of

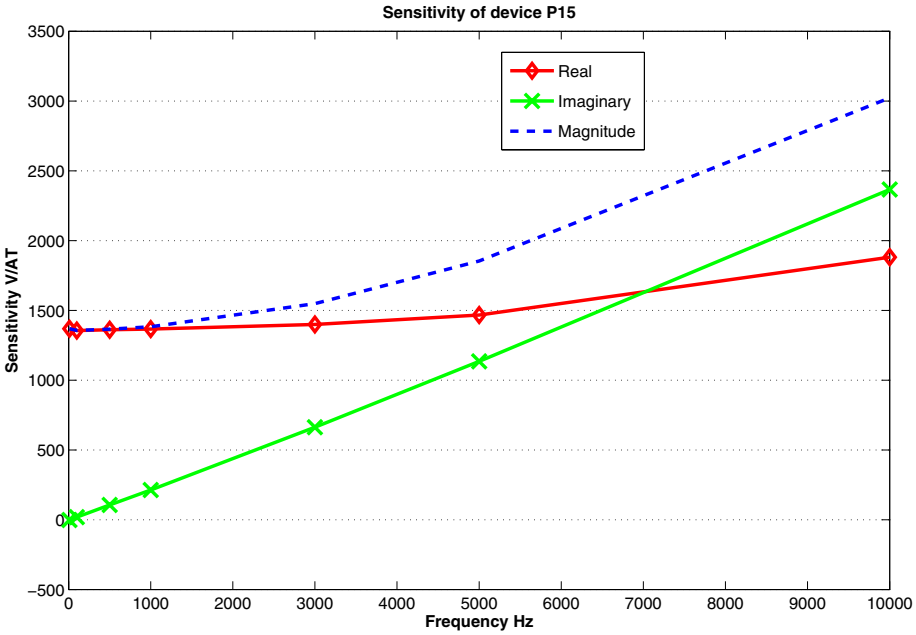

Figure 2.7 Sensitivity of the P-15 Hall sensor as a function of frequency

the Sensor; displaying the magnitude, real component and the imaginary component of the sensitivity normalized to the current (V/AT). The imaginary component increases linearly with frequency which is to be expected as the imaginary component includes the induced EMF in the leads of the sensor which increases linearly with frequency. The real component that includes the Hall Voltage appears to be negligible as compared to the induced voltage. Thus, the magnitude of the Hall Voltage is mainly due to the induced EMF. This is not at all desirable. After looking at the experimental setup closely to make sure the erroneous reading was not due to the result of incorrectly hooked up apparatus, the sensitivity analysis of the MRC sensor was repeated many times. The data obtained showed the MRC sensor not performing as desired. The MRC sensor was thus rejected.

The sensitivity of a Hall device depends on the temperature and it varies slightly with it. Although the variation is small over a small change in temperature but it must be accounted for if the temperature variations are vary large or when a high degree of measurement stability

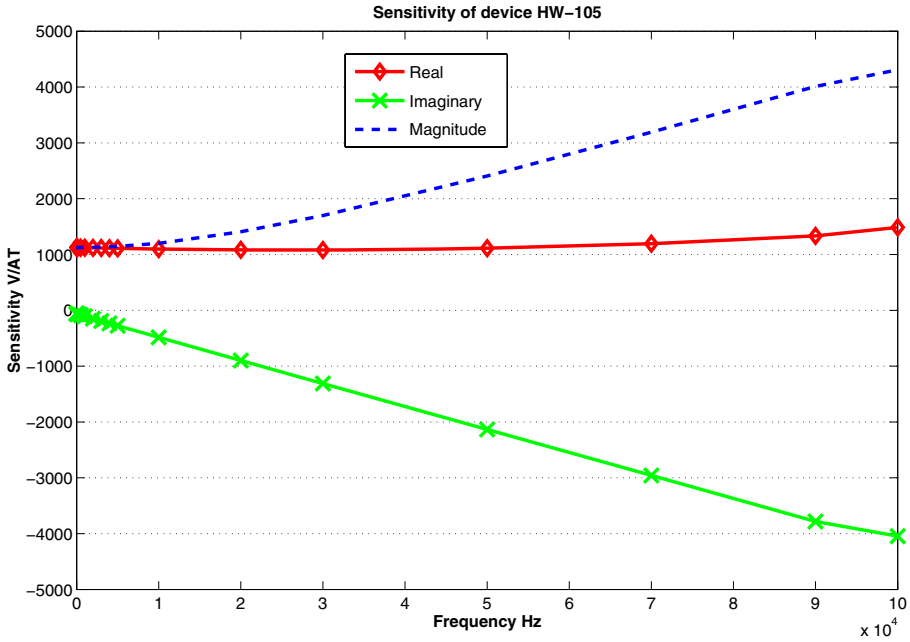

Figure 2.8 Sensitivity of the HW-105 Hall sensor as a function of frequency

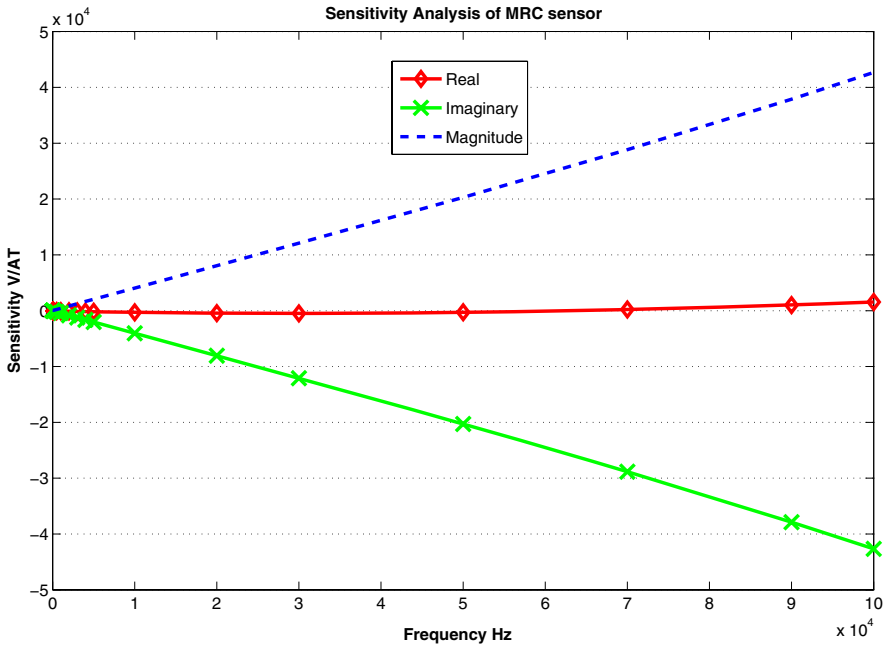

Figure 2.9 Sensitivity of the MRC Hall sensor as a function of frequency

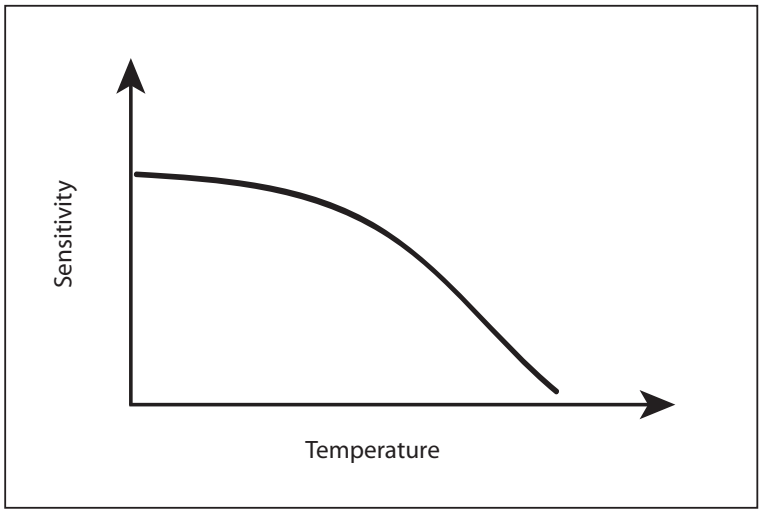

Figure 2.10 Diagram to give a general idea of the relationship between temperature and sensitivity. For more detail, a Fig based on experimental data and typical results for sensitivity vs temperature; see [16][17]

is needed. For example, a Hall device will have a different sensitivity when the circuit is just switched on. But if the current flows through the hall device for a very long time, it will heat up slightly and the result will be a slight decrease in the sensitivity. Figure 2.10 shows the variation in the sensitivity vs temperature of a Hall effect transducer when biased with a constant current. This figure is conceptual and does not represent experimental data. Readers interested in further detail, typical results showing the change in sensitivity vs temperature and a Fig based on experimental data; see [16][17].

b) Ohmic Offset:

Ohmic offset results due to imperfection in the manufacturing of the Hall device. Like electrical noise this offset is impossible to get rid of. All one can do is to minimize it. Ohmic offset is defined as the the small voltage that appears at the output of the Hall device when it is biased in the absence of a magnetic field. This offset voltage is undesirable as it limits the ability of the device to detect small steady state magnetic fields. It complicates the matter if the device has a low sensitivity as in that case this ohmic offset becomes quite significant.

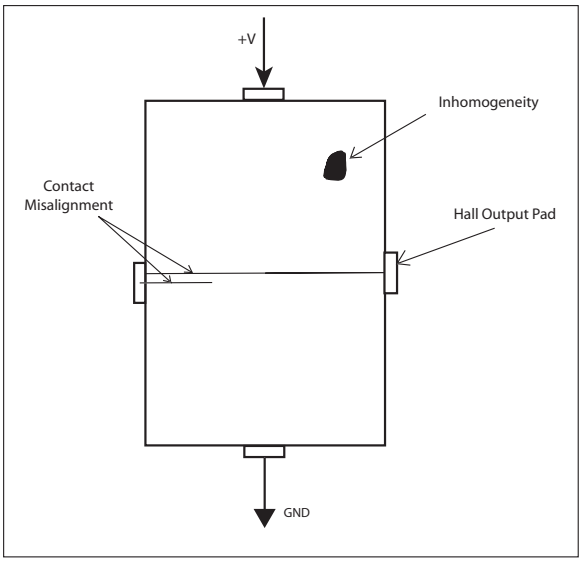

Figure 2.11 Ohmic offsets results from misalignment of the sense contacts and inhomogeneities in the material

A number of factors contribute to create this ohmic offset. One is the alignment error in the sense contacts, where one is slightly upstream or downstream from the other as shown in Figure 2.11. Inhomogeneities in the material of the device are another source of errors and finally the effect of the change in the electrical resistance of the device due to mechanical distortion.

The ohmic offset was tested by using the same setup as explained in Figure 2.5. The only difference was that the magnetic field was not applied and the device was kept inside an aluminum box to shield it from any stray magnetic fields. The ohmic offset value obtained this way for both HW-105 and P-2 was almost negligible as compared to Hall voltage produced by the two devices. One way to remove this ohmic offset from the output Hall voltage is to use the process of modulation explained in detail later in section 2.1.5.

c) Input and Output Resistance:

These parameters are important to the circuit designer as they influence the design of the bias circuitry and the front end amplifier design used to detect the Hall voltage. In an array of Hall sensors the input and output resistances become important as 16 Hall sensors in series

with 800 ohm input resistance mean that a total resistance is 12.8 kΩ. Thus the input voltage needs to be high in order to supply 1 mA current to each device. Similarly the same number of sensors in parallel mean a total resistance of 50 Ω. Thus in order to supply the 1 mA current to each device a much lower bias voltage is needed.

For low-noise operation a low output resistance device is desirable

d) Electrical Noise:

There are basically two types of noise that the Hall effect transducer present at their outputs. First kind is the **"Johnson noise"**. Johnson noise is given by

$$V_{noise} = \sqrt{4kTRB} \tag{2.9}$$

where

k is Boltzmann's constant ($1.38 \times 10^{-23} K^{-1}$)

T is the Temperature in Kelvin (K)

R is the output resistance in Ohms

B is the bandwidth in Hertz

Johnson noise is a result of the thermally induced motion of the electrons or any charge carriers in a conductive material. Thus, this noise is a function of the output resistance of the device and the operating temperature. It is generated by every resistive material and it defines the bottom limit to the signal that can be recovered from the Hall sensor. It can be reduced by minimizing the impedance of the Hall transducer. In our project the P-2 device has a low 800 Ω resistance and Johnson noise is negligible as compared to the sensitivity of the device.

The other noise is the **"flicker noise"** or the "1/f" noise. It is often a more significant problem than the Johnson noise. This type of noise is found in many physical systems and can be generated by many different and unrelated types of mechanisms. The common factor, however is the resultant spectrum. It is maximum near DC and decreases as the frequency increases. That is why it is referred to as the 1/f noise. In our project we use modulation to

reduce the effect of this type of noise as in modulation the Hall signals are shifted to a very high frequency and this noise is than filtered off.

e) Pick-up in the leads:

Another important factor is the induced voltage in the leads of the Hall sensor or simply the pick-up in the leads of the Hall device. This can also be considered as noise, since it is an undesirable signal. Faraday's law states that if a loop of wire is paced in a magnetic field, there is a voltage induced in the loop proportional to the rate of change of the magnetic flux in the coil.

$$V_{ind} = -N\frac{d\Phi}{dt} \tag{2.10}$$

where

N is the number of turns in the loop,

Φ is the magnetic flux in Weber

"-" sign shows the direction of the induced voltage which is opposite to the directed voltage and is given by Lenz's Law.

The magnetic flux Φ produced by a AC magnetic field B is given by

$$\Phi = BA\cos(\omega t)\cos\theta \tag{2.11}$$

where

B is the magnetic field in Tesla,

ω is the frequency of B in radians

A is the area of the loop in square meters,

θ is the angle between B and A

Assuming B is perpendicular to A i.e $\theta = 0^\circ$ and the number of turns in the loop N = 1, then substituting the value of Φ in equation 2.10 gives the induced voltage as

$$V_{ind} = -\frac{dBA\cos(\omega t)}{dt} \tag{2.12}$$

Or

$$V_{ind} = \omega BA\sin(\omega t) \tag{2.13}$$

This voltage is known as induced voltage is one of the biggest sources of errors in the Hall device. As can be seen from equation 2.13 it increases linearly with frequency and becomes a problem at higher frequencies.

2.1.4 Principle of Modulation

The best way to get rid of the Ohmic offset and pick-up in the leads is to use the principle of modulation. Simply explained, the process of modulation is that the desired signal is shifted to a higher frequency, the undesired signals are then filtered off and then the desired signal is shifted back to its original frequency.

In our case the desired signal is the Hall voltage. Everything else is an unwanted signal. The mathematical representation of the process of modulation is explained below.

$$\cos(\omega_1 t)\cos(\omega_2 t) = \frac{1}{2}[\cos(\omega_1+\omega_2)t + \cos(\omega_1-\omega_2)t] \tag{2.14}$$

Equation 2.14 states that when two sinusoids are multiplied, the resultant signal has two sets of frequencies i.e. the sum and the difference of the frequencies of the sinusoids.

2.1.5 Modulation in Hall Effect Sensors

The block diagram of the setup used to explain the process of modulation is shown in Figure 2.13. To achieve modulation, the Hall sensor is biased by an AC current instead of a DC current. The Hall sensor acts as a multiplier as the Hall Voltage, given by equation 2.1 is just the multiplication of the Hall input current and the magnetic field. The term $1/q_oNd$ is a constant. To simplify the matter equation 2.1 is rewritten as

$$V_H = KIB \tag{2.15}$$

where

K = $\frac{1}{q_o Nd}$ = constant

Instead of a DC current the Hall sensor is now biased with an AC current at a frequency of ω_1, which varies sinusoidally with time as

$$I = I_0 \cos(\omega_1 t) \tag{2.16}$$

The coil producing the magnetic field is biased by an AC current having a frequency of ω_2.

$$B = B_0 \cos(\omega_2 t) \tag{2.17}$$

Substituting I and B in equation 2.15, the Hall voltage then becomes

$$V_H = KI_0 \cos(\omega_1 t) B_0 \cos(\omega_2 t) \tag{2.18}$$

Using the identity from equation. 2.14, the Hall voltage becomes

$$V_H = \frac{1}{2} KI_0 B_0 [\cos(\omega_1 + \omega_2)t + \cos(\omega_1 - \omega_2)t] \tag{2.19}$$

The Hall voltage has been shifted from baseband to a higher frequency of $(\omega_1 + \omega_2)$ and $(\omega_1 - \omega_2)$. But the voltage on the terminals of the Hall device also contains the induced voltage V_{ind} from equation 2.13.

$$V_T = V_H + V_{ind} \tag{2.20}$$

Substituting the values of V_{ind} and V_H from equations 2.13 and 2.19 respectively gives

$$V_T = \frac{1}{2} K I_0 B_0 [\cos(\omega_1 + \omega_2)t + \cos(\omega_1 - \omega_2)t] + \omega_2 B A \sin(\omega_2 t) \tag{2.21}$$

The induced voltage is at a frequency of ω_2 and can easily be filtered off using a high-pass filter. The signal left is the desired Hall voltage which can now be demodulated back to DC or read using the Lock-in amplifier.

During the course of the project, the principle of modulation was tested successfully many times using the Japanese HW-105 sensor, as well as the British P-2 sensor. Fig 2.12 shows the output of a Hall sensor with and without modulation, under ideal circumstances. This figure is not based on experimental data but is illustrated to convey the process of modulation. Without modulation the frequency response of the sensitivity of Hall device should look something like Fig 2.12(A). The magnitude (blue curve) of the sensitivity will increase with frequency. This is to be expected as the magnitude also includes the undesirable induced voltage, in addition to the desirable Hall voltage. When the Magnitude of the sensitivity is split into its real and imaginary parts, one would expect the real part (red curve) which is primarily composed of the Hall signal to be a almost horizontal line over the entire range of frequency. Though in reality you will find that the real part does not remain a horizontal line but is in fact a slightly curved line going up as the frequency increases. But here we are assuming an ideal situation. The imaginary part (green curve) should increase linearly with frequency as it is primarily composed of the induced voltage and we know from equation 2.13 that the induced voltage increases linearly with frequency. This is how the curves would look like without modulation.

After modulation and removing the induced voltage from the signal, the sensitivity of the Hall device would look something like Figure 2.12(B). The real part would remain unaffected. The only change would be in the imaginary part, which now should be a horizontal line. The magnitude would reflect that and would be a horizontal line too. The error introduced due to the induced voltage is now removed. Notice in Fig 2.12(B) the curves do not start from zero. This due to the fact that under ideal circumstances the the frequency transform of a sinusoid is a straight line but in the real world it would have a bandwidth of at least around

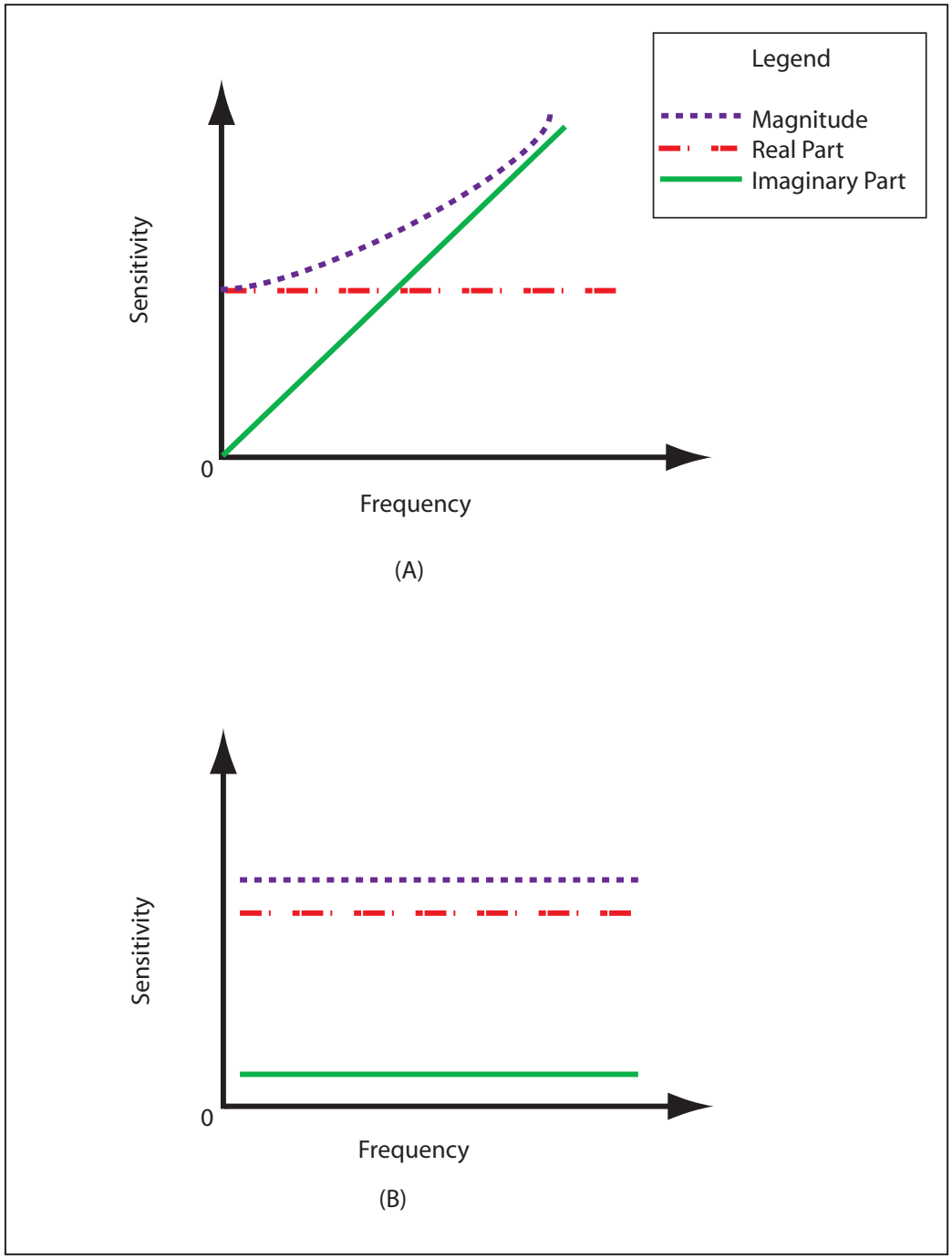

Figure 2.12 Figure Explaining the concept of modulation

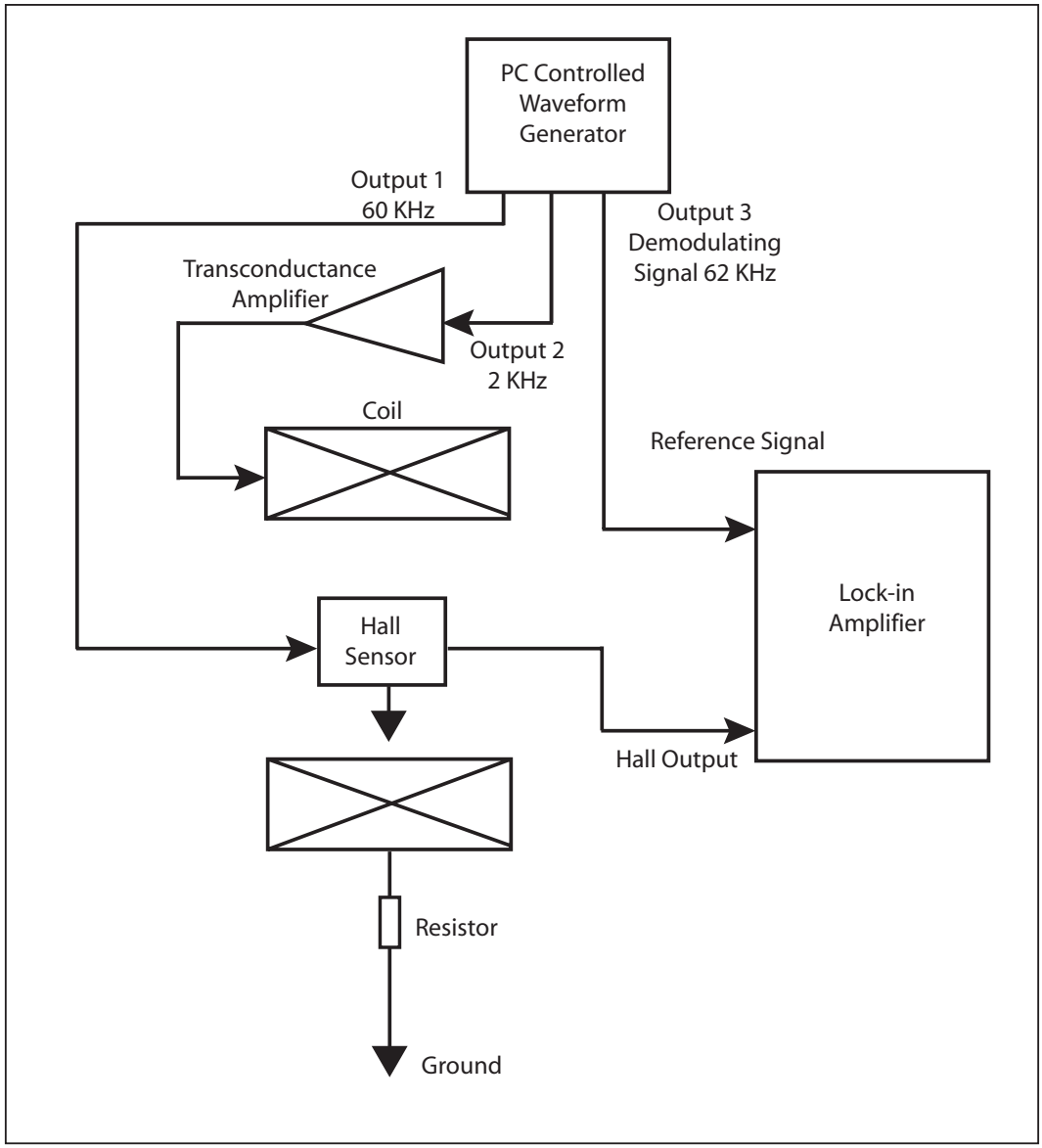

Figure 2.13 Block diagram of the circuit layout during the process of modulation

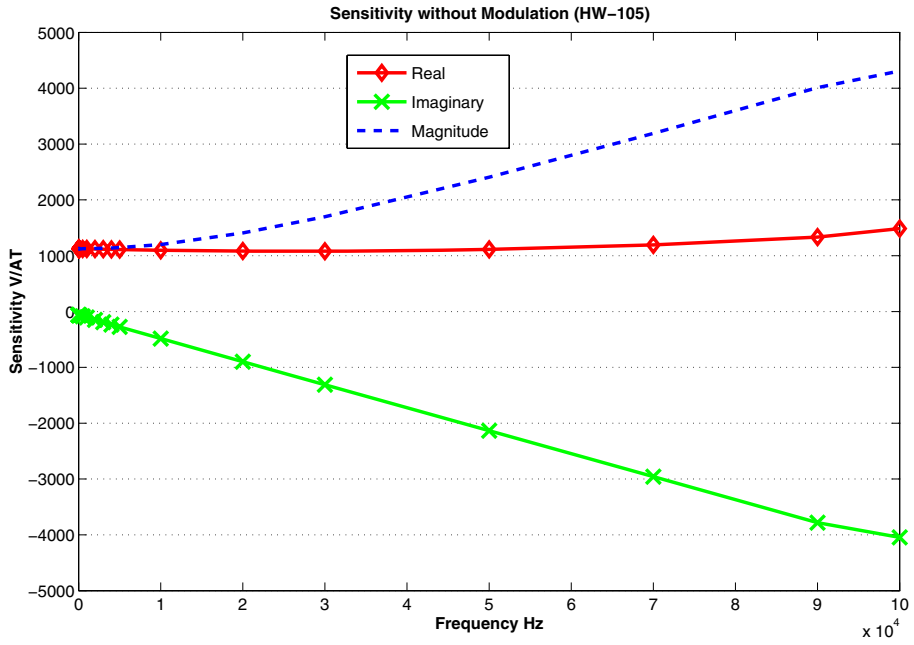

Figure 2.14 Sensitivity without Modulation

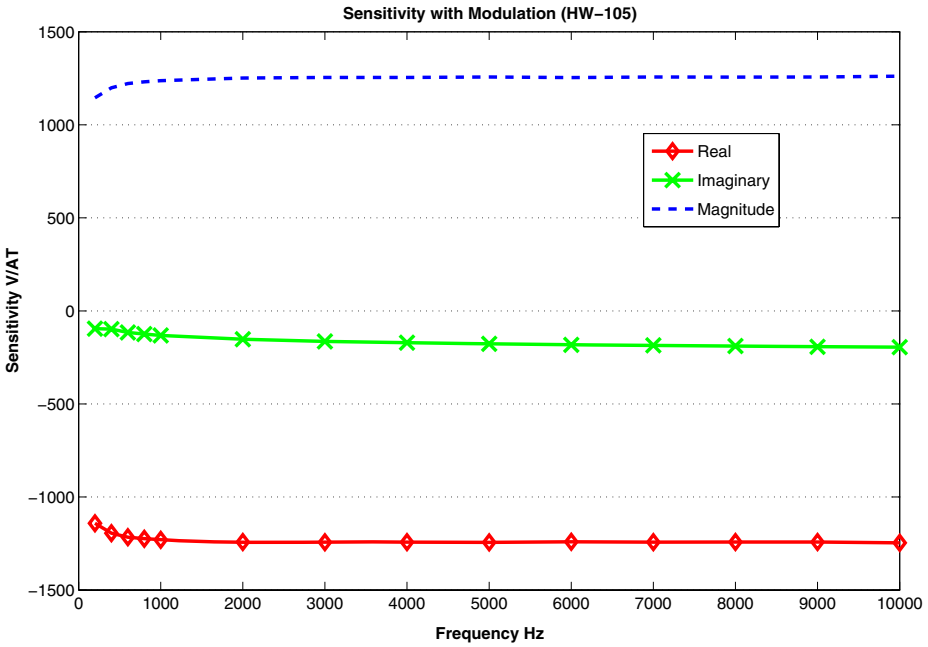

Figure 2.15 Sensitivity with modulation

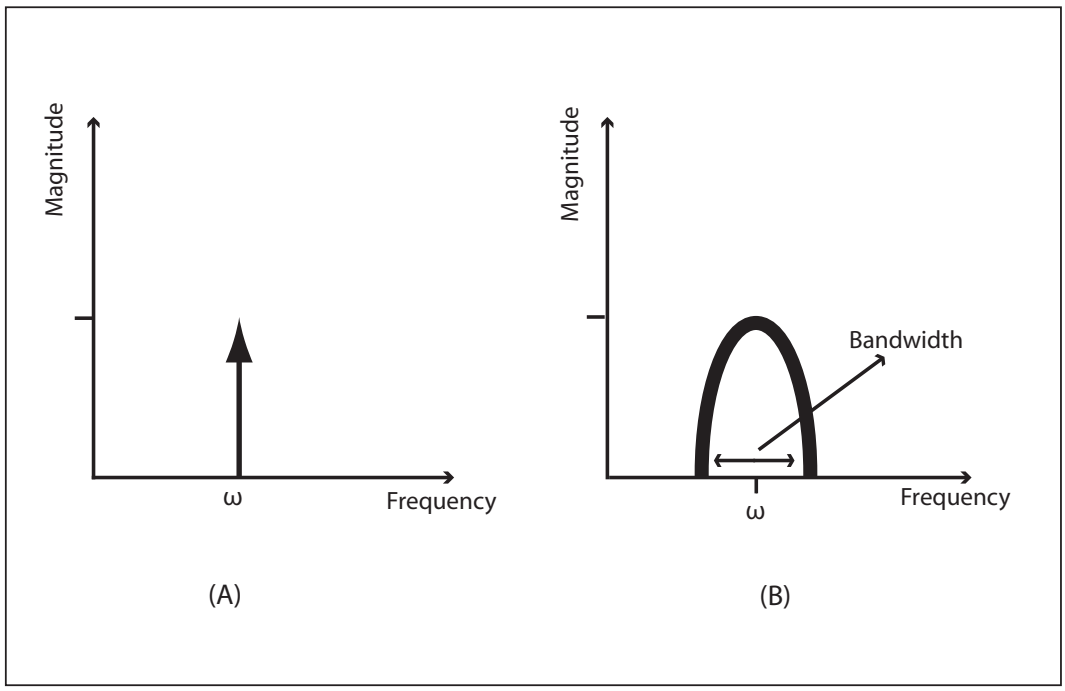

Figure 2.16 Comparison between the frequency spectrum of an ideal sinusoid and a real world sinusoid

200 Hz, (100 Hz each side). Fig 2.16 shows the comparison. Fig 2.16(A) displays the frequency transform of an ideal sinusoid, while Fig 2.16(B) shows the frequency transform of a sinusoid in the real world. Similarly the undesired signal present around DC will also have a spectrum with a bandwidth of around 200 Hz and in order to get rid of this signal a high pass filter with a cutoff of at least 200 Hz should be used prior to demodulation.

Figure 2.17 shows how the process would look like in the frequency domain. Fig 2.17(A) and 2.17(B) show the frequency domain representation of equations 2.16, the Hall device bias current and equation 2.17, the coil current respectively. Fig 2.17(B) also has the induced voltage present at frequency ω_2. Figure 2.17(C) shows the Hall output V_T from equation 2.21. Notice that after modulation the desired Hall signal has shifted to a higher frequency while the Induced voltage is still at ω_2. The induced voltage can now be easily filtered off. Filtration will also get rid of any other noise or undesired signal present in the V_T. The signal remaining would be the Hall voltage V_H. V_H can then be de-modulated and filtered off.

In project various frequencies were used for testing the process of modulation. Initially the testing was done using the carrier frequency (Hall sensor current) of 30 kHz and the modulating frequency (the coil current) of 1 kHz. Ideally the carrier frequency should be as high as possible but we were constrained due to the bandwidth of the AC source used to bias the circuit whose bandwidth was only 35 kHz. The process of modulation worked as expected. See Fig 2.14 and Fig 2.15. In this case the sensor was the HW-105. The coil current was selected to be 1 kHz due to the fact that the frequencies needed for nondestructive analysis of commercial airplanes are typically between 1-3 kHz. This frequency range is enough to satisfy a skin depth of most commercial aircrafts. Figure 2.15 shows that during modulation, the Coil current was increased with an increment of 1 kHz up till 10 kHz. It was unadvisable to go beyond 10 kHz as with the Carrier frequency at 30 kHz the lower sideband would have formed at 30 - 10 = 20 kHz. The 10 kHz deadline was chosen to avoid interference and to be on the safe side. As seen in the figure the Real, imaginary and magnitude curves remain almost horizontal from 1 to 10 kHz. This was expected and showed that the process of modulation worked flawlessly.

Our final circuit was biased using computer controlled waveform generator PCI cards so the constraint of limiting the carrier frequency below 35 kHz was not there. Thus the Hall sensor was biased by a current of 60 kHz while the coil was biased by a current of 2 kHz. In order to demodulate the signals, a third signal of 62 kHz was generated from the same cards. The de-modulation brought the Hall voltage present at 62 kHz back to baseband (DC) and Hall voltage was then filtered off using a low pass filter. It is important to point out that the PC cards were connected together so they were being run by the same clock. This resulted in all the three signals to have the same phase. This is important if a lock-in amplifier is to be used to de-modulate the final signal.

2.1.6 Detector circuitry

The signals from the Hall sensors are then fed to a detector circuit. The circuit was designed by Haiyan Sun [26]. Each hall sensor has its own detector circuit and since our hall array has 32 hall sensors so there are 32 detector circuits on 8 PCB boards. Each PCB board handles

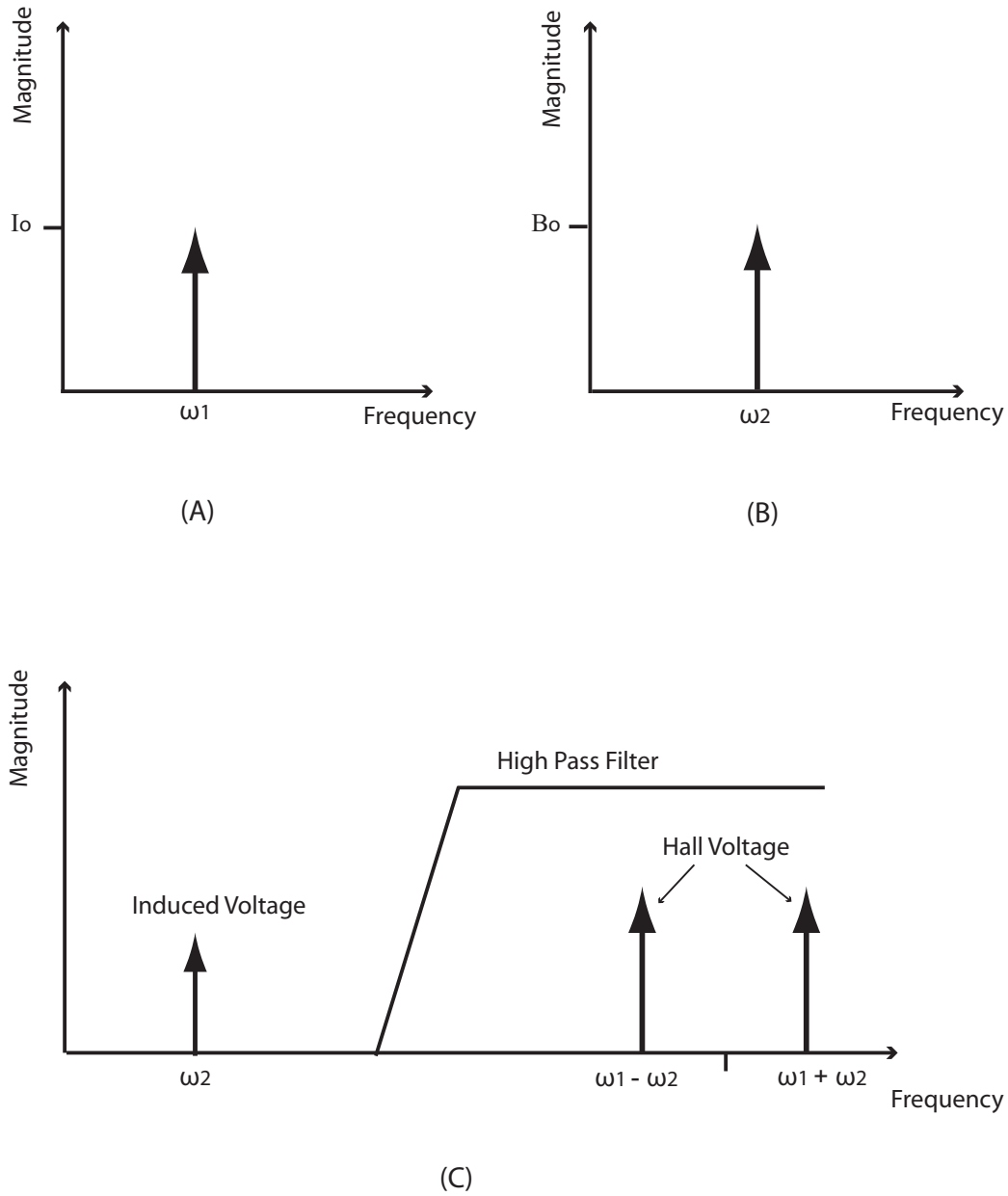

Figure 2.17 Process of Modulation in frequency domain

4 Hall sensors. The circuit schematic of the detector circuit and that of the PCB showing 4 detector circuits is shown in Fig 2.20 and Fig 2.19 respectively. The detector circuit comprise of an amplifier stage, a multiplier stage, a low-pass filter and a sample-and-hold circuit, see Figure 2.18.

The amplifier stage has two amplifiers AD620, one has a gain of 500 while the other has a gain of unity. The second stage was built in the circuit to provide additional gain if it was needed. At the time of circuit design it was thought that a gain of 500 would be enough. upon testing a prototype of the circuit it was felt that this gain would not be enough furthermore according to the data sheet of AD620 with a gain of 500 the bandwidth of the amplifier is only around 16 kHz. This bandwidth is not enough if the circuit is to be used for modulation. For modulation it is desirable to use a high frequency 20 - 100 kHz to reduce the background noise and increase the signal to noise ratio.

The circuit board was thus modified to make the gain of the first stage low enough so that the bandwidth would increase to about 100 kHz. That gain was calculated by various trials and finally a gain of around 80 was decided. This decreased the overall gain of the circuit so the second amplifier was also given the same gain. The overall gain of the amplifier stage was now 6400. Another reason to give both amplifiers the same gain was to increase the stability of the circuit.

The signal from the amplifier stage is then fed to the input X of a multiplier AD633. The multiplier is actually a demodulator, as it shifts the frequency of the Hall signal back to DC. The output of the multiplier is given by

$$\text{Output} = \frac{XY}{10} + Z \tag{2.22}$$

The multiplier has two more inputs Y and Z. Input Z is produced by the sample-and-hold circuit. Input Y is multiplied with input X and causes it to move to DC. For Example, if the Hall sensor is biased with a DC current and the coil is biased with an AC current at a frequency of 2 kHz, then the Hall signal X will also be at a frequency of 2 kHz. Now, when

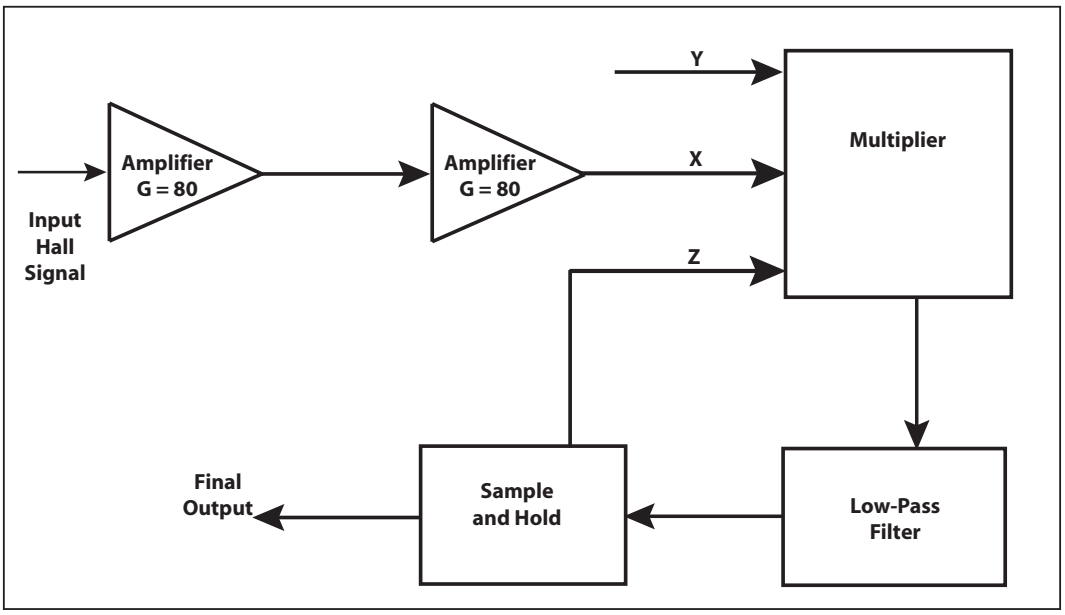

Figure 2.18 Block Diagram of the detector circuit

signal Y with the frequency of 2 kHz is multiplied with X, it produces one signal at a frequency of 4 kHz and another at DC. The high frequency is then filtered off. Care should be taken to insure that both the signals X and Y not only have the same frequency but also the same phase, so that no information is lost by the change in the phase of the signals. This is achieved by generating both signals by a computer controlled waveform generator card having the same onboard clock. The output of the multiplier is then passed through a low-pass filter with a cut-off at 50 Hz and the signal at DC is then filtered off.

This DC signal is the Hall voltage and is then fed to a sample and hold circuit, which holds the signal long enough to be read on a laptop running a Labview program.

2.1.7 The Hall Array

The Hall array used in our experiment comprised of 32 P-2 type Hall Sensors. The array was part of a whole wafer comprising about 5000 plus Hall sensors. The actual wafer is illustrated in Fig 2.23. On the wafer or die the arrays were divided into three different configurations

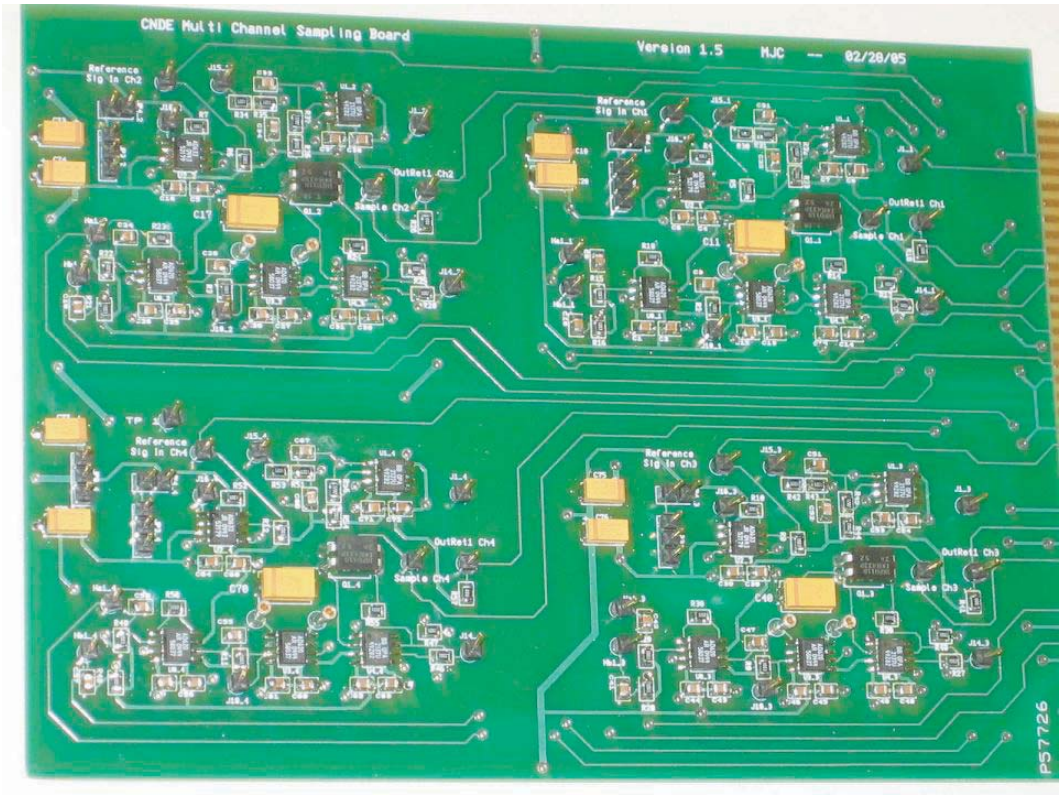

Figure 2.19 PCB showing four detector circuits. Each circuit handles one Hall Sensor. There are 32 circuits in total on 8 PCBs

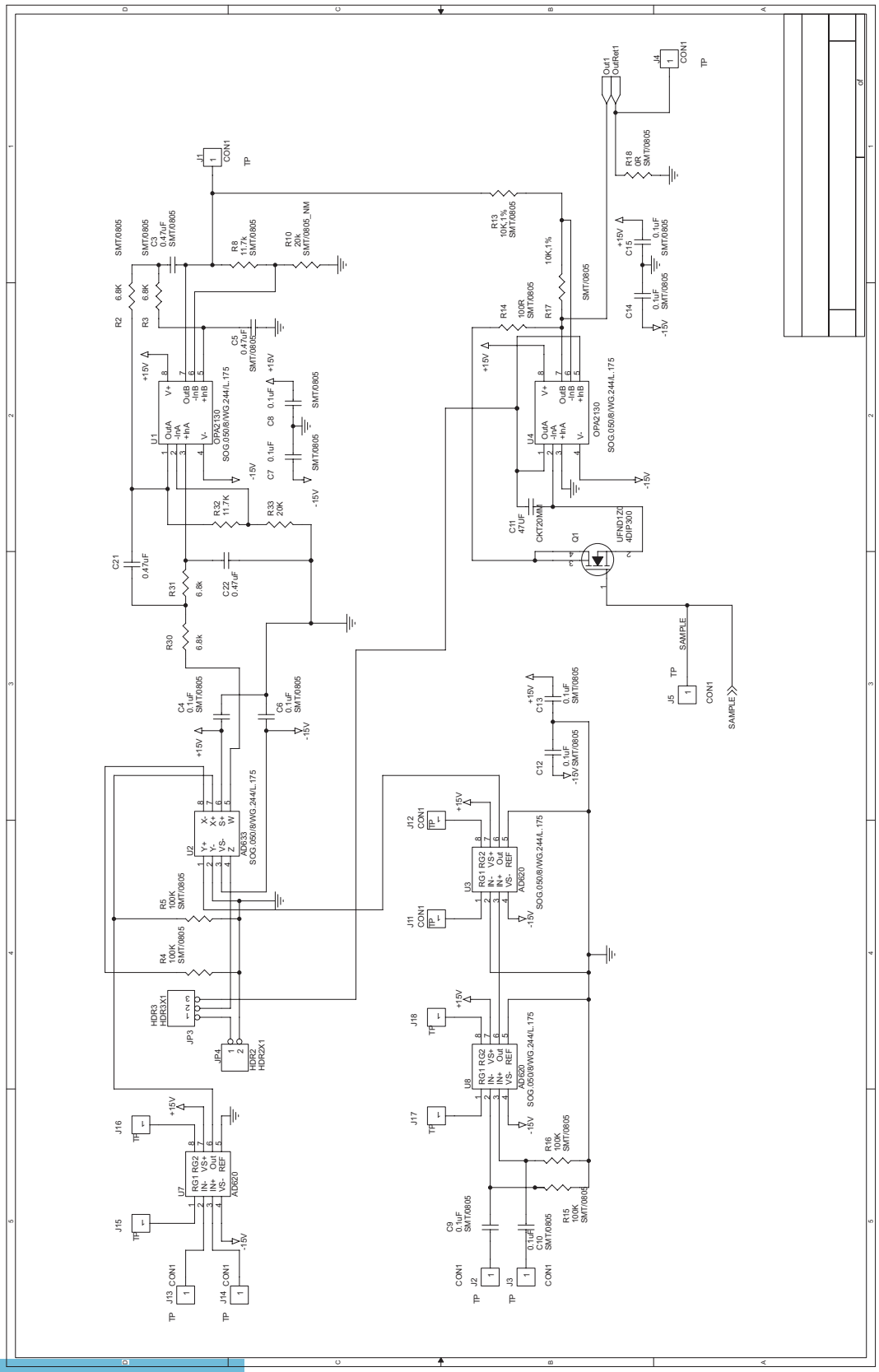

Figure 2.20 Schematic of the detector circuit

depending on how the array was to be powered. The configurations were parallel, series and individual Hall sensors. The parallel and series configuration are shown in Figures 2.21 and 2.22 respectively. Figure 2.24 is a blow up of the actual wafer from Fig 2.23, showing the parallel and series and individual sensors as they are positioned on the actual die.

Both parallel and series configurations have their advantages and disadvantages. For example the total resistance across a 16 element die for the parallel configuration is only 45 ohms (700 ohms across each device). Thus the voltage needed to power the array and dive a current of 1 mA through each sensor would be very small. On the other hand the 16 element array connected in series will have a combined resistance of approximately 10 k ohms. A large amount of voltage is needed to drive 1 mA current through each device.

Figure 2.25 shows the various configuration of the Hall array with respect to the race-track coil that was to be used to apply magnetic field to the material under observation. Each configuration has its merits and drawbacks. In the end, we decided to go with the configuration (A), as it provided a reasonable amount of performance while saving a lot of space. This way the hand held probe would not be a big cumbersome thing.

Figure 2.26 shows the blow up of the individual Hall sensor, showing the sense contacts and the width and length of the sensor. These parameters effect the sensitivity of the Hall Sensor and should be taken care off while the Hall sensor was fabricated

2.1.8 The P-2 Hall Sensor

The Hall devices are usually made from semiconductor materials such as GaAs, InAs, InSb, AlGaAs, InGaAs etc. The InGaAs/AlGaAs/GaAs are popular nowadays because they offer advantages such as superior electron mobility, moderate sheet carrier densities, low temperature dependence of the output Hall voltage and large signal to noise ratios [23]. These features allow the devices to be small but sensitive. Nowadays, devices made out of complex materials AlGaAs-InGaAs have grown popular and have become the choice for high speed devices and RF circuits [23]. The P-2 Hall sensors used in our project is made out of similar complex material AlGaAs-InGaAs-GaAs. There performance has been tested by [23] and these devices were

found to be satisfactory even for low magnetic fields with few exceptions [23]. These sensors proved to be sufficient for our project requirement and were thus selected. The P-2 Hall sensor powered with an AC circuit was able to detect magnetic fields as low as 100nT, which are among the lowest ever reported using a GaAs Hall effect sensor with low cost signalling conditioning circuitry [23].

2.1.9 Labview Software

A software was written in Labview to acquire the data from the Hall array. The 32 element Hall array was divided into two individually powered 16 element arrays. Each 16 element array was connected to a PCMCIA card. The Labview software scanned the data from both PCMCIA cards and then coupled it together to display all 32 sensor data on one graph. There were two types of graphs. One, a 2D graph that displayed the location of the crack by change of amplitude. When the 32 element array was passed over a crack the amplitude of the Hall sensors directly over the crack would change giving the location of the crack. The second graph was a 3D intensity chart. When the array passed over a crack, the color on the chart would change showing the location of the crack. Each graph displayed real-time data and was set in a continuous loop. The software would only stop acquiring the data, when the off switch was pressed, either on the software panel or on the Hall array probe.

2.1.10 Conclusion

The project was tested using a single Hall sensor. The circuit was connected in a similar manner as the final circuit would have been connected. When the single sensor was passed over a subsurface crack 0.2 mm wide and 4 mm long, at a depth of more than 2 mm, the software registered the crack, proving that the Hall array and detector circuit worked as designed. Some modification were made to the detector circuit. The second amplifier stage was used to increase the gain and the bandwidth of the circuit and a DC amplifier stage was added to the output of the detector circuit. Since each detector circuit handled only one Hall sensor, these modifications were required for all 32 detector circuits. Due to project delays, time constraints

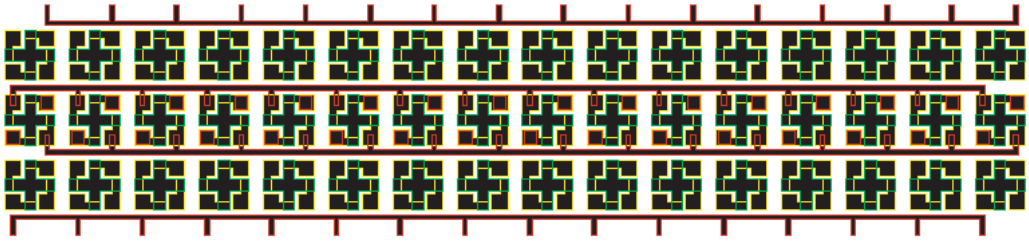

Figure 2.21 Parallel configuration of the Hall sensors

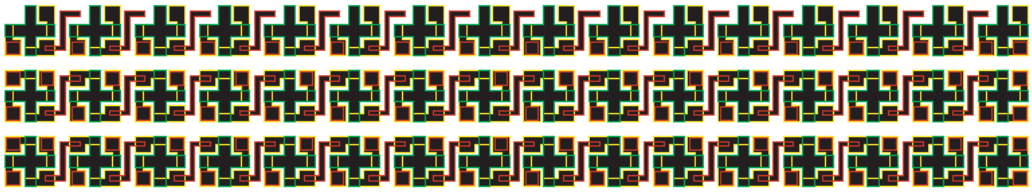

Figure 2.22 Series configuration of the Hall sensors

and an important member leaving the project, the above mentioned modifications could not be made by December 2005. Thus, the circuit was not tested using all 32 element Hall arrays connected simultaneously.

2.1.11 Acknowledgements

The work done on Hall array project was generously funded by the Federal Aviation Administration (FAA) and carried out at the Center of Nondestructive Evaluation at Iowa State University.

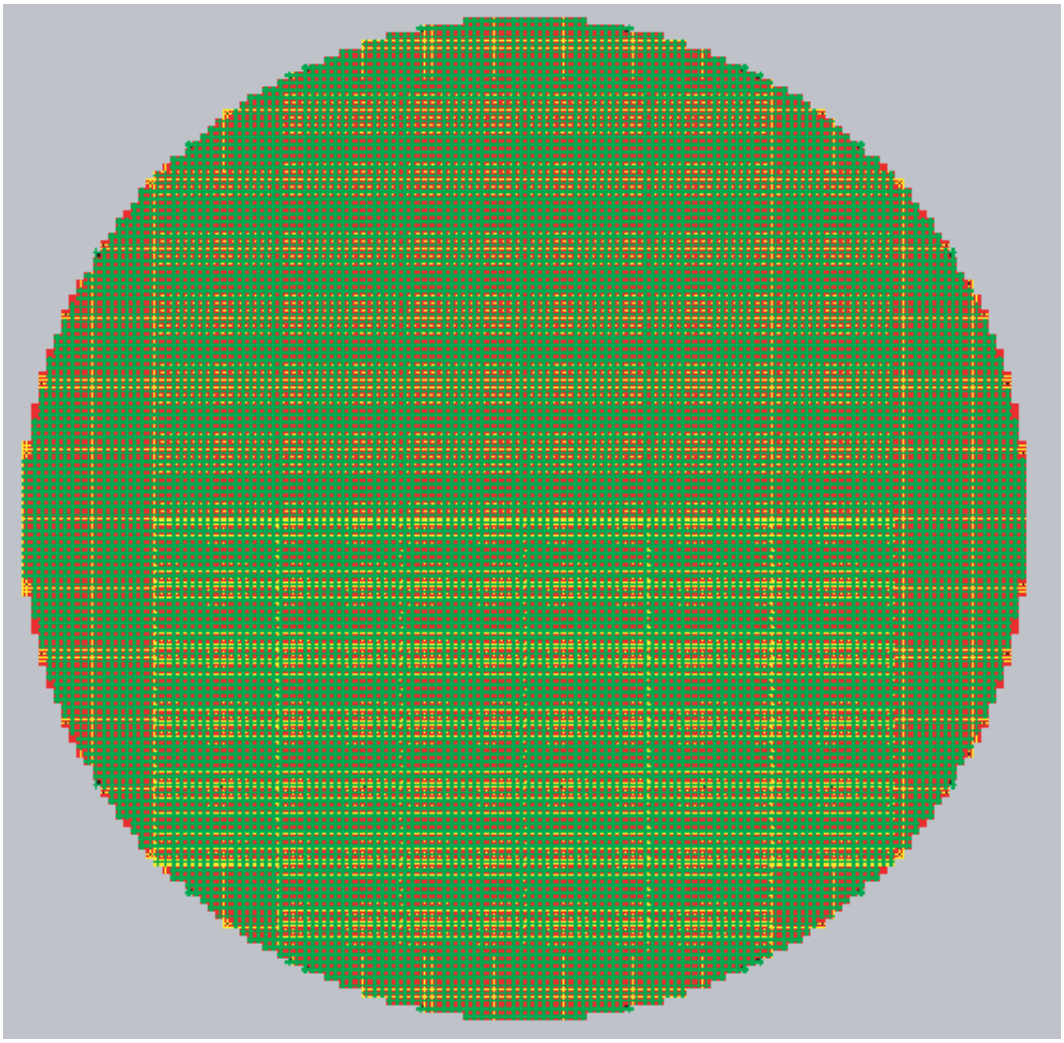

Figure 2.23 Actual wafer (die) of Hall sensors containing more than 5000+ Hall sensors

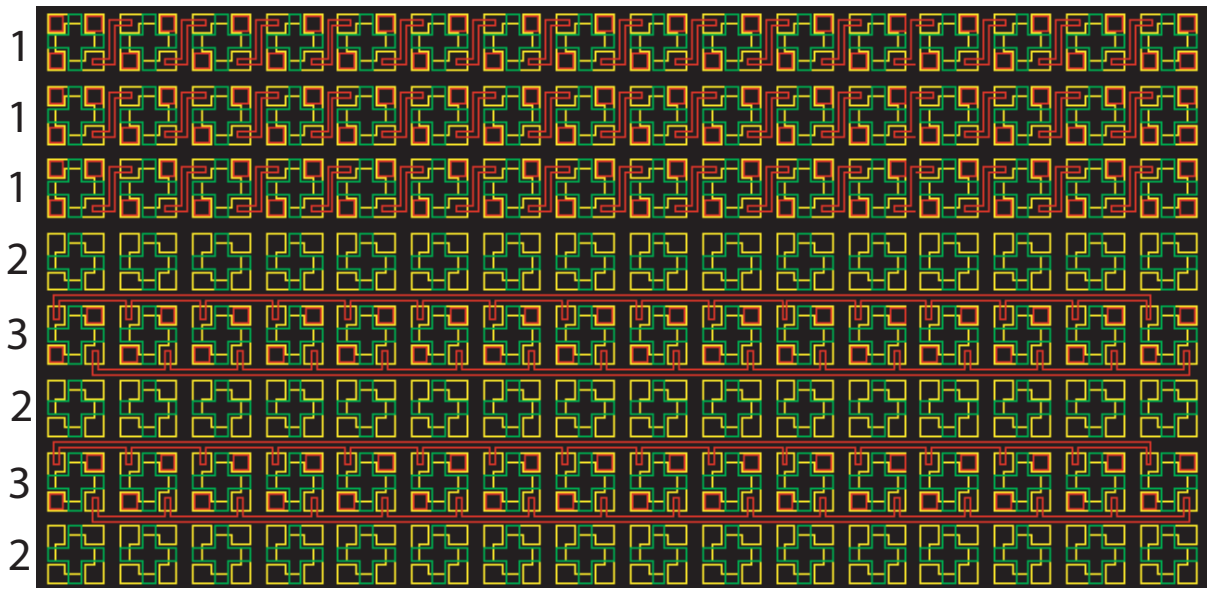

Figure 2.24 Zoomed in of the actual wafer showing 16 series (rows labeled 1), 16 parallel (rows labeled 3) and 16 individual (rows labeled 2) Hall sensors

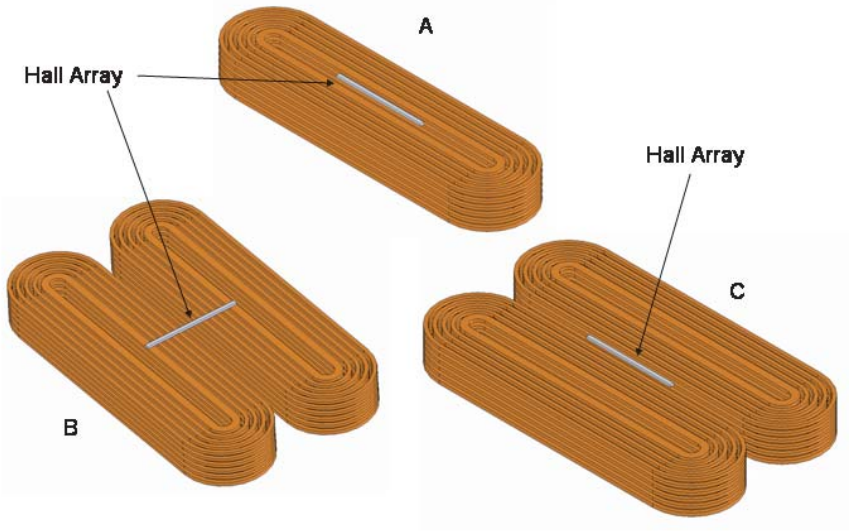

Figure 2.25 Coil configurations

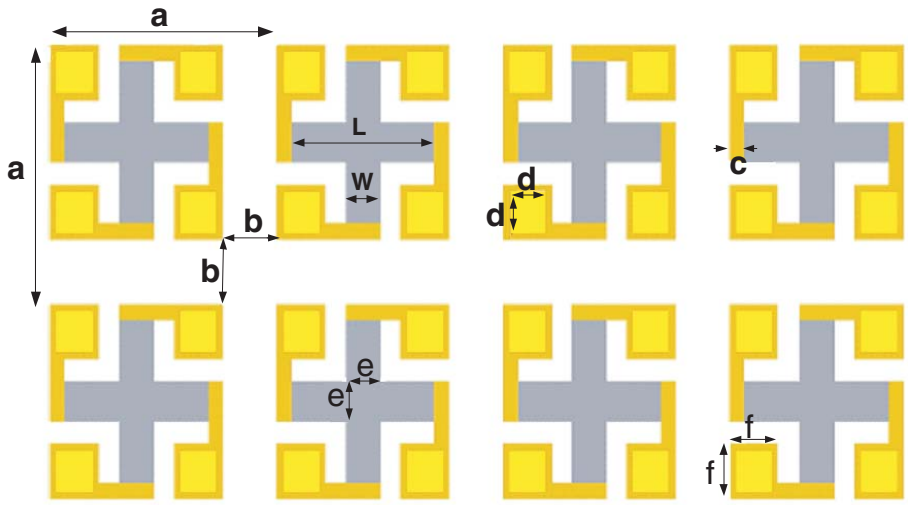

Figure 2.26 Hall sensors zoomed-in

APPENDIX. ENHANCED FLAW DETECTION USING AN EDDY CURRENT PROBE WITH A LINEAR ARRAY OF HALL SENSORS [27]

Haiyan Sun, Raza Ali, Marcus Johnson and John R. Bowler

Iowa State University, Center for Nondestructive Evaluation,

1915 Scholl Road, Ames, IA 50011

ABSTRACT

This article describes a new probe technology with enhanced flaw detection capability, which through the use of multiple magnetic field sensing elements, can also reduce inspection time. The probe contains a linear array of high-sensitivity Hall sensors and a racetrack coil. Instead of using individual Hall sensors to form the array, sensor arrays were fabricated directly on a wafer using photolithography techniques and then mounted in their unencapsulated form. The array dimensions are chosen to achieve high spatial resolution and to limit the overall probe size. Individual active elements have a minimum separation of 400 μm and a sensitive region 50 μm across. Electronic hardware and custom software have been developed to interface the new probes to a computer. Modulation of Hall current was introduced to discriminate the Hall signal from the effects of inductive pick-up and to improve signal to noise ratio.

INTRODUCTION

Conventional eddy current inspection uses induction coils to detect cracks and other flaws but it has been suggested recently that inductive probes are reaching their development limits and that new sensors are needed to push back the present boundaries of flaw detection [1]. For subsurface flaws such as cracks under fasteners in aircraft skins, the performance of inductive

sensors is limited by the need to use low frequencies to achieve significant penetration. Induction coil signals, being dependent on the rate of change of flux linkage, are less effective at low frequencies whereas typical solid state sensors do not suffer a diminished sensitivity in the low frequency regime. In a driver pick-up probe configuration, a relatively large coil can be used as a driver and high spatial resolution plus good low frequency performance achieved by using small solid state devices as sensors. Because the solid state sensors are easily fabricated as arrays, we can take advantage of this to produce probes that facilitate faster inspections.

Although coil arrays have been successfully produced and tested, additional turns of wire are needed for subsurface flaw detection to improve the low frequency performance. However, this increases their size and reduces the spatial resolution of the probe [2]. Arrays made with individual Hall sensor integrated circuits (ICs) and a rectangular coil have been produced [3] but the integrated circuit package is much bigger than the actual Hall element therefore the spacial separation of the devices is limited by the packaging. The probes described in this article overcome these difficulties. We also describe electronic hardware and custom software developed to interface the probes to a computer.

DESIGN OF THE HALL SENSOR ARRAYS

The Hall sensors, type P2, grown by a molecular beam epitaxy (MBE) system on a 2 inch wafer, were obtained from the University of Manchester Institute of Science and Technology in the United Kingdom. They are new two-dimensional electron gas Hall devices which were designed using the AlGaAs-InGaAs structure shown in Fig A.1. The sensors are designed for low magnetic field measurement of the order 1 μT with a magnetic field amplitude resolution of a few hundred nanoTesla [4]. The characteristics of the P2 Hall sensor are given in Table A.1 [4].

Two types of arrays were fabricated on a single wafer: one with the devices connected in series and the other with them connected in parallel. While the series arrays are suitable for constant current drive, its input resistance is very high. The arrays in parallel are suitable for constant voltage drive and have low input resistance which requires a low supply voltage.

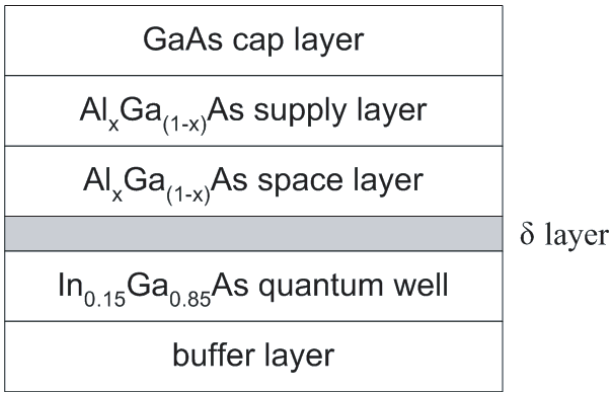

Figure A.1 Epitaxial structure of the Hall effect sensor (P2)

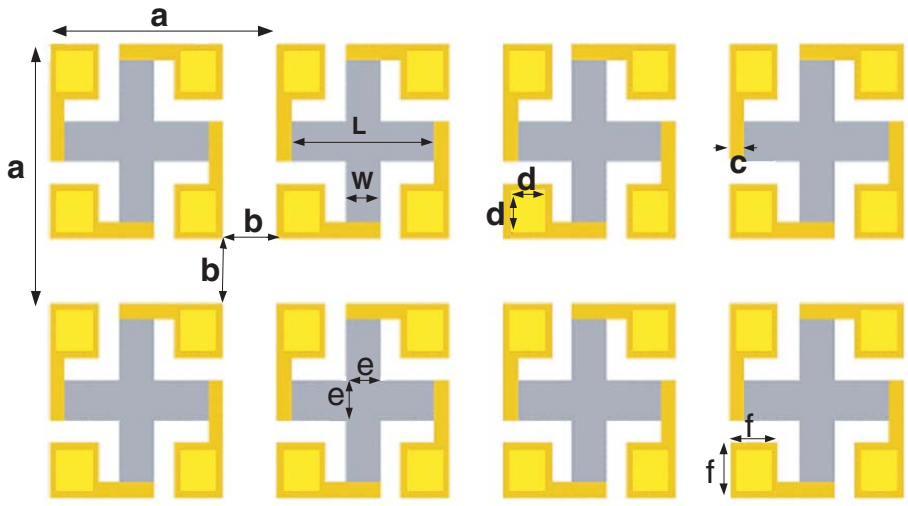

Figure A.2 Geometries of the Hall sensor arrays. The dimensions shown in the Fig are a = 400 μm, b = 90 μm, c = 70 μm, d = 80 μm, e = 50 μm, f = 100 μm, W = 70 μm, L = 210 μm. Note that the tracks connecting between sensors are not shown.

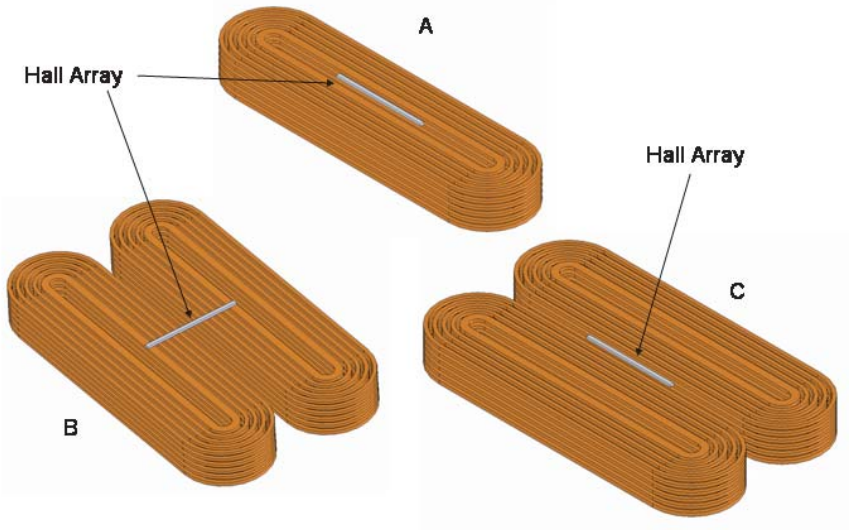

Figure A.3 Different coils and Hall sensor array arrangements.

Both types of array are under development and will be investigated to determine the best configuration. The two array types are fabricated in the central region of a single wafer while some individual devices populate the region near the boarder. This arrangement was used because the center of the wafer has more uniform properties than in the border region due to the fabrication process.

The Hall devices are in the form of square Greek cross with four ohmic contacts for each sensor, Fig A.2. The device structure is fully symmetrical and thus input and output resistance are the same. Each array has 16 elements with conductive tracks connecting them. The connecting tracks are made by thermal evaporation of titanium followed by gold. The arrays and individual devices have a pitch of 400 microns.

A printed circuit board (PCB) was designed with a long slot in the center for holding the Hall sensor arrays. Two Hall arrays, each having 16 Hall sensors, are glued in the slot. Each Hall sensor has two current supply contacts and two Hall signal contacts. The current

supply contacts were connected by tracks on the wafer for either series or parallel operation as mentioned above. The Hall signal contacts are wire-bonded to pads on the PCB. These pads are then connected to two insulation displacement cable (IDC) headers on the edges of the PCB by copper tracks. Pairs of copper tracks associated with an individual Hall sensor are routed directly opposite one another on two different layers. The purpose of this layout is to minimize the induction in the circuit loop.

There are three options to arrange the coils and the sensor array, Fig A.3. Option A uses one racetrack coil with the Hall array placed along the central line of the coil, where the magnetic field intensity is perpendicular to the Hall sensor surface. This generates a strong background signal due to the coil itself. Furthermore, the field at two ends of the array is different from at its center. Thus, although option A is simple, it suffers from a strong background signal and end effects. Options B and C use two racetrack coils with the Hall array placed between them. The current flowing in the two coils are of the same magnitude but in the opposite directions (one in the clockwise direction and the other in the counter-clockwise direction). In option C, the Hall array is placed exactly between the two coils and along the coil tracks, where the magnetic fields generated by two coils are canceled completely. Therefore, there is no background signal. In option B, the Hall array is placed between the coils and across the coil tracks, where the fields are partly canceled by each other and the the background signal is weak compared with option A. But the field is non-uniform along the Hall array. For option

Table A.1 Characteristics of the P2 Hall sensors.

Parameters	Value	Units
Nominal control current	1.5	mA
Input resistance	680	Ω
Output resistance	680	Ω
Mobility	6500	cm^2/V sec
Current sensitivity	180	V/AT
Current sensitivity drift over temperature	-0.08	% ^oC
Power consumption for $V_{in} = 1V$	1.4	mW

A and B, it is necessary to null the background signal before measurements.

SYSTEM DESIGN AND ELECTRONIC HARDWARE

The block diagram of the Hall array system is shown in Fig A.4. The racetrack coil is excited by a current source through a sensing resistor. The signal from each Hall sensor is connected to detector circuits, which will be discuss in detail below. Each channel contains one detector circuit. The voltage across the sensing resistor is amplified to serve as a reference signal to the detector circuits. This amplified voltage can be connected to the detector circuit directly as an in-phase reference or through a phase-shifter to give a quadrature reference. A switch is used to toggle between the two reference signals.

The output of the Hall probe is scanned through two data acquisition cards each having 16 channels. The output signals are displayed on a computer by a software written in National Instrument's Labview. The software scans the 32 channels, takes one sample per channel and then displays the result in an X-Y graph and a three dimensional (3D) intensity chart. The X-Y graph plots the amplitude versus channel number. The 3D intensity chart displays the amplitude per channel versus time. The amplitude is shown along the z-axis and its variations are shown by the change in color on the chart. Thus, when the probe is passed over a sample with defects in it the intensity chart will change color to indicate the presence of the defect.

As shown in Fig A.5, the detector circuit (one for each Hall device) consists of four parts: an amplifier, an analog multiplier AD633 (acting as a demodulator), a low pass filter and a sample-and-hold circuit. The Hall signal from each sensor is AC coupled to a two-stage differential amplifier. AC coupling can eliminate the DC offset of hall sensors. Due to differences in the Hall sensors, a gain resistor associated with the amplifier needs to be adjusted so that all channels will give the same signal level in a uniform field.

The AD633 is basically a multiplier that takes inputs X and Y and subtracts a third input, Z. The output, W, is thus:

$$W = XY + Z \tag{A.1}$$

Here X is amplified Hall signal. Y is the reference signal, coming from the sensing resistor

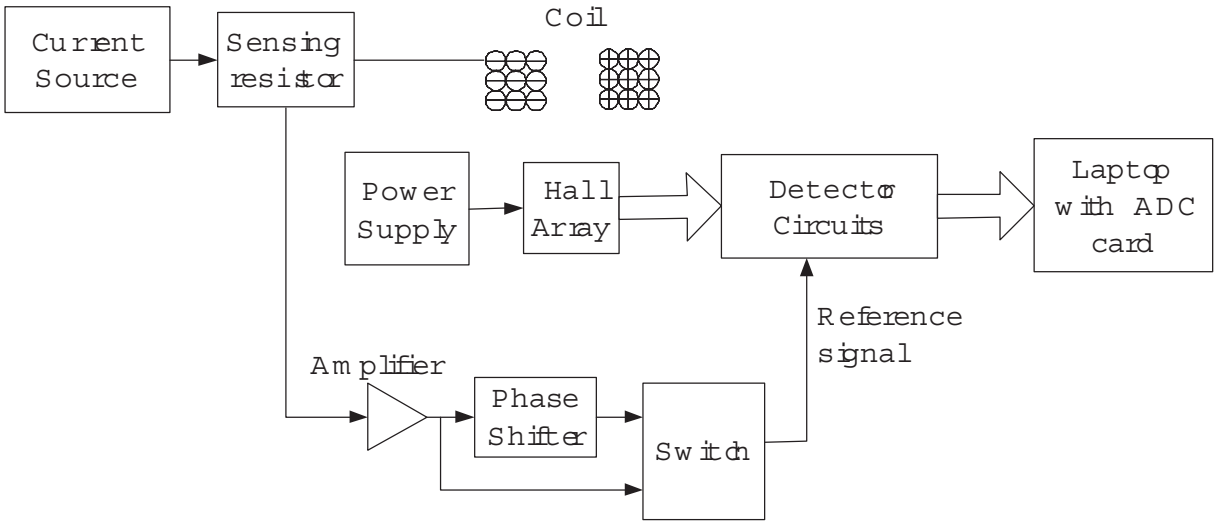

Figure A.4 Block diagram of the Hall array circuit system.

as shown in Fig A.4. Z is the DC output from sample-and-hold circuit and will be discussed below.

In normal operation, it is standard practice to null a conventional eddy-current probe, usually in the presence of an unflawed region of the specimen being inspected. The same is true of array probes, the only difference being that multiple channels must be nulled simultaneously. The demodulator AD 633 provides outputs (W) that are then filtered to give a DC level that is proportional to the magnetic field. This circuit also has provision for a separate DC input that is subtracted from the final output voltage. This input can be used to perform the null operation by the inclusion of a suitably configured sample-and-hold circuit. The sample-and-hold circuit consists of an integrator and FET (field-effect transistor) switch that is activated by a push-button control. Upon activation, the integrator output signal, which is subtracted from the demodulator's output, ramps until the filter-circuit output is equal to zero volts; at this point the sensor is said to be nulled. Gain can then be increased and small changes in the field seen by the Hall devices, such as those produced by a flaw, magnified.

The Hall effect voltage (V_H) is given by

$$V_H = K_H I B \tag{A.2}$$

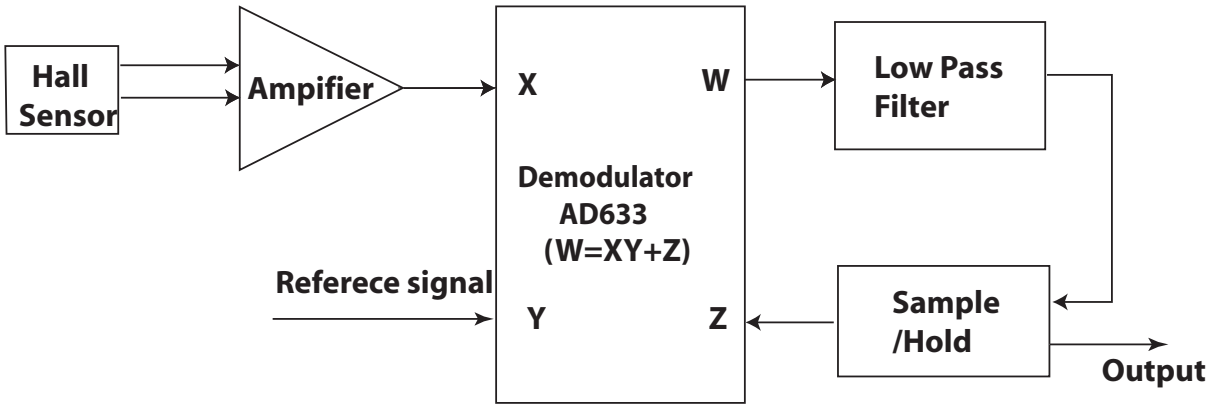

Figure A.5 Block diagram of the detector circuit for one channel.

where K_H is the open circuit (unloaded) current sensitivity, I is the supply current to the Hall sensor and B is the magnetic flux density to be measured. The measured voltage contains not only V_H, but also an induced voltage V_{ind} due to the loop area of the connecting leads. To separate the induced voltage from the genuine Hall effect voltage, the principle of modulation is employed. To modulate the Hall signals, the Hall sensor are supplied by an AC current at a frequency of ω_1, which varies sinusoidally with time as $I_0 \cos(\omega_1 t)$. This provides an another advantage over DC supply of avoiding the low frequency (1/f) noise, mainly generated by the Hall sensor. The coil current excites eddy currents at another frequency ω_2, which generates the magnetic field as

$$B = B_0 \cos(\omega_2 t) \tag{A.3}$$

The Hall voltage can then be written as

$$V_H = K_H I_0 \cos(\omega_1 t) B_0 \cos(\omega_2 t) = \frac{1}{2} V_{H0} [\cos(\omega_1 + \omega_2)t + \cos(\omega_1 - \omega_2)t] \tag{A.4}$$

where $V_{H0} = K_H I_0 B_0$. From Faraday's law, the induction voltage (V_{ind}) in the connecting loop can be expressed as

$$V_{\text{ind}} = -\frac{d\Phi}{dt} \qquad \text{with} \qquad \Phi = \Phi_0 \cos(\omega_2 t) \tag{A.5}$$

where Φ is the magnetic flux linking the connecting leads. The induced emf will appear in the measured voltage as a term which increases linearly with frequency. Thus the total measured

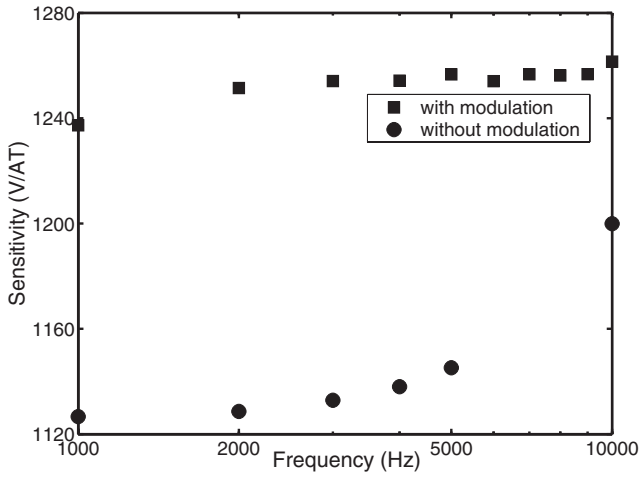

Figure A.6 Experimental results showing the effect of modulation. For the modulated data, the Hall sensor is biased with an AC current at a frequency of 30kHz which acts as the carrier frequency of the amplitude modulated signal. In acquiring data without modulation, the Hall sensor is biased with a DC current.

voltage is

$$V_T = \frac{1}{2}V_{H0}[\cos(\omega_1+\omega_2)t + \cos(\omega_1-\omega_2)t] + \Phi_0\omega_2\sin(\omega_2 t) \tag{A.6}$$

This expression shows that the measured voltage has three frequency components. To make sure modulation works properly, the Hall sensor is driven by a much higher frequency ω_1 than the coil frequency ω_2, then the ω_2 component will be much lower than $(\omega_1+\omega_2)$ and $(\omega_1-\omega_2)$ components. Thus the inductive voltage at ω_2 can be eliminated by a proper low pass filter. Instead of using a low pass filter, the process of modulation can also be accomplished by using a lock-in amplifier whose sensitivity and immunity to noise is well documented. The lock-in amplifier can measure the signal at $(\omega_1-\omega_2)$ and discard the other frequency components.

Experiments have been carried out to verify the benefit of modulating the Hall signals. An arbitrary waveform generator is used to generate drive current to the Hall sensor, drive current to the coil and the reference signal to a lock-in amplifier. These three signals have the same phase to make sure the lock-in amplifier can measure the desired Hall voltage properly. The sensitivity of the Hall sensor is plotted against the coil frequency which varies from 1kHz to

10kHz, Fig A.6. Here the sensitivity is defined as the Hall voltage divided by the magnitude of the magnetic flux density and the supply current to the Hall sensor. In the lower curve, the Hall sensor is supplied by a DC current, thus there is no modulation. In producing data using amplitude modulation, the Hall sensor is biased by an AC current at a frequency of 30kHz while the coil excitation current varies from 1 to 10 kHz. As shown in the Figure, without modulation, the apparent sensitivity increases with frequency especially at the higher frequency range. This is because the induction voltage which increases linearly with frequency can't be decoupled from the Hall voltage. With the modulation technique, the sensitivity is almost flat as the effect of the induced voltage has been removed. The difference in magnitude of the two curves is due to the gain introduced by a transducer during the modulation process.

SUMMARY

A multi-sensor linear array probe is being developed using high sensitivity, high resolution, custom designed Hall sensor arrays. It has a potential to reduce inspection time and to improve flaw detection ability. Test system has been built to process signals form multiple channels and display the signals on a computer. Modulation concept is introduced to reduce the induction voltage and to increase the signal to noise ratio.

ACKNOWLEDGEMENTS

This material is based upon work supported by the Federal Aviation Administration under Contact #DTFA03-98-D-00008, Delivery Order #IA043 and performed at Iowa State University's Center for NDE as part of the Center for Aviation Systems Reliability program.

REFERENCES

1. Airworthiness Assurance Working Group "Recommendations for Regulatory Action to Prevent Widespread Fatigue Damage in the Commercial Airplane Fleet," J. McGuire and J. Foucault, Chairpersons, Final report, (2002).

2. D.C. Hurley, K.H. Hedengren, P.J. Howard, W.P. Kornrumpf, G.E. Sutton, and J.D. Young, in *Review of Progress in QNDE*, Vol. 13 (1994), P.1111-1118.

3. R. A. Smith and D. J. Harrison, *Insight*, Vol. 46 No. 3 (2004).

4. N. Haned and M. Missous, *Sensors and Actuators A 3594* **39**, 1-7 (2002).

BIBLIOGRAPHY

[1] Harrison D. J, Jones L. D, and Burke S. K. Benchmark Problems for Defect Size and Shape Determination in Eddy Current Nondestructive Evaluation. *Journal of Nondestructive Evaluation*, 15(1): 21–34. (1996).

[2] Dodd C. V and Deeds W. E. Analytical Solutions to Eddy-Current Probe-Coil Problems. *Journal of Applied Physics*, 39(6): 2829–2838. (1968).

[3] Bowler J. R, Harfield N. Thin Eddy-Current Interaction with Semielliptical and Epicyclic cracks. *IEEE Transctions on Magnetics*, 36(1): 281–291. (2000).

[4] Bowler J. R, Jenkins S. A, Sabbagh L. D, Sabbah H. A. Eddy-current Probe impedance due to a volumetric flaw. *J. Appl. Phys*, 70(3): 1107–1114. (1991).

[5] Burke S. K. A benchmark problem for calculation of ΔZ in eddy-current nondestructive evaluation (NDE). *J. Nondestruct. Eval.*, 7: 35–42. (1988).

[6] McKirdy D. McA. Recent improvements to the application of the volume integral method of eddy-current modelling. *J. Nondestruct. Eval.*, 8: 45–52. (1989).

[7] Norton S. J, Bowler J. R. Theory of eddy-current inversion. *J. Appl. Phys*, 73: 501. (1993).

[8] Bowler J. R. Eddy-current interaction with an ideal crack: I. The forward Problem. *J. Appl. Phys*, 75: 8128–8137. (1994).

[9] Bowler J. R, Norton S. J, Harrison D. J. Eddy current intraction with an ideal crack: II The inverse problem. *J. Appl. Phys*, 75: 8138–8144. (1994).

[10] Burke S. K. Eddy-current inversion in the thin-skin limit: Determination of depth and opening for a long crack. *J. Appl. Phys*, 76: 3072–3080. (1994).

[11] Ward W. W and Moulder J. C. Low frequency pulsed eddy currents for deep penetration, *Review of Progress in Quantitative Nondestructive Evaluation*, 17(A): 291–298. (1998).

[12] Smith R. A and Hugo G. R. Transient eddy-current NDE for aging aircraft capabilities and limitations, *Fourth Joint DoD/FAA/NASA Conference on Aging Aircraft*, (May 2000).

[13] Conductivity and resistivity values for Aluminum and Alloys, http://www.ndt-ed.org/GeneralResources/MaterialProperties/ET/Conductivity_Al.pdf (Last access date: Jan. 20, 2007).

[14] Plummer J. D, Deal M. D and Griffin P. B. *Silicon VLSI Technology*, Prentice Hall Inc., 510–512, (2000).

[15] Ramsden ED. *Hall Effect Sensors - Theroy Application*, Cleveland, Ohio: Advanstar. (2001).

[16] Understanding Hall Effect Devices, http://www.sypris.com/library/documents/hall.pdf (Last access date: Jan. 20, 2007).

[17] Bulk Indium Arsenide BH-200 Series Datasheet, http://media.fwbell.com/BH200.pdf (Last access date: Jan. 20, 2007).

[18] Hall Effect Sensors, http://en.wikipedia.org/wiki/Hall_effect_sensor (Last access date: Jan. 20, 2007).

[19] Putley E. H. *Hall effect and related phenomena (Semi-conductor monographs)*, Butterworths, (1960).

[20] McGuire J and Foucault J. Recommendations for regulatory action to prevent widespread fatigue damage in the commercial airplane fleet. *Airworthiness Assurance Working Group, final report*, (2002).

[21] Smith R. A, and Harrison D. J. Hall sensor arrays for rapid large-area transient eddy current inspection, *Insight*, 46(3): 142–146, (2004).

[22] InSb Hall element moel HW105A: data sheet, Asahi Kasei Electronics, http://www.asahi-kasei.co.jp/ake/jp/product/hall/file/hw-105a.pdf, (Last access date: Jan 20, 2007).

[23] Haned N. and Missous M. Nano-tesla magnetic field magnetometry using an InGaAs-AlGaAs-GaAs 2DEG Hall sensor, *Sensors and Actuators A: Physical*, 102(3): 216–222, (2003).

[24] Data sheet for P2 and P15 Hall sensors, obtained by private communication with Sly J. L, School of Electrical and Electronic Engineering, University of Manchester, Manchester, UK.

[25] Decker M. R. GaAs and InAs Hall effect devices for nondestructive evaluation, Master of Science Dissertation, Iowa State University, Ames, Iowa, (2003).

[26] Haiyan Sun. Electromagnetic methods for measuring material properties of cylindrical rods and array probes for rapid flaw inspection, Doctor of Philosphy Dissertation, Iowa State University, Ames, Iowa, (2005).

[27] Sun H, Ali R, Johnson M. J, and Bowler J. R. Enhanced flaw detection using an eddy current probe with a linear array of hall sensors, *Review of Progress in Quantitative Nondestructive Evaluation*, 24: 516–522. (2005).

ACKNOWLEDGEMENTS

I would like to thank my major professor Dr. John Bowler for his valuable help and support, without which this thesis would not have been possible. I would also like to thank Marcus Johnson, Haiyan Sun and Fangwei Fu for working with me and helping me with the project presented in this thesis. I am also indebted to my committee members Dr. John Bowler, Dr. Nicola Bowler and Dr. David Hsu.